Spin-valve effect in nanoscale Silicon spin-valve devices

Duong Dinh Hiep

PhD Dissertation

Dissertation supervisor

Associate Professor Pham Nam Hai

Department of Physical Electronics

Tokyo Institute of Technology

January, 2019

Doctoral Committee:

Associate Professor Pham Nam Hai, supervisor

Professor Shigeki Nakagawa

Professor Takaaki Manaka

Professor Akira Yamada

Associate Professor Shinsuke Miyajima

Dr. Hidekazu Saito

Contents

CHAPTER 1

INTRODUCTION

1.1. Spintronics

Every electron has an intrinsic form of angular momentum, called “Spin”. Understanding the electron spin property and its interaction with surrounding solid-state environments gives us an opportunity to control the state of not only the spin of individual electron but also a whole spin system. Spintronics, brief of spin-based electronics, is the study in which the spin degree freedom of electrons are employed to create new forms of information storage, as well as the foundation for new paradigm of information processing and low-power nonvolatile electronics.

The beginning of spintronics could be considered starting from the researches of Nevill Francis Mott, an English physicist who won the Nobel Prize for Physics in 1977. By investigating an unusual behavior of resistance in ferromagnetic metals, he outlined some primary paths for our understanding of spin-polarized transport. In his researches, when the temperature is low enough, he recognized that magnon scattering becomes very small, then the majority and minority spin which the magnetic moment are parallel and antiparallel to the magnetization of a ferromagnet do not mix in the scattering processes. As a result, the current in ferromagnets is polarized into majority and minority spin, thus the total

conductivity can be identified by the sum of two independent and unequal parts for two different spin projections [1,2].

Then, the first work to impressively bring the spin information from pure physics into real applications belongs to the groups of Albert Fert and Peter Grunberg, who demonstrated the giant magnetoresistance (GMR) in the end of the 1980s [3,4]. Until that time, people only employed the electrical characteristic of electron in electronic devices. Because of its impact in establishing the new field of spintronics, the discovery of the GMR brought to Albert Fert and Peter Grunberg the Physics Nobel award in 2007 [5]. The GMR devices detect information by utilizing the interaction of spin of electron with magnetic materials. The application of GMR could be listed here such as spin-valve sensors, hard disk drives or MRAM. In the GMR devices, there are two or more ferromagnetic (FM) layers with a few nanometers thick each layer separated by non-magnetic materials. In the operation process, the device shows a low resistance when the status of the FM layer magnetizations are parallel and high resistance in the antiparallel status. This simple concept works very successfully in the read heads of standard computer hard disk drives nowadays. Additionally, the parallel – antiparallel concept is employed to develop the so-call novel non-volatile magnetic random access memory (MRAM) as well. The spin transfer torque (STT) effect is also another promising direction in the memory technology. Based on the STT effect, people demonstrated the possibility of exciting the magnetization of ferromagnet and switching its direction by a spin current instead of using an external magnetic field [6,7,8,9], brightening the concept of STT-MRAM.

Chapter 1

Recently, semiconductor based lateral spin devices have received great attention for employing the spin nature of electrons in potential applications for the ultra-dense, high-speed, low-power operation memory devices and reconfigurable logic [10,11,12]. Spin MOSFET research is directed in this point of view in the emerging research devices in Beyond CMOS era [13]. The understandings of spin injection, detection and manipulation are vital for purpose of fully functional spin transistors realizing.

Semiconductor based lateral spin devices

In lateral spin devices, generally the electrodes are arranged horizontally, which is easy for that fabrication process. Based on the operating method as well as geometry structure, people divide the lateral spin based devices into two types: a two-terminal spin valve device and a three-terminal spin transistor. In two-terminal spin valve devices, there are two ferromagnetic electrodes. The resistance between the two ferromagnetic electrodes becomes high when the two FMs are aligned in the antiparallel configuration and low when the two FMs are in parallel configuration. The operation concept is similar to GMR or TMR devices. Even though experimental results show the switching behavior of spin-dependent resistance in all metal-based spin valve devices, it is challenging to observe such response in semiconductor-based devices because of the conductivity mismatch between the ferromagnetic electrodes and the semiconductor channel. This issue is the main obstacle on the way of bringing the semiconductor-based spin valve devices into practical applications.

1.1.1. Spin valve devices

The origin of spin valve devices came from the idea of the spin injection from ferromagnetic electrodes into a non-magnetic medium which is proposed firstly by Aronov, then experimentally demonstrated by Johnson and Silsbee [14] in a metallic channel. For semiconductor channel, the spin valves were experimentally demonstrated [15,16] in a GaAs channel device in 2005. The operation concept of a spin valve device is similar to a diode-like device, in which there are two resistance status: one is high when the two ferromagnetic electrodes are in antiparallel configuration, and another is low when they are in parallel configuration. Base on the geometry structure, the semiconductor spin valve devices are divided into two types: the 1st is the lateral structure, and the 2nd is the vertical structure, as shown in Fig. 1.1.

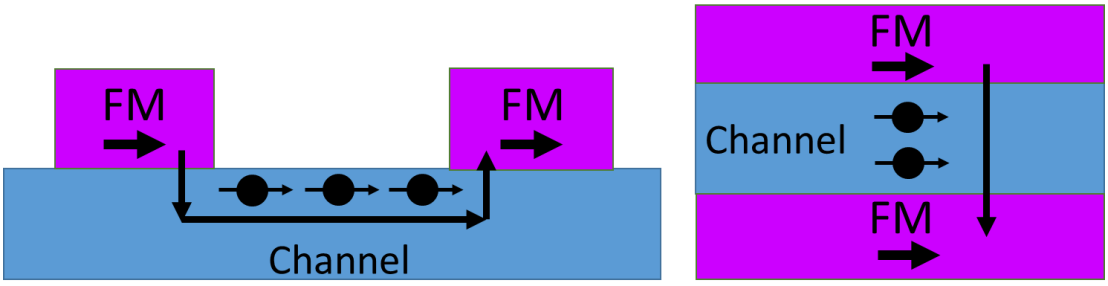

Figure 1.1: Schematic illustration of a (left) lateral spin valve and (right) vertical spin valve geometry.

In the lateral spin valve (LSV) devices, the spin injection and transport directions are orthogonal to each other. This type of device is based on planar technologies which is commonly used in conventional microelectronics technology. Hence, it has an advantage of being easily integrated into process flows without a harsh change. Furthermore, LSVs have

the possibility of demonstrating electric current switching, by using a third gate electrode to control the spin of the electrical current.

In the vertical spin valve (VSV) devices, the spin injection and transport directions are parallel to each other. The VSV device has similar operating mechanism to a LSV device, but shows higher magnetoresistance response. The reason is in this type of device, people can precisely control the channel length and conducting area by using epitaxial growth techniques. The short channel length could preserve the spin information of electrons, then allowing more spin-polarized electrons reach to detector before the spin-relaxation process finish. However, manipulating spin in the VSV device is more difficult than the LSV, because of the problem in fabricating an all-around gate electrode around the thin channel layer.

1.1.2. Spin FETs

Spin-based logic devices (spin transistors) are generally viewed as the promising candidate for ultra-dense, high-speed, low-power operation memory devices and reconfigurable logic [10,11,17]. The Spin-based logic devices have been classified as the "Non-Conventional Charge-based Extended CMOS Devices" by ITRS. It means that, these devices show transistor-like behaviors with the operating mechanism of a spintronic device. The spintronic logic devices are defined as possessing the abilities of control the current or voltage by the magnetization configuration of the ferromagnetic contacts with respect to the majority spin orientation, and non-volatile information storage using the magnetoresistance and spin torque effects. Those abilities are very advanced functionalities for energy efficient, high-performance circuit architectures but are being inaccessible to conventional CMOS

circuits. Several spin-based logic devices have been proposed. The first one is known as the Datta-Das transistor, in which the spin of electron is controlled by a gate voltage through the spin-orbit coupling [12]. However, there is no Datta-Das transistor demonstrated so far, and a convincing experimental realization of the device has shown the impractical possibility of this concept. Nevertheless, it still provides the basic idea and platform for future spin-based logic devices to improve upon by using the spin-orbit interaction to systematically control a spin system.

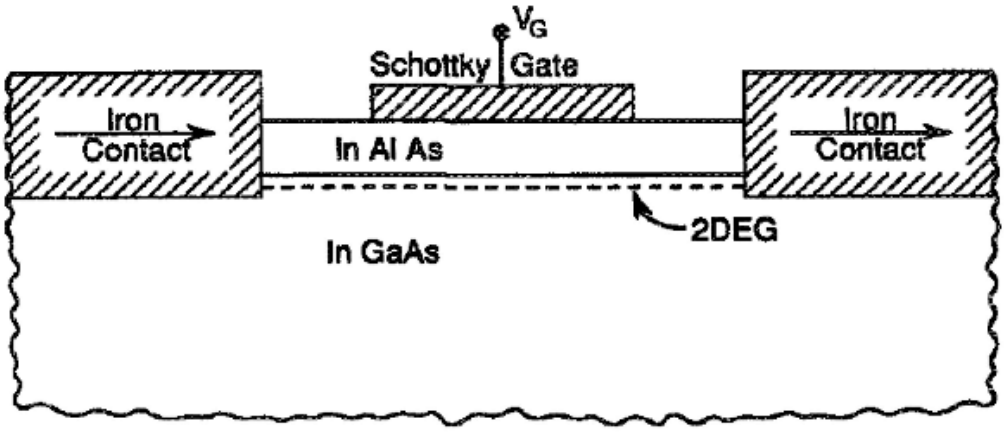

Figure 1.2: Structure of the spintronic analog of the electro-optic modulator proposed by Datta and Das in 1990 [12]. Reprinted from Appl. Phys. Lett. 56, 665 (1990), with the permission of AIP Publishing.

Besides the Datta-Das spin transistor concept, Fabian and Zutic also proposed another potential spin-logic device – the magnetic bipolar transistor (MBT) [18]. The operation concept of this device is similar to the conventional bipolar junction transistor (BJT) with offers the new function of controlling current amplification by spin property. In order to

maximize the gain in a conventional BJT, it is necessary to minimize the relative contribution of holes in the emitter current or prevent the e-h (electron-hole) recombination in the base region. This condition is realized by the ability of spin control in the MBTs [19].

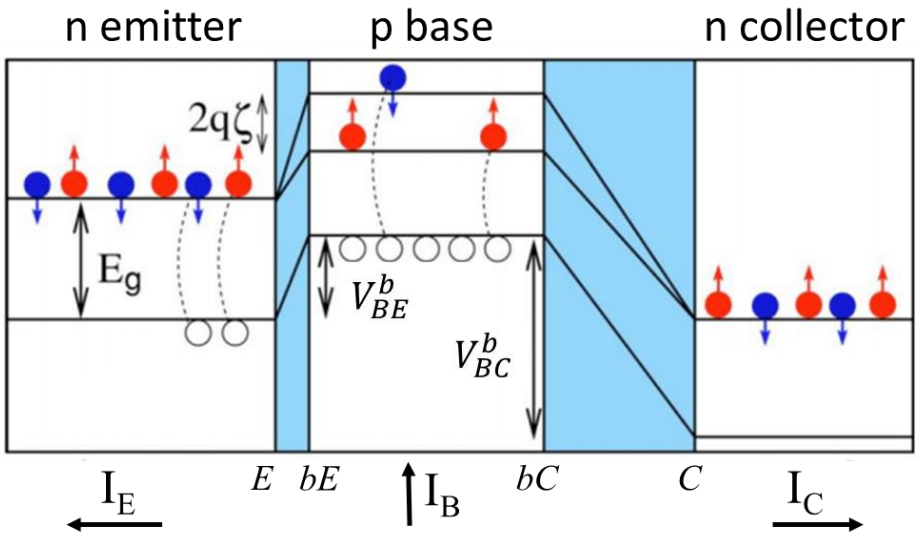

Figure 1.3: Illustration of the magnetic n-p-n transistor in the amplification mode in which the B-E junction is forward biased ($V_{BE} > 0$) to lower the barrier and reduce the depletion layer width, while the B-C junction is reverse biased ($V_{BC} < 0$) to raise the barrier and expand the depletion layer width. It is possible to control the current amplification $\beta = I_C/I_B$ by the spin polarization in the base as well as by the nonequilibrium spin in the emitter [18].

The most practical spin-logic device is the concept of spin metal-oxide-semiconductor field-effect transistor (spin-MOSFET), which has been proposed by Tanaka and Sugahara [13]. The silicon (Si) based spin MOSFET is considered to be one of the most promising candidates because of its high compatibility with CMOS technology and long spin lifetime

in Si [17,13,20,11,21]. However, there is no Si-based spin MOSFET demonstrated so far because the issue of conductivity mismatch has been not solved yet.

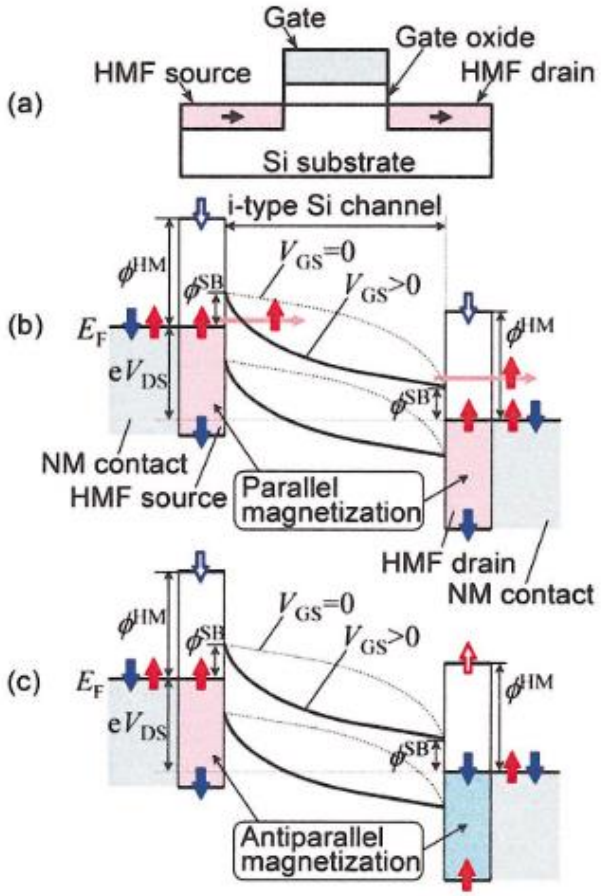

Figure 1.4: (a) Schematic device structure and band diagrams of the spin MOSFET in (b) parallel and (c) antiparallel magnetization configurations. Solid arrows in the HMF source/drain show up-spin and down-spin electrons at the Fermi energy of the metallic spin band and at the valence band edge of the insulating spin band. Open arrows represent the conduction band edge of the insulating spin band of the HMF source/drain [13]. Reprinted from Appl. Phys. Lett. 84, 2307 (2004), with the permission of AIP Publishing.

1.2. Silicon spintronics

Recently, there is a huge attention in combining the semiconductors and magnetic materials, aiming to create a revolutionary and energy-efficient information technology in which digital data are encoded in the spin of electrons. Magnetic materials show advantages in non-volatile memory such as rapidly switching, unlimited endurance, and high resistance to noise. On the other hand, semiconductor is in the heart of logic technology. Therefore, a combination of memory and logic computing is promising for next generation electronic devices. In that circumstance, implementing spin functionality in silicon, the mainstream semiconductor, is essential to establish spin-based electronics with potential to change information technology beyond imagination. Si-based spin-MOSFET is the most realistic concept to do so. In fact, Si shows key advantages such as it is the de-facto material of electronics; it has small spin-orbit interaction, thus long spin lifetime of electron in Si is expected; and the spin transport over μm in Si has been demonstrated. Therefore, it is the very promising channel material for Spin-MOSFET.

1.3. Motivation

Conventional CMOS (complementary metal oxide semiconductor) device is based on manipulation of the electron charge current. The main innovation trend of CMOS is primarily focused on miniaturization, roughly doubling the number of transistors in one unit every 18 months, known as Moore's law. Leading semiconductor corporations have been able to keep

Moore's law strong by improving lithographic techniques and fabricating smaller devices, as shown in Fig. 1.5. However, the enormous enhancement in lithography and innovations in device engineering cannot change the fact that, sooner or later, conventional CMOS devices will reach a physical limit where further miniaturization of the device will be fundamentally impossible. Moreover, conventional CMOS technology is facing serious problems of high idling power consumption and heat generation due to leakage off-current when the device size is miniaturized to nanoscale, which restricts the device operating speed. Hence, there is a demand for alternative low-power solutions to overcome these problems in the beyond-CMOS era. The silicon (Si) based spin-MOSFET is a promising solution because of its high compatibility with the well-established CMOS technology and long spin lifetime in Si [13,17,11,20,21]. For that reason, there has been a great interest in demonstrating spin injection and detection of spin transport in Si by ferromagnetic electrodes. In fact, spin injection into microns of Si channels by using the three terminal Hanle effect [22,23,24] or the four-terminal spin-valve effect [25,26,27] has been demonstrated. However, previous researches only studied the spin transport in micron-scale Si channels and the typical spin-dependent output voltages were less than 1 mV which is not enough for realistic spin-MOSFET.

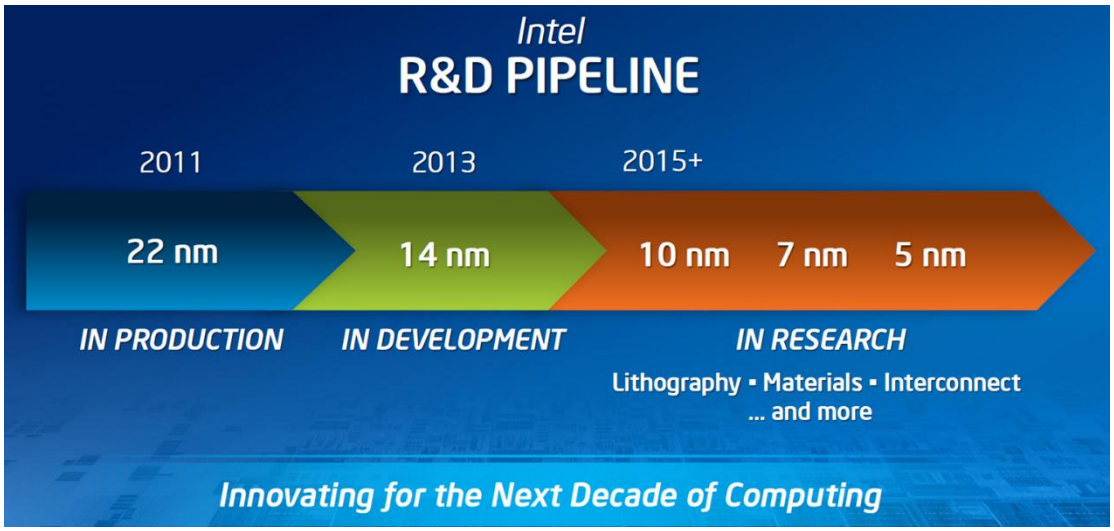

Figure 1.5: R&D pipeline of Intel for the scaling down process in IC technology [source: Intel].

To improve the spin-dependent output voltage, I propose the spin-valve effect utilizing ballistic electron transport in nanoscale Si channel. It is expected that the ballistic transport of electrons in such nanoscale channels may overcome the conductivity mismatch problem which arises at the interface between a ferromagnetic (FM) electrode and a diffusive semiconductor (SC) channel [28,29], resulting in a higher spin-dependent output voltage.

1.4. Thesis outline

The purpose of this thesis is systematically investigating the spin-dependent transport characteristics in nanoscale Si-based 2 terminal spin-valve devices with a Si channel length as short as 20 nm.

Chapter 1

The thesis is divided into 9 chapters.

Chapter 1 is an introduction to the topic of spintronics in general, and silicon spintronics in particular, and the motivation for this study.

Chapter 2 introduces the physics of spin injection and relaxation in diffusive regime and ballistic regime, then briefly discusses the electrical spin injection and transport measurements.

Chapter 3 describes in detail the fabrication and measurement process of nanoscale Si-based 2 terminal spin-valve devices in this study.

Chapter 4 focuses on the investigation of spin-valve devices fabricated by Electron Beam Evaporation.

Chapter 5 focuses on the investigation of spin-valve devices fabricated by Molecular Beam Epitaxy.

Chapter 6 describes the important role of ballistic transport in nanoscale spin-valve devices.

Chapter 7 presents the optimization of the MgO tunnel barrier thickness in spin-valve devices to achieve a higher spin-dependent output voltage.

Chapter 8 describes the effect of inserting a Mg buffer layer in between the Fe and MgO layer to improve the spin-injection in spin-valve devices.

Chapter 9 summarizes the main results of this thesis and discusses on future respects.

1.5. Summary

Spintronics is the technology which aims to utilize the spin degree freedom of electrons for many applications in nowadays and future technology such as new forms of information storage, as well as the foundation of new paradigm for information processing and low-power nonvolatile green electronics. In spintronics, the spin-MOSFET is considered to be the building block of low-power-consumption electronics devices. In the respect of a semiconductor material, Si shows key advantages such as it is the de-facto material of electronics; it has small spin-orbit interaction, thus long spin lifetime of electron in Si is expected; and the spin transport over μm in Si has been demonstrated. Therefore, Si is the very promising channel material for Spin-MOSFET. One obstacle staying on the developing road is the low performance of spin-valve device in the diffusive regime, which is replaced by ballistic regime in this study. This chapter gave a quick view of silicon spintronics researches, especially in spin injection and transport.

References

1. Mott N. F. and Wills H. H. The Electrical Conductivity of the Transition Metals. *Proc. R. Soc. A Math. Phys. Eng. Sci.* **153,** 699–717 (1936).

2. Mott N. F. The Resistance and Thermoelectric Properties of the Transition Metals. *Proc. R. Soc. A Math. Phys. Eng. Sci.* **156,** 368–382 (1936).

3. Baibich, M. N. *et al.* Giant Magnetoresistance of (001)Fe/(001)Cr Magnetic

Superlattices. *Phys. Rev. Lett.* **61,** 2472–2475 (1988).

4. Binasch, G., Grünberg, P., Saurenbach, F. & Zinn, W. Enhanced magnetoresistance in layered magnetic structures with antiferromagnetic interlayer exchange. *Phys. Rev. B* **39,** 4828–4830 (1989).

5. Wolf, S. A. Spintronics: A Spin-Based Electronics Vision for the Future. *Science* **294,** 1488–1495 (2001).

6. Slonczewski, J. C. Current-driven excitation of magnetic multilayers. *J. Magn. Magn. Mater.* **159,** L1–L7 (1996).

7. Berger, L. Emission of spin waves by a magnetic multilayer traversed by a current. *Phys. Rev. B* **54,** 9353–9358 (1996).

8. Tsoi, M. *et al.* Excitation of a Magnetic Multilayer by an Electric Current. *Phys. Rev. Lett.* **80,** 4281–4284 (1998).

9. Katine, J. A., Albert, F. J., Buhrman, R. A., Myers, E. B. & Ralph, D. C. Current-Driven Magnetization Reversal and Spin-Wave Excitations in Co / Cu / Co Pillars. *Phys. Rev. Lett.* **84,** 3149–3152 (2000).

10. Fabian, J., Matos-Abiague, A., Ertler, C., Stano, P. & Zutic, I. Semiconductor Spintronics. *Acta Phys. Slovaca* **57,** 565–907 (2007).

11. Žutić, I., Fabian, J. & Das Sarma, S. Spintronics: Fundamentals and applications. *Rev. Mod. Phys.* **76,** 323–410 (2004).

12. Datta, S. & Das, B. Electronic analog of the electro-optic modulator. *Appl. Phys. Lett.* **56,** 665–667 (1990).

13. Sugahara, S. & Tanaka, M. A spin metal–oxide–semiconductor field-effect transistor using half-metallic-ferromagnet contacts for the source and drain. *Appl. Phys. Lett.* **84,** 2307–2309 (2004).

14. Johnson, M. & Silsbee, R. H. Interfacial charge-spin coupling: Injection and detection of spin magnetization in metals. *Phys. Rev. Lett.* **55,** 1790–1793 (1985).

15. Saha, D., Basu, D., Holub, M. & Bhattacharya, P. Two-dimensional spin diffusion in multiterminal lateral spin valves. *Appl. Phys. Lett.* **92,** 022507 (2008).

16. Lou, X. *et al.* Electrical detection of spin transport in lateral ferromagnet–semiconductor devices. *Nat. Phys.* **3,** 197–202 (2007).

17. ITRS. International Technology Roadmap for Semiconductors 2.0: Executive Report. *Int. Technol. roadmap Semicond.* 79 (2015).

18. Fabian, J. & Žutić, I. Spin-polarized current amplification and spin injection in magnetic bipolar transistors. *Phys. Rev. B* **69,** 115314 (2004).

19. Flatté, M. E., Yu, Z. G., Johnston-Halperin, E. & Awschalom, D. D. Theory of semiconductor magnetic bipolar transistors. *Appl. Phys. Lett.* **82,** 4740–4742 (2003).

20. Tanaka, M. & Sugahara, S. MOS-Based Spin Devices for Reconfigurable Logic. *IEEE Trans. Electron Devices* **54,** 961–976 (2007).

21. Zarifis, V. & Castner, T. G. ESR linewidth behavior for barely metallic n-type silicon. *Phys. Rev. B* **36,** 6198–6201 (1987).

22. Dash, S. P., Sharma, S., Patel, R. S., de Jong, M. P. & Jansen, R. Electrical creation of spin polarization in silicon at room temperature. *Nature* **462,** 491–494 (2009).

23. Dash, S. P. *et al.* Spin precession and inverted Hanle effect in a semiconductor near a finite-roughness ferromagnetic interface. *Phys. Rev. B* **84,** 054410 (2011).

24. Li, C. H., van 't Erve, O. M. J. & Jonker, B. T. Electrical injection and detection of spin accumulation in silicon at 500 K with magnetic metal/silicon dioxide contacts. *Nat. Commun.* **2,** 245 (2011).

25. Huang, B., Monsma, D. J. & Appelbaum, I. Coherent Spin Transport through a 350 Micron Thick Silicon Wafer. *Phys. Rev. Lett.* **99,** 177209 (2007).

26. Sasaki, T. *et al.* Electrical spin injection into silicon using MgO tunnel barrier. *Appl. Phys. Express* **2,** (2009).

27. Aoki, Y. *et al.* Investigation of the inverted Hanle effect in highly doped Si. *Phys. Rev. B* **86,** 081201 (2012).

28. Schmidt, G., Ferrand, D., Molenkamp, L. W., Filip, A. T. & van Wees, B. J. Fundamental obstacle for electrical spin injection from a ferromagnetic metal into a diffusive semiconductor. *Phys. Rev. B* **62,** R4790–R4793 (2000).

29. Fert, A. & Jaffrès, H. Conditions for efficient spin injection from a ferromagnetic metal into a semiconductor. *Phys. Rev. B* **64,** 184420 (2001).

CHAPTER 2

FUNDAMENTAL PHYSICS of SPIN TRANSPORT

In this chapter, overviews of the spin transport mechanisms in diffusive regime and ballistic regime were presented. Additionally, electrical spin measurements techniques were discussed. An understanding of the physical mechanisms that govern spin transport inside semiconductors is essential for proper design and characterization of these devices, as well as for overcoming the current issues.

2.1. Spin transport in the diffusive regime

2.1.1. Two-current model

A conventional approach to understand and explain spin transport effects is the two-current model which was firstly proposed by Valet and Fert in 1993 [1]. In this model, electrons have 2 types of spin: up-spin and down-spin. Up-spin electrons have their spins aligned with the magnetization of the ferromagnetic metal (FM), while down-spin electrons have their spins aligned in the opposite direction. Other spin directions are mapped on these two directions. That is the reason why it is called two-current model.

According to the Einstein relation, the conductivity of a material is described by the formula:

$$\sigma = De^2\nu(E_F) \tag{2.1}$$

In the above formula, D is the diffusion coefficient, e is the electron charge and ν is the density of states (DOS) of electron at the Fermi level E_F. In the FM, because the DOS of two spin directions at E_F are different, there is a difference in conductivity of up-spin and down-spin $\sigma_{\uparrow,\downarrow} = De^2\nu_{\uparrow,\downarrow}(E_F)$, then the total conductivity and total DOS can be calculated as $\sigma = \sigma_\uparrow + \sigma_\downarrow$ and $\nu = \nu_\uparrow + \nu_\downarrow$, respectively. The symbol ↑ and ↓ represent the spin directions, spin-up and spin-down.

By using this difference in conductivity of two spin directions, one can characterize the relative magnetization direction of two FM electrodes in a serial circuit. That is the idea of the local spin-valve effect. In the serial circuit with FM electrodes, the circuit response can

be illustrated as Fig. 2.1(a) and 2.1(b) by using the two-current model, disregarding the resistance of materials between the FM electrodes. If all FM electrodes have their magnetizations aligned in the same direction (parallel state), one type of spin exhibits a high conductance (low resistance) in all FM electrodes, while the other type of spin exhibits a low conductance (high resistance) as described in Fig. 2.1(a). On the other hand, in the antiparallel state in which each FM electrode aligned its magnetization in opposite directions, both spin types exhibit a low resistance in one FM electrode and a high resistance in the other FM electrode as shown in Fig. 2.1 (b). Therefore, the antiparallel state usually appears in a higher resistance than the parallel state. This model is used to explain the local spin-valve signal as indicated in Fig. 2.1 (c). The magnetizations of two FM electrodes connected to a silicon channel are switched from parallel to antiparallel orientation and back, using a magnetic field [2]. The FM electrodes can be switched independently as they have different coercive fields and the system shows a higher resistance when the electrodes are in antiparallel alignment.

In this local spin-valve concept, two FM electrodes work as an injector/detector and have to be separated by a non-magnetic material to enable the independent switching of their magnetizations. The spins are injected from the injector electrode into the non-magnetic channel, transport through this channel without losing their spin orientation, then detected at the detector electrode. If the spin orientation is maintained while the electrons travel between the FM electrodes, the relative orientation of the magnetizations of the FM electrodes is the primary factor influences the resistance of the device.

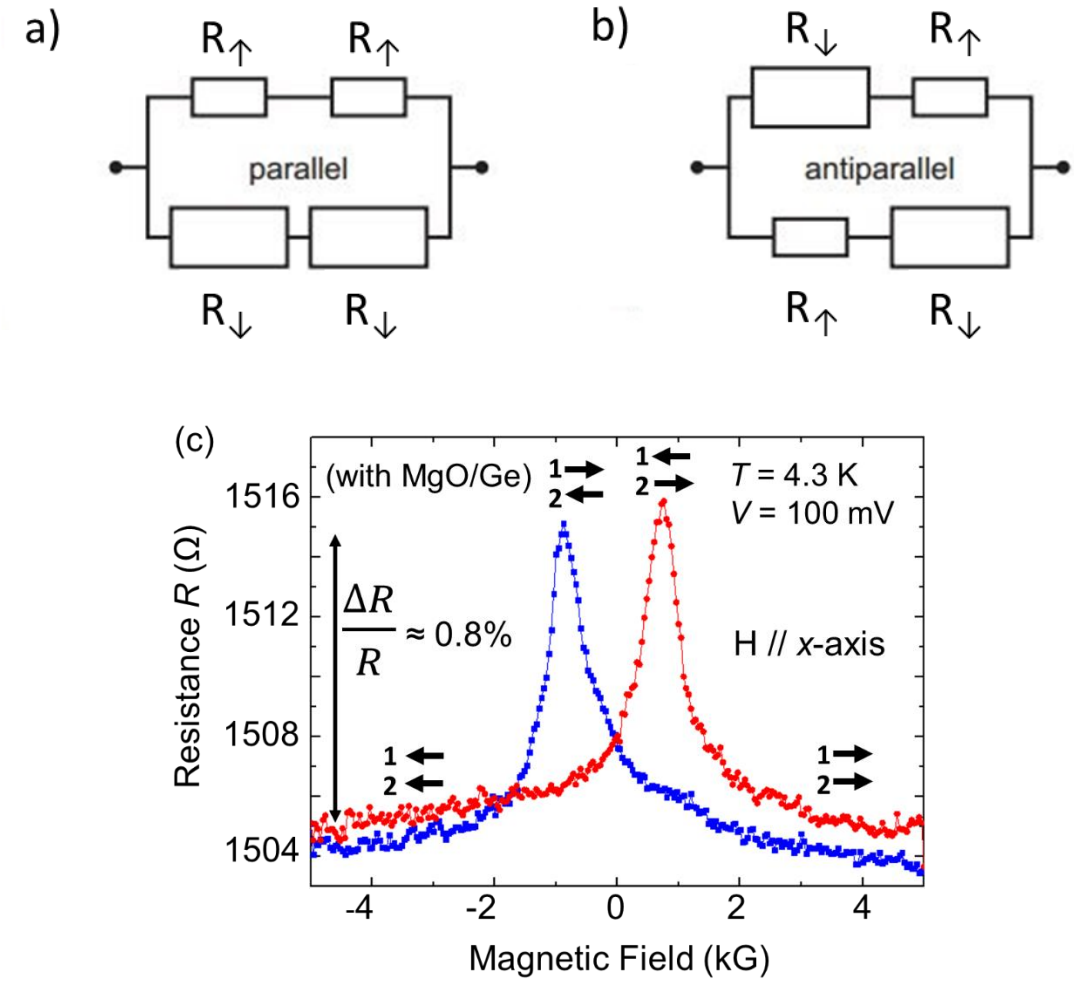

Figure 2.1: The two-current model for two FM electrodes in serial connection. Spin-down electrons exhibit a high resistance $R_\downarrow$ while spin-up electrons show a low resistance $R_\uparrow$. The illustration for parallel state (a) and antiparallel state (b) of the magnetizations demonstrates the different resulting resistances. (c) Local spin-valve signal in the nanoscale Si channel [2].

2.1.2. Spin injection and relaxation

The Fig. 2.2 illustrates the concept of spin injection and relaxation with spin diffusion length. The left of Fig. 2.2(a) describes the DOS of electron in the FM in equilibrium with a shifted DOS for spin-up and spin-down and an imbalance of the DOS $\nu_\uparrow > \nu_\downarrow$. The right of

Fig. 2.2 (a) describes the DOS of electron in a non-magnetic material (NM) in equilibrium with a balance of the DOS at E_F $\nu_\uparrow(E) = \nu_\downarrow(E)$. When electrons are injected from the FM into the NM, there is a spin accumulation close to the interface of FM and NM shown as a difference in DOS in the center of Fig. 2.2(a), because the spin imbalance of the FM is transferred into the NM. This is a non-equilibrium state at the interface of FM and NM, and the spin accumulation will diffuse from the interface into the bulk of the NM where there is no spin accumulation. During diffusion, spins relaxation will occur.

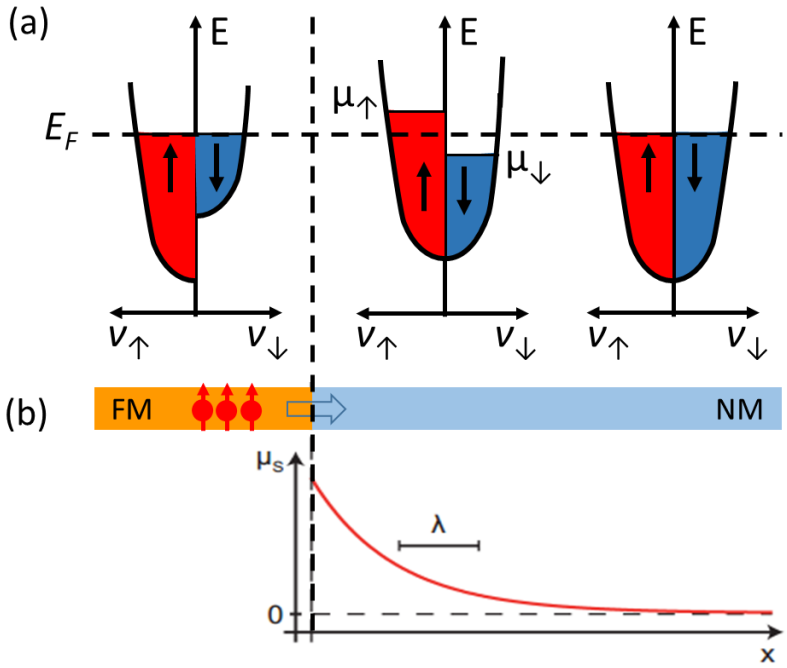

Figure 2.2: (a) Concept of spin injection and relaxation illustrated by the spin-dependent DOS of a FM and a NM in equilibrium (left and right, respectively) and the spin accumulation in the NM close to the interface when an electrons are injected from the FM into the NM (center). (b) The spin electrochemical potential μ_S in the NM decays as a function of the position x with the spin diffusion length λ [3].

Generally, the spin injection and transport from FM into NM can be characterized by applying the two-current model to define the spin current density $J_S = J_\uparrow - J_\downarrow$ and the charge current density $J = J_\uparrow + J_\downarrow$

$$J_{\uparrow,\downarrow} = -\frac{\sigma_{\uparrow,\downarrow}}{e}\nabla\mu_{\uparrow,\downarrow} \tag{2.2}$$

With $\mu_{\uparrow,\downarrow}$ is the spin-dependent electrochemical potentials of the electrons. The electrochemical potential $\mu_0 = \frac{1}{2}(\mu_\uparrow + \mu_\downarrow)$ and the spin electrochemical potential $\mu_S = \frac{1}{2}(\mu_\uparrow - \mu_\downarrow)$ describes the spin accumulation [3].

In the bulk of the FM, we have shown that $\sigma_\uparrow \neq \sigma_\downarrow$ as discussed in the previous section, the $J_\uparrow \neq J_\downarrow$, while in the bulk of the NM we have $J_\uparrow = J_\downarrow$. Therefore, spin accumulation builds up at the interface. The mechanism of this spin accumulation defined by the spin electrochemical potential μ_S is described by the Bloch equation [3]

$$\frac{d\overrightarrow{\mu_S}}{dt} = D\nabla^2\overrightarrow{\mu_S} - \frac{\overrightarrow{\mu_S}}{\tau} + \overrightarrow{\omega_L} \times \overrightarrow{\mu_S} \tag{2.3}$$

where D is the diffusion coefficient, τ is the spin relaxation time, $\omega_L = g\mu_B/\hbar\vec{B}$ is the Larmor frequency. $\vec{B}$ is the magnetic field with the gyromagnetic factor g (g-factor, g = 2 for free electrons) and the Bohr magneton μ_B.

The spin chemical potential $\overrightarrow{\mu_S}$ in this equation is a vector quantity, representing not only the spin chemical potential $\mu_\uparrow$ and $\mu_\downarrow$ with respect to the z-axis, but also the 3-dimensional spin accumulation. For $\vec{B} = 0$, the system is in a steady state with $\frac{d\overrightarrow{\mu_S}}{dt} = 0$, and with the

boundary condition $\mu_S(x \to \infty) = 0$ the spin accumulation exponentially decays away from the interface with $\mu_S \propto \exp(-\frac{x}{\lambda})$ where $\lambda = \sqrt{D\tau}$ is the spin diffusion length in the NM.

2.1.3. Conductivity mismatch problem

The conductivity mismatch problem is a crucial issue for attempts to efficiently inject spins into a diffusive transport channel. The first discussion about this fundamental problem in spin injection from FMs into semiconductors (SC) was raised by Schmidt *et al.* [4]. They explained that the difference in resistivity of the FM injector and the SC transport channel causes a vanishing polarization of the injected spins. Although it was shown that the mismatch can be circumvented when using a ferromagnetic SC material for spin injector, this injection method is limited to low temperatures, due to the very low Curie temperatures of these ferromagnetic SC materials.

According to the theory of spin transport in the diffusive transport regime [4,5], when spin polarized electrons are injected from FM into SC, without barrier between the FM layer and the SC channel, the spin polarization of the current at the FM/SC interface is given by

$$(\mathrm{SP})_I = \left(\frac{J_+ - J_-}{J_+ + J_-} \right)_I = \frac{\beta}{1 + r_N / r_F} . \qquad (2.4)$$

Here, β is the spin-polarization of the FM layer, r_F and r_N are characteristic resistances defined by $r_F = \rho_F \lambda_F$ and $r_N = \rho_N \lambda_N$, where ρ_F , ρ_N are the resistivity of the FM and SC, and λ_F, λ_N are the spin-diffusion length in FM and SC. The ratio r_N / r_F determines the spin polarization at the interface. Using $\rho_F \sim 1\times10^{-5}$ Ωcm and $\lambda_F \sim 2$ nm for Fe, $\rho_N = 2\times10^{-2}$ Ωcm

for n-Si (n =10^{18} cm^{-3}) and assuming that λ_N ~10 μm, the ratio r_N / r_F is as large as 1×10^7. This means that there is almost no spin polarization at the interface between Fe and n-Si. The situation is even worse for the spin-valve ratio in the FM/SC/FM structure. Assuming that the length of the SC layer $t_N \ll \lambda_N$, the spin-valve ratio is given by

$$\frac{\Delta R}{R} = 8\beta^2 \left(\frac{r_F}{r_N} \frac{l_{sf}^N}{t_N} \right)^2 \tag{2.5}$$

For the Fe/n-Si interface, even when t_N = 20 nm, the ratio $\left(\frac{r_F}{r_N} \frac{l_{sf}^N}{t_N} \right)^2$ is of the order of 10^{-9}, which means that there is almost no spin-valve effect.

The conductivity mismatch problem can be avoided by inserting a barrier between the FM and SC [5,6], which has been widely used to obtain spin injection into SC. However, this method still has some problems. While spin injection from FM into SC through a barrier has been definitely demonstrated, typical values of the spin-valve ratio reported so far in lateral devices are as small as 0.01% ~ 0.1%. Furthermore, high-resistance barriers at the source/drain electrodes are not desired from the viewpoint of current-driving capability of spin-transistors. On the other hand, the conductivity mismatch problem can also be avoided by using nano-scale SC channels with ballistic (or quasi-ballistic) transport. If the SC channel length is comparable or shorter than the electron mean free path, the transport regime changes from diffusive to (quasi) ballistic. In this case, the Ohm's law and diffusion equations used to derive the spin-polarized current are no longer valid. The transport in the SC channel may be modeled using quantum mechanics rather than classical transport equations of electrons.

In such a case, the transfer matrix method may be used to calculate the spin-polarized transport in the SC channel. Such a method was used to calculate the magnetocurrent in spin-MOSFETs in the original work by Tanaka and Sugahara [7].

2.2. Spin transport in the ballistic regime

The ballistic transport is the transport of electrons in the medium that can eliminate the electrical resistivity by scattering. If the length of the channel (L) is smaller than the mean free path (λ) of electrons, the ballistic transport could occur. In case of $L \sim \lambda$, we have the quasi-ballistic transport. In devices with submicron dimensions, this phenomena is especially true because λ for momentum scattering can easily exceed device dimensions. Moreover, if the conductor of such materials is narrow enough, it easily become quantum wires, where current is carried by only a small number of transverse subbands. In a sufficient short quantum wire, intersubband scattering becomes inconsequential and quantization of electrical conductance is manifested [8,9].

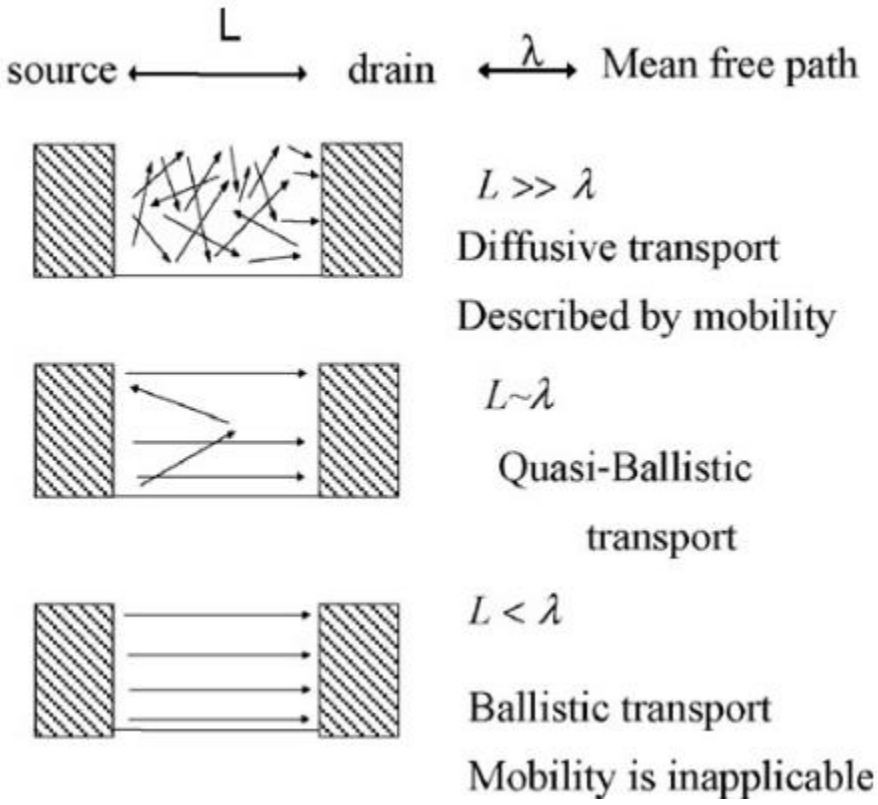

Figure 2.3: Carrier transport in channel depends on relative dimension of the device size and the mean free path [10]. Reprinted from Appl. Surf. Sci. 254, 6194 (2008), with the permission of Elsevier Publishing.

Bart van Wees and his colleagues discovered the quantization of the conductance in a two-dimensional electron gas (2DEG) in 1998 [8]. In that experiment, they manipulated the width of a channel where electrons flowed by applying a gate voltage to 2DEG, and observed a change of the conductance in a stepwise manner, with steps of ($2e^2/h$). This quantized conductance may be explained as follows. Restricted regions where a current flows may be considered to be pseudo-one-dimensional. The electronic state in such restricted regions is continuous along the current flow direction, but it is quantized perpendicular to the current

flow, with the quantization of the electronic state is identified by the Fermi wave-length λ_F. When the width of the restricted region is close to λ_F, only one state is available for electrons. As a result, two electrons (having up and down spins) may contribute to a current, making increase to a conductance of $\Gamma_0 = 2e^2/h$. If the width of the sample is expanded, the conductance increases stepwise in steps of $\Gamma = \left(\frac{2e^2}{h}\right) \times n$.

In the ballistic transport, each channel is characterized by the quantized conductance $\Gamma_0 = 2e^2/h$. Therefore, the total conductance may be given by

$$\Gamma = \sum_i \Gamma_0 \tau_i \qquad (2.6)$$

where τ_i is the transmission coefficient of the i^{th} channel. This conductance is independent of material conductance, thus it is possible to overcome the conductivity mismatch in the ballistic regime.

In fact, there are some experiments showing the promising magnetoresistance ratio in ballistic transport regime. An investigation of MR effect in Ni point contacts reported by García *et al.* [11] has shown that the MR ratio becomes large when the conductance approaches Γ_0. In that experiment, the maximum MR ratio was 280% (for the pessimistic definition). These results are shown in Fig. 2.4. The MR effect observed was termed as ballistic MR. Other researches conducted by Chopra and Hua [12,13] have reported that the MR ratio is 3000 – 10,000 % for usual point contacts of Ni or those produced by electrodeposition. However, the resistance in their measurements is only in range of 0.1 kΩ, which is much smaller than the inverse of the quantization conductance $\Gamma_0^{-1} = 12.9\ k\Omega$.

Therefore, the conductive properties of their samples might be different from those observed by García *et al.* For the vertical spin-valve structure, Pham *et al.* reports the large MR ratio of 8 % in the MnAs vertical spin-valve devices with MnAs nanoparticles at the bottom electrode. [14].

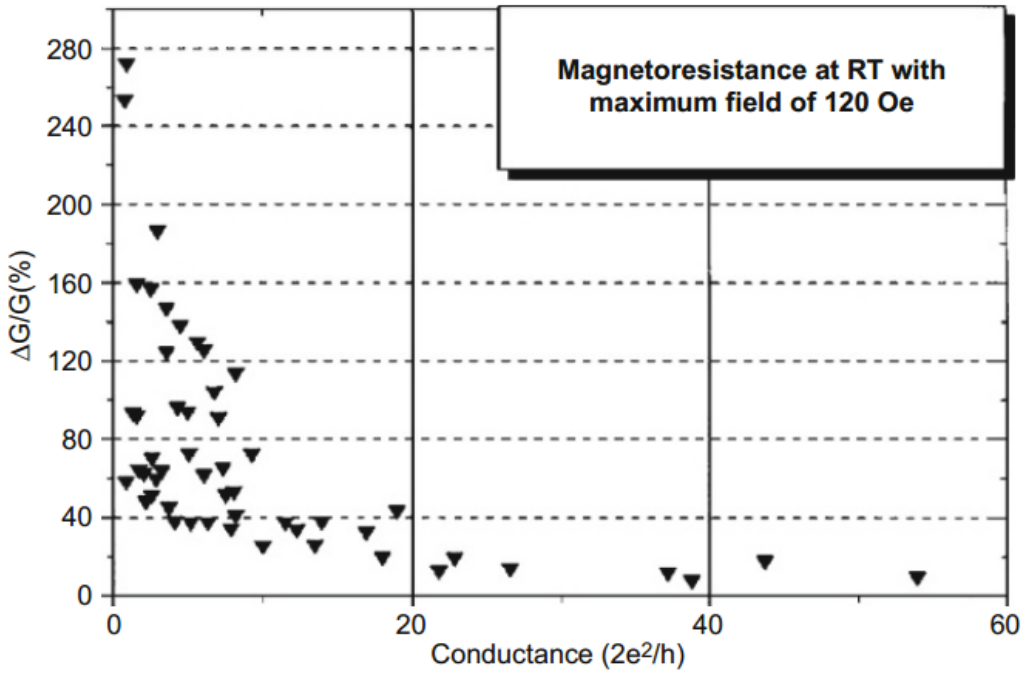

Figure 2.4: Experimental results of conductance change as a function of quantized conductance in Ni point contacts [11]. Reprinted from Phys. Rev. Lett. 82, 2923 (1999), with the permission of APS Publishing.

2.3. Electrical Spin Injection and Transport Measurements

This section describes the typical measurements used to investigate the spin transport phenomena. Basically, the mechanism of these measurements is investigation of

magnetoresistance, which is manifested as a change in the resistance (or voltage) across terminals at a certain magnetic field range (antiparallel magnetization of the two ferromagnetic electrodes).

2.3.1. Two-terminal local spin-valve

The mechanism of two-terminal local spin valve measurement is analogous to the metal based spin valves, in which spin polarized carriers are injected from a FM electrode (as an injector) into a non-magnetic semiconductor channel and detected by a second FM electrode (as a detector) that is placed within the spin diffusion length associated with the semiconductor material. The Fig. 2.5 sketches a typical two-terminal spin-valve measurement setup. Although this measurement can produce large spin signals (e.i. Large change in resistance or voltage) and is the simplest method to set up, it is also highly influenced by spurious effects. Therefore, it is necessary for a systematical investigation for the spin-valve device in case of using the two-terminal local spin-valve measurement.

According to Fert and Jaffers [5], it is possible to estimate the transverse spin relaxation time with channel length dependent magnetoresistance data by using these equations:

$$\Delta R = \frac{2(\beta r_F + \gamma r_b^*)^2}{(r_b^* + r_F) + \frac{r_N}{2}\left[1 + \left(\frac{r_b^*}{r_N}\right)^2\right]\frac{l_N}{\lambda_{sf}^N}}$$

$$R_P = 2(1-\beta^2)r_F + r_N\frac{l_N}{\lambda_{SF}^N} + 2(1-\gamma^2)r_b^* + 2\frac{(\beta-\gamma^2)r_F r_b^* + r_N(\beta^2 r_F + \gamma^2 r_b^*)\tanh\left(\frac{l_N}{2\lambda_{sf}^N}\right)}{(r_F + r_b^*) + r_N\tanh\left(\frac{l_N}{2\lambda_{sf}^N}\right)}$$

The ratio of $\Delta R/R_P$ is defined as the magnetoresistance. In the above formulas, β and γ are the bulk spin polarization and a spin-dependent tunneling parameter, respectively. l_N is the non-ferromagnetic channel length, r_F and r_N are the resistivity of the ferromagnetic electrode and non-ferromagnetic channel, respectively, and r_{b*} is the interface resistance of the tunnel barrier contact. While the four-terminal non-local measurements can provide conclusive evidence of spin injection, the two-terminal local measurements can still provide the maximum magnitude of spin response which is more applicable in practical devices.

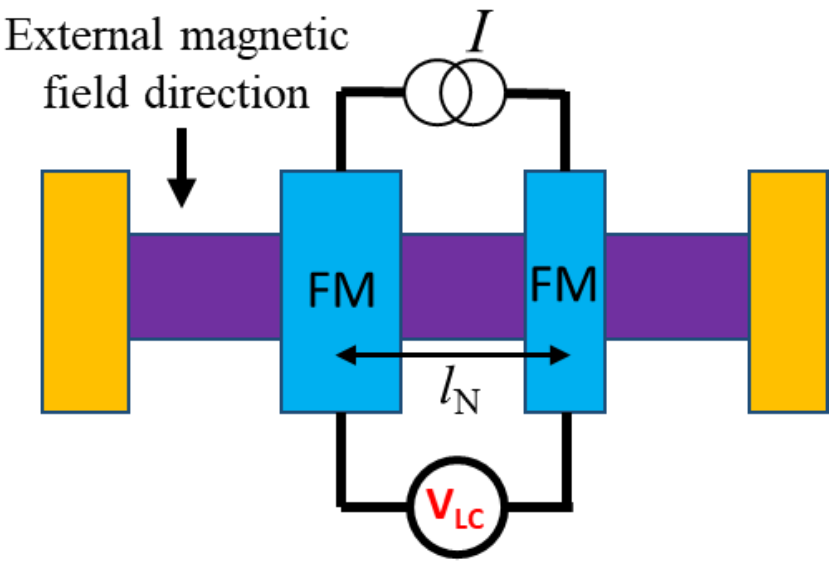

Figure 2.5: Two-terminal local spin-valve measurement scheme on a four-terminal lateral spin-valve. In this configuration, l_N is the channel length (center-to-center distance between the two ferromagnetic (FM) electrodes. For a constant current bias (or voltage bias) across the two FM electrodes, the voltage change (or current change) is measured as an external magnetic field is swept across the device. The outer two electrodes can either be a FM or non-magnetic ohmic contact.

2.3.2. Four-terminal non-local spin-valve

Different from the two-terminal local measurement which use the same injector / detector for spin and charge currents, the four-terminal non-local spin valve measurement separates the charge current path and the pure spin diffusion path, eliminating most of the spurious effects mentioned previously. Conventionally, it consists of two laterally separated FM electrodes placed on the SC channel as the injector and detector for spin current, and two outer reference ohmic contacts (either FM or non-magnetic) as shown in Fig. 2.6. In this measurement, the charge current flows from one of the FM electrode to its closest outermost reference contact, causing a non-equilibrium spin accumulation induced in the SC channel. The spin accumulation from the injecting FM electrode diffuses away from the injection point to both left and right directions and relaxes with a characteristics length known as the spin diffusion length. An adjacent detector FM electrode which is within the spin diffusion length will detect the diffused spin electrons outside of the electric current path. The spin signal which is considered as the voltage change when the injector and detector are in parallel and anti-parallel configuration can be defined as:

$$\Delta R = \frac{\Delta V}{I} = \frac{P_1 P_2 \lambda_s \rho}{A} \exp\left(-\frac{L}{\lambda_s}\right)$$

In the above formula, P_1 and P_2 are the spin polarization of the current across the interfaces of the (FM electrode-injector)/NM channel and NM channel/(FM electrode-detector), respectively, I is the electron injection current, ρ is the resistivity of the semiconductor, A is the cross junction area of the semiconductor, and L is the lateral distance between the two FM electrodes.

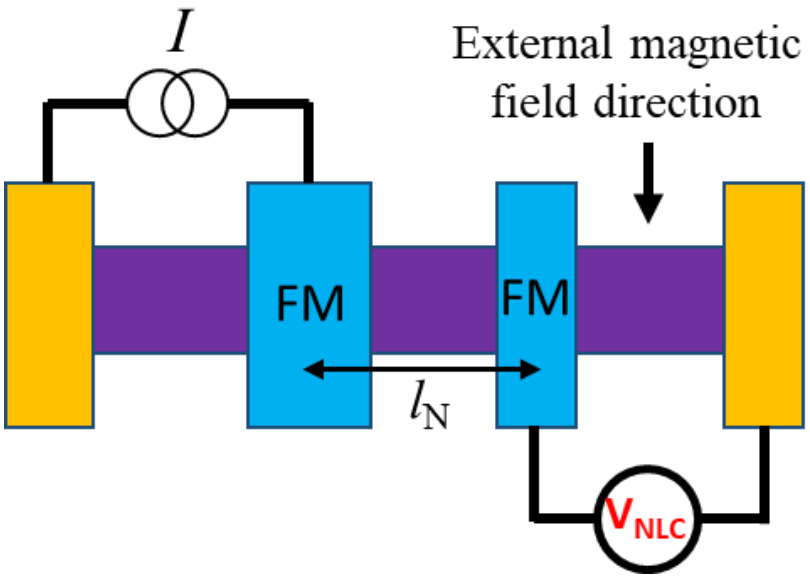

Figure 2.6: The configuration of a four-terminal non-local spin-valve measurement. The charge current is passed through the outer region on the left-side of the channel, while the right-side circuit with the FM detector is used to detect the diffused spin accumulation outside of the charge current path.

2.3.3 Three-terminal Hanle precession measurements

Different from both local and non-local spin-valve measurements, the three-terminal Hanle use a single FM electrode to observe the spin accumulation and precession. This measurement configuration consists of three terminals – two reference electrodes (either FM or non-magnetic) and one FM electrode. The injection of spin polarized carriers into a SC channel generates a net spin accumulation, resulting in splitting of the spin-dependent electrochemical potential: $\Delta\mu = \mu_\uparrow - \mu_\downarrow$. This splitting is detected as a voltage $\Delta V_{3T} = \gamma\Delta\mu/2q$, in which γ is the tunneling spin polarization of the FM tunnel contact. Under an out-of-plane magnetic field B_z applied with respect to the z axis, the spins precess at the

Larmor frequency $\omega_L = g\mu_B B_z/\hbar$, resulting in precessional dephasing of the net spin accumulation in the channel, where g is the Lande g-factor, μ_B is the Bohr magneton, and $\hbar$ is the reduced Planck's constant. This precessional dephasing manifests itself in a Lorentzian shaped data which can be defined by

$$V_{3T}(B_Z) = \Delta V_{3T}(0)/[1 + (\omega_L \tau_s)^2]$$

in which τ_s is the spin relaxation time. This measurement technique allows us to focus on and probe the characteristics of the spin system directly underneath the spin injecting contact.

However, there is a crucial issue that may prevent one from obtaining an accurate spin signal. Because this measurement uses the same electrode for both injection and detection of the spin accumulation and precession, the interface quality between the FM/SC becomes significantly important. According to Tran *et al.* [15], the spin polarized electrons can be trapped at the interface states or defect sites near the FM/SC interface, leading to longer spin lifetimes than what the actual value inside the SC channel and causing an overestimation of the spin lifetime value. There are methods to verify that interface states are not affecting the three-terminal signal. The first one is to change the doping of the SC channel and confirming the change in spin lifetimes. Conventionally, a lower doping concentration will cause a longer spin lifetimes due to decrease in scattering. Another method is to use several tunnel barrier materials. If the interface states or defect sites are not dominant in the observed spin signal, the spin lifetime should remain relatively constant across multiple tunnel barrier materials.

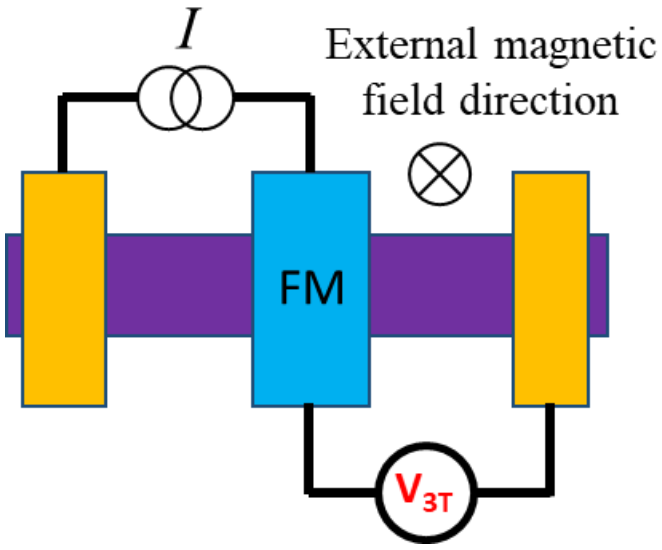

Figure 2.7: The configuration of a three-terminal Hanle measurement. Spin injection and detection is experienced by a single FM electrode. The outer two contacts are ohmic reference contacts. The magnetic field is swept orthogonal to the sample surface.

2.4. Summary

This chapter introduces the overviews of the spin transport mechanisms in diffusive regime with the conductivity mismatch issue and ballistic regime with advantages to overcome that issue. Electrical spin measurements techniques were discussed as well. An understanding of the physical mechanisms that govern spin transport inside various semiconductors is essential for proper design and characterization of these devices, as well as for overcoming the issue of conductivity mismatch.

References

1. Valet, T. & Fert, A. Theory of the perpendicular magnetoresistance in magnetic multilayers. *Phys. Rev. B* **48,** 7099–7113 (1993).
2. Hiep, D. D., Tanaka, M. & Hai, P. N. Spin transport in nanoscale Si-based spin-valve devices. *Appl. Phys. Lett.* **109,** 232402 (2016).
3. Fabian, J., Matos-Abiague, A., Ertler, C., Stano, P. & Zutic, I. Semiconductor Spintronics. *Acta Phys. Slovaca* **57,** 565–907 (2007).
4. Schmidt, G., Ferrand, D., Molenkamp, L. W., Filip, A. T. & van Wees, B. J. Fundamental obstacle for electrical spin injection from a ferromagnetic metal into a diffusive semiconductor. *Phys. Rev. B* **62,** R4790–R4793 (2000).
5. Fert, A. & Jaffrès, H. Conditions for efficient spin injection from a ferromagnetic metal into a semiconductor. *Phys. Rev. B* **64,** 184420 (2001).
6. Rashba, E. I. Theory of electrical spin injection: Tunnel contacts as a solution of the conductivity mismatch problem. *Phys. Rev. B* **62,** R16267–R16270 (2000).
7. Sugahara, S. & Tanaka, M. A spin metal–oxide–semiconductor field-effect transistor using half-metallic-ferromagnet contacts for the source and drain. *Appl. Phys. Lett.* **84,** 2307–2309 (2004).
8. van Wees, B. J. *et al.* Quantized conductance of point contacts in a two-dimensional electron gas. *Phys. Rev. Lett.* **60,** 848–850 (1988).
9. Wharam, D. A. *et al.* One-dimensional transport and the quantisation of the ballistic resistance. *J. Phys. C Solid State Phys.* **21,** L209–L214 (1988).
10. Natori, K. Ballistic/quasi-ballistic transport in nanoscale transistor. *Appl. Surf. Sci.*

254, 6194–6198 (2008).

11. García, N., Muñoz, M. & Zhao, Y.-W. Magnetoresistance in excess of 200 % in Ballistic Ni Nanocontacts at Room Temperature and 100 Oe. *Phys. Rev. Lett.* **82,** 2923–2926 (1999).
12. Chopra, H. D. & Hua, S. Z. Ballistic magnetoresistance over 3000% in Ni nanocontacts at room temperature. *Phys. Rev. B* **66,** 020403 (2002).
13. Hua, S. Z. & Chopra, H. D. 100,000 % ballistic magnetoresistance in stable Ni nanocontacts at room temperature. *Phys. Rev. B* **67,** 060401 (2003).
14. Hai, P. N., Sakata, Y., Yokoyama, M., Ohya, S. & Tanaka, M. Spin-valve effect by ballistic transport in ferromagnetic metal (MnAs)/semiconductor (GaAs) hybrid heterostructures. *Phys. Rev. B - Condens. Matter Mater. Phys.* **77,** 1–6 (2008).
15. Tran, M. *et al.* Enhancement of the spin accumulation at the interface between a spin-polarized tunnel junction and a semiconductor. *Phys. Rev. Lett.* **102,** 1–4 (2009).

CHAPTER 3

DEVICE FABRICATION and CHARACTERIZATION

This chapter describes the fabrication process and characterizations of devices in this study. Several techniques were used and a large number of samples were fabricated. This chapter is aimed at providing an insight into the fabrication and characterization of Si-based nanoscale spin-valve devices.

3.1. Techniques

In this research, I employ 5 main techniques to fabricate the Si-based nanoscale spin-valve devices. They are Electron Beam (EB) Evaporation and Molecular Beam Epitaxy (MBE) for depositing ferromagnetic (FM) and tunnel barrier layers, Electron Beam Lithography (EBL) for the nanoscale mask design, ion milling technique for patterning the nanoscale Si channel, and photolithography to fabricate the measurement electrodes.

- **Electron Beam Evaporation**

EB Evaporation or Electron Beam Physical Vapor Deposition is a material deposition method in which a target anode is bombarded with an electron beam emitted from a charged tungsten filament under high vacuum. The target material is heated by this electron beam and transformed into the gaseous phase, then evaporated in the vacuum chamber, and coating the in-situ sample. In this study, I used the ULVAC EB evaporator.

- **Molecular-beam Epitaxy**

MBE is an epitaxy method for deposition of high quality crystalized thin film, which is normally operated in high or ultra-high vacuum of 10^{-6} – 10^{-10} Pa. In this research, I use a custom-made MBE system with the based pressure of 10^{-8} Pa. In the MBE chamber, there are different material sources in the so-called effusion cells. From these cells, the materials are heated and evaporated, then the molecules land on the surface of sample to form thin films. The most importance of MBE is the low deposition rate that allows the films to grow epitaxially and low impurity concentration.

- **Electron beam lithography**

EBL is an important technique in nanotechnology. In this technique, a focused beam of electrons is used to pattern features down to sub-10 nm on a surface covered with an electron-sensitive film called a resist. The electron beam changes the solubility of the resist, enabling selective removal of either the exposed or non-exposed regions of the resist by immersing it in a developer. In this research, the EBL technique was employed to pattern the 20 nm Si spin-valve devices. In this study, I used the Hitachi S-4500 EBL system which is both EBL and Scanning Electron Microscope (SEM) machine. In this

EBL process, the mixer of ZEP-520A and ZEP-A in 1:1 ratio was used as electron beam resist.

- **Ion milling technique**

Ion Milling is a physical etching technique whereby the beam of high-energy Ar ions bombard into a substrate in vacuum in order to erode the surface to some desired depth or under-layer. [VLSI electronics Microstructure Science, volume 8, chapter 11, 1984]

- **Photolithography**

Photolithography technique is widely used in microfabrication to design the microscale structures. In this technique, the ultra-violet light is used to project a geometric structure onto a photoresist surface, which is a light-sensitive chemical, by a photomask. The surface then is undergone some chemical treatments to remove the un-needed area, to get the desired structure. In this study, I use OFPR-54CP as the photoresist.

3.2. Fabrication process

Si-based nanoscale 2 terminal spin valve device

A schematic drawing of the Si-based nanoscale 2 terminal spin-valve device is shown in figure 2.1.

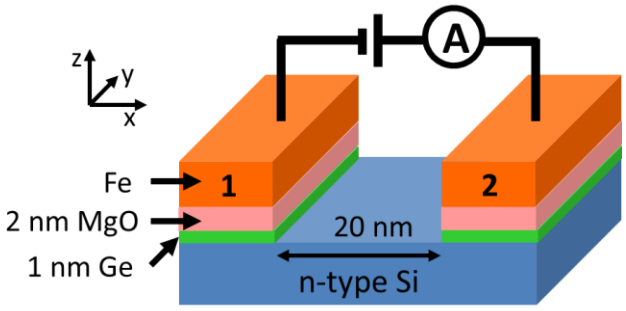

Figure 2.1: A schematic drawing of the Si-based nanoscale 2 terminal spin-valve device

The basic process flow for a local spin valve device is shown in figure 2.2. Firstly, the Si substrate is prepared by standard cleaning process of acetone – H_2SO_4 – BHF to remove the native SiO_2 on surface.

Secondly, the samples were introduced into the ultra-high vacuum to deposit the FM and tunnel barrier layers. In this step, I have fabricated 2 series of samples with similar structure but by different deposition method: EB evaporation and MBE.

The third step is creating the 20 nm Si channel by EBL and ion milling techniques. In this step, I have used EBL to pattern 30 nm-thick Au hard masks with a 20 nm-long and 100 nm-wide gap in between, followed by using Ar ion milling to etch the exposed Fe area and define a 20 nm-long Si channel.

Finally, I have used the photolithography, EB evaporation and liftoff techniques to fabricate the Au (40 nm) / Cr (5 nm) pad as the measurement electrodes.

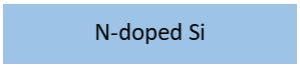

1. The Si substrate after the cleaning process of acetone – H_2SO_4 – BHF.

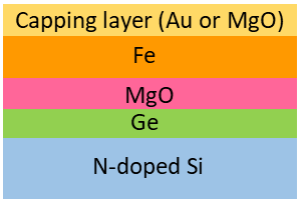

2. Deposition of the Ge/MgO double tunnel barrier and Fe electrode layers by EB evaporation or MBE.

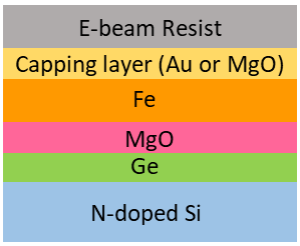

3. ZEP-520A resist is spin coated on the sample and baked at 180^0C in 4 minutes to prepare for the EBL process.

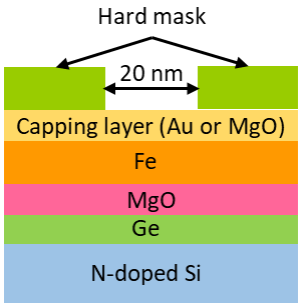

4. The EBL process, hard mask deposition and lift-off process is conducted for the hard mask fabrication.

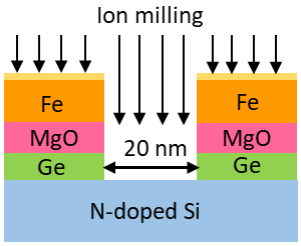

5. The ion milling process is conducted to etch the sample surface to define the nanoscale Si channel. The exposed Fe area is eroded to form the 20 nm-long Si channel. The area covered by hard mask is protected to become the FM electrodes.

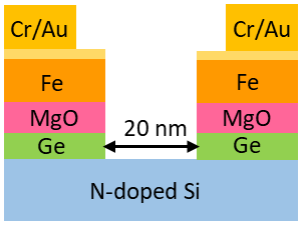

6. Finally, the photolithography, EB evaporation and liftoff techniques is conducted to fabricate the Au/Cr (40nm/5nm) pad as the measurement electrodes.

Figure 2.2: The fabrication process for a local spin valve device

3.3. Substrate preparation

In this research, the highly doped n-type Si (100) substrates with electron density $n = 1 \times 10^{18}$ cm^{-3} were used. In order to get a clean sample for the fabrication process, 3 kinds of cleaning process were employed: standard cleaning process (with acetone, isopropanol (IPA), and deionized water (DI water)) and Piranha cleaning process (with H_2O_2 and H_2SO_4) to remove dust and organic element. Finally, the BHF etching process was used to remove the native oxide layer on the surface of sample before doing the fabrication process. The sample preparation is as follow.

- Si substrates were cut into appropriate size, e.g. square 20 mm on a side.
- Standard cleaning of acetone – isopropyl alcohol (IPA) – DI water with ultrasonic in 2 minutes in each.
- Piranha cleaning process (H_2SO_4:H_2O_2 in 1:1 ratio). Samples are dipped in Piranha solution in 10 minutes, then rinsed in DI water in 10 minutes, followed by drying with air gun.
- BHF etching process to remove the native oxide layer on surface of sample. Samples are dipped in BHF in 90 seconds, then rinsed in DI water, followed by drying with air gun. Samples are ready for the deposition step.

3.4. FM electrodes and tunnel barriers deposition

After the cleaning process, the samples were introduced into ultra-high vacuum to deposit the FM and tunnel barrier layers. We have fabricated 2 series of sample with similar structure but by different deposition method: Electron-Beam (EB) evaporation and Molecular-Beam-Epitaxy (MBE).

3.4.1. EB evaporation of the FM electrodes and tunnel barriers

The 1st series were fabricated by the EB evaporation method. After the cleaning process, the samples were introduced into an ultra-high-vacuum EB evaporation chamber with the base pressure of 8×10^{-6} Pa to deposit the 10 nm Fe layer and finally capped with a 3 nm Au thin film. In order to enhance the spin injection efficiency from Fe to Si, I inserted an MgO/Ge double layer between the Fe electrodes and Si substrates. According to literature, MgO is a promising spin-dependent tunnel barrier for efficient spin injection from ferromagnetic electrode into semiconductors (SCs) [1,2]. However, it is difficult to grow a very thin MgO layer with a thickness of 1~2 nm on Si at room temperature for using as a tunnel barrier. On the other hand, epitaxial growth of MgO on Ge has been reported [3,4]. Moreover, deposition of smooth thin film of Ge on Si has been demonstrated at low deposition temperature [5]. Therefore, in these studies I decided to employ an ultra-thin film of Ge as a buffer layer between MgO and Si to improve the quality of MgO layer grown at room temperature. In order to investigate the role of the MgO/Ge double layer comparing with conventional MgO single barrier, I have prepared 3 spin-valve device structures; Device 1 with Fe electrodes deposited directly on the Si channel; Device 2 with 2 nm MgO inserted between Fe electrodes and Si channel; and Device 3 with an 2 nm-thick MgO / 1 nm-thick Ge double layer as the tunnel barrier. Figure 1(a) shows the schematic structure of device 3 with (2 nm MgO / 1 nm Ge) double tunnel barriers. All of the deposition processes have been conducted in the same EB evaporation chamber without breaking the vacuum.

3.4.2. MBE growth of the FM electrodes and tunnel barriers

In the second deposition method, I grew the tunnel barrier and Fe electrode layers by MBE in order to improve the crystal quality of Fe electrode and tunnel barrier layers. After the cleaning process, Si substrates were introduced into a MBE chamber with a base pressure of 1×10^{-8} Pa for growing the multilayers stack of Fe electrode and tunnel barrier. In this research, I have grown 2 series of sample by MBE method. In the first one, in order to investigate the spin transport in nanoscale Si channel at different thickness of MgO tunnel barrier layer, I grew the stack of 1 nm Ge / (1.5 – 3.5 nm) MgO tunnel barrier / 10 nm Fe

layer, and finally capping by 1.1 nm MgO layer. In the second one, in order to enhance the spin injection in our spin-valve devices by prevent the magnetically-dead layer arise between Fe and MgO layers, I have inserted an Mg buffer layer in between them. I grew the stack of 1 nm Ge / (1.5 – 3.5 nm) MgO tunnel barrier / 1 nm Mg / 10 nm Fe / 1.1 nm MgO layer. Knudsen cells were used for thermal evaporation of Ge and Fe, while a low-power electron-beam evaporator was used to deposit MgO with a slow rate of 0.03 Å/s. The X-ray diffraction has been employed to investigate the crystal quality of the tunnel barrier, and has confirmed the crystal orientation of Fe(110) || MgO(001) || Ge(001) in the MBE grown samples. Therefore, I expect that the crystal quality of the MBE-grown MgO/Ge double layer is much better than that grown by EB evaporation.

3.5. Fabrication of nanoscale Si channel

After deposit the tunnel barrier and FM layers, I used the EBL, EB evaporation and ion milling techniques in order to create the 20 nm Si channel. In this step, the EBL and EB evaporation processes are used to make the hard mask on the prepared sample. The e-beam resist (mixer of ZEP-520A and ZEP-A in 1:1 ratio) is spin coated onto the sample with the thickness of 200 nm. Then, the sample is baked at 180^0C in 4 minutes by a hot plate, followed by transferring into the EBL chamber for EB exposure. Next, the sample is developed in the developer ZED-N50 in 4 minutes and rinsed in ZMD-B to dissolve the exposed resist. After developing, the sample is transferred into the high vacuum EB evaporation chamber to deposit hard mask. For samples capped by 3 nm Au, the hard mask is 30 nm Au; for samples capped by 1 nm MgO, the hard mask is (5 nm Cr / 35 nm Au). The lift-off process was carried out in N,N-Dimethylformamide at 80^0C in 30 minutes, followed with aceton, IPA and DI water. Finally, I employed the Ar ion milling method to etch away the exposed Fe area and define a 20 nm-long Si channel. Figure 2.3 shows the spin-valve device with Fe electrodes as the spin injector / detector and the 20 nm Si channel in between.

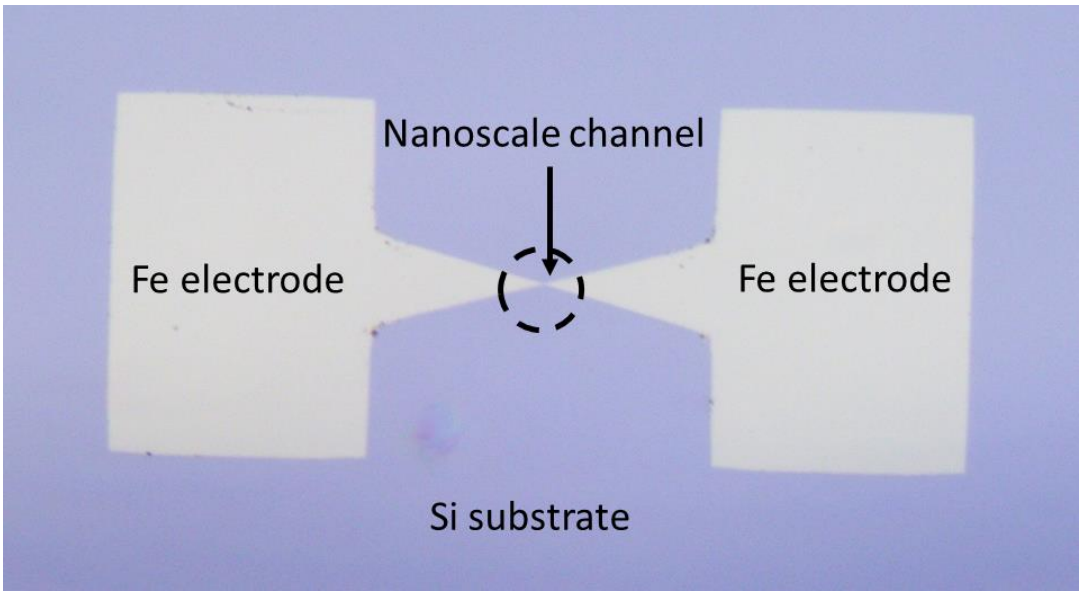

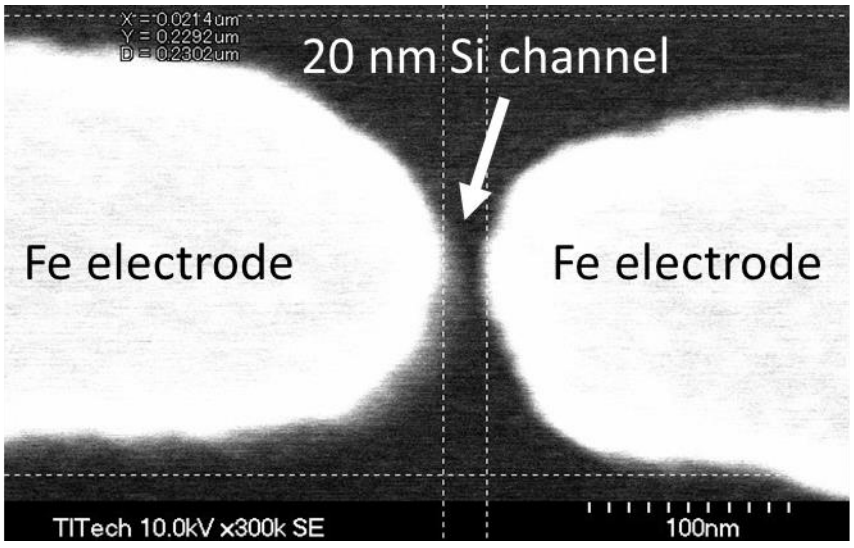

Figure 2.3: a) The spin-valve device with Fe electrodes as the spin injector / detector and a 20 nm Si channel in between. b) The scanning electron microscope (SEM) image of the 20 nm Si channel.

3.6. Connecting the spin-valve device to the microscale contacts

For characterization, it is necessary to connect the spin-valve device to micro contacts for spin-valve measurement. In order to fabricate the contacts, the photolithography, EB evaporation and lift-off techniques were used.

Firstly, the photoresist (OFPR-54CP) is spin coated onto the sample at 500 rpm – 5 sec and 5000 rpm – 30 sec. Then, the sample is soft baked at 110^0C in 3 minutes by a hot plate, followed by transferring into the photolithography chamber for exposure. Next, the sample is developed in the developer NMD-3 in 90 sec and rinsed in DI water in 2 minutes to dissolve the exposed resist. After developing, the sample is transferred into the high vacuum EB evaporation chamber to deposit the Au (40 nm) / Cr (5 nm) pad electrodes. The lift-off process was carried out in N,N-Dimethylformamide at 80^0C in 30 minutes, followed with aceton, IPA, DI water and drying by air gun to obtain the final Si-based spin-valve device as shown in Fig. 2.4. The sample is ready for measurements.

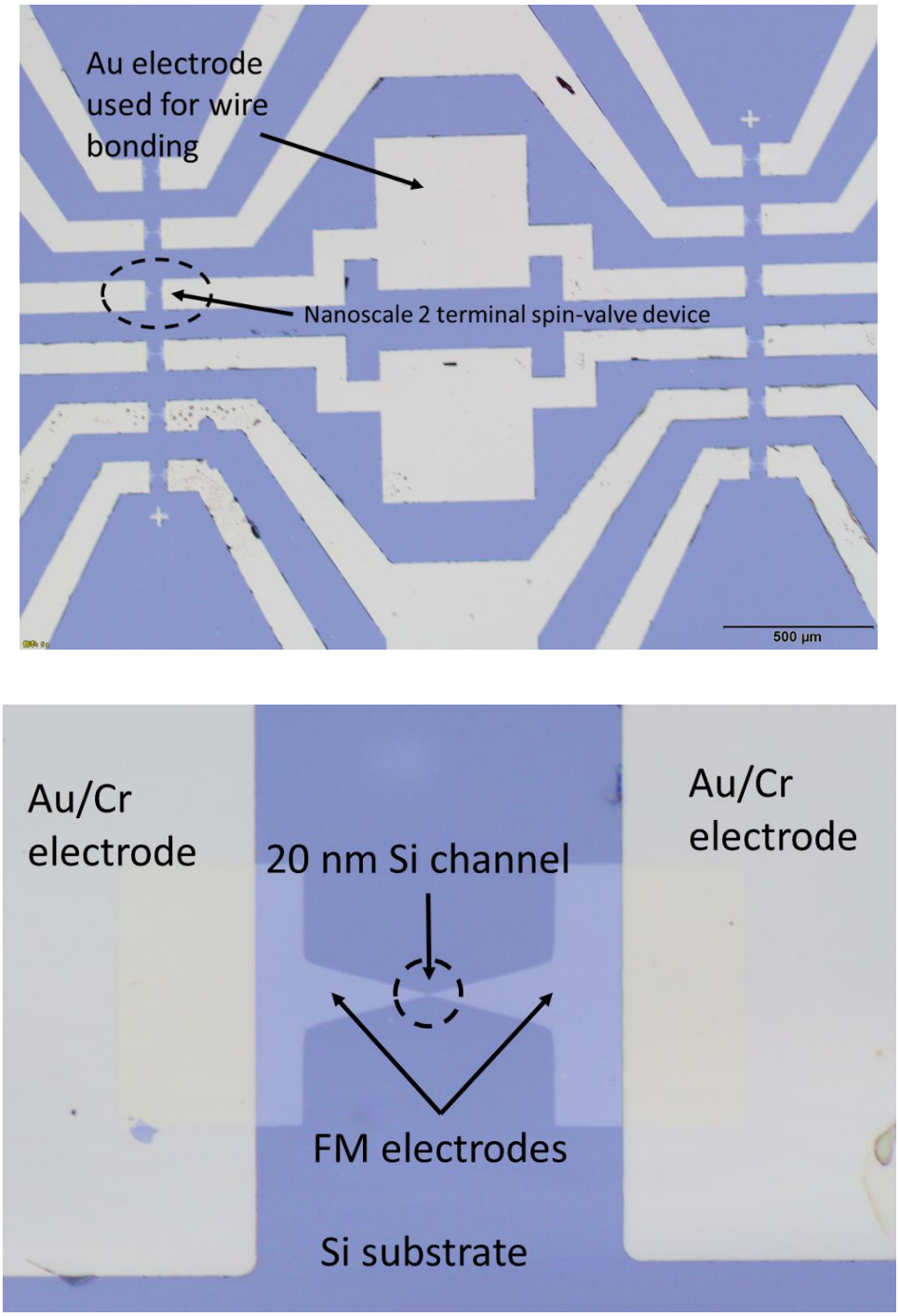

Figure 2.4: The final 2 terminal spin-valve devices after fabrication process.

3.7. Wire bonding

Because the spin-valve effect measurement is conducted in the cryostat at low temperature, the final step before measurement is the wire-bonding of sample onto the cryostat sample holder, and wire bonding is used for this purpose. In this step, instead of using a wire bonder whose ultrasonic wave has high possibility to break the nanoscale device, the portable soldering iron and indium were used to weld the gold wire connecting the devices and cryostat sample holder. This bonding method has 100% of success, and does not break any device.

3.8. Characterization

3.8.1. Local magneto-transport measurement

In conventional two-terminal spin-valve effect measurements, the spin-injecting and spin-detecting terminals are the same. Thus, they suffer from parasitic local magnetoresistance effects, such as the anisotropic magnetoresistance (AMR) effect of the FM electrodes and the tunneling anisotropic magnetoresistance (TAMR) effect at the FM / SC interfaces. To avoid such local effects, two well-known methods have been used to detect intrinsic spin transport in mm-long SC channels. One method is to observe the non-local spin-valve effect in a four terminal configuration, where the spin-injecting terminals and the spin-detecting terminals are different. If the distance l between the spin-injecting and spin-detecting terminals is far enough compared with the depth d of the SC channel where the electric current flows, then the spin-detecting terminal voltage will not be affected by local effects and can detect a pure spin current [6]. However, if l is comparable or shorter than d, the non-local voltage is also affected by local effects as shown by careful experiments and device simulations [7]. As a result, the four-terminal configuration has no advantage over the two-terminal configuration in our case of nano-scale SC channels, because both methods suffer from local effects. Another method is to observe spin precession when the spin-polarized electrons diffuse through the SC channel under an applied magnetic field (the Hanle

effect) [8]. In this method, however, the SC channels have to be long enough so that considerable spin precession can occur. Therefore, the Hanle effect cannot be used in my 20 nm-long Si channels, where the spin precession is negligible. Finally, I note that any realistic nano-scale spin MOSFETs should operate only with source and drain electrodes, corresponding to the two terminal configuration. Taking the above into consideration, I conclude that the two-terminal spin-valve effect measurement is a realistic way to detect the spin transport in our devices, even though this method suffers from local effects. To distinguish the intrinsic spin-valve effect from the parasitic local effects in the two-terminal configuration, I systematically investigated the bias voltage dependence, temperature dependence, and magnetic-field direction dependence of MR in our devices. The figure 2.5 shows the 2 terminal local spin-valve measurement configuration. In this measurement, I used a JANIS liquid He cryostat system for low temperature measurement and a Keithley 2400 SourceMeter as the DC voltage source and current meter.

3.8.2. Cryostat system

In this study, a cryogenic magneto resistance measurement system is used. In the liquid helium cryostat, there are a sample chamber inside and vacuum chamber outside which isolated to each other. The liquid helium can be injected into the sample chamber inside to decrease the sample temperature to maximum of 4.3 K. The outside vacuum chamber is used to isolate the sample chamber to from the outside world.

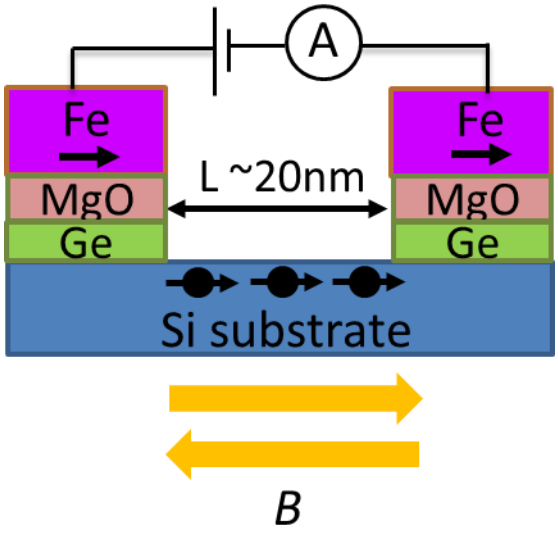

Figure 2.5: The 2 terminal local spin-valve measurement configuration.

3.9. Summary

This chapter describes the fabrication process and characterization of device used in this study. After introducing the general concept of techniques mainly used in this research such as EB evaporation, MBE, EBL, ion milling, and photolithography, I discuss about the process flow which is used for device fabrication, from the beginning of substrate preparation, FM electrodes and tunnel barriers deposition, fabrication of nanoscale Si channel, connecting the spin-valve device to the microscale contacts, to the last step is wire bonding on chip carrier. In the end of the chapter, the setups and techniques used to measure our devices are briefly discussed.

References

1. Jiang, X. *et al.* Highly Spin-Polarized Room-Temperature Tunnel Injector for Semiconductor Spintronics using MgO(100). *Phys. Rev. Lett.* **94,** 056601 (2005).

2. Martínez Boubeta, C. *et al.* Epitaxial Fe/MgO heterostructures on GaAs(001). *J. Cryst. Growth* **226,** 223–230 (2001).

3. Jeon, K.-R., Park, C.-Y. & Shin, S.-C. Epitaxial Growth of MgO and CoFe/MgO on Ge(001) Substrates by Molecular Beam Epitaxy. *Cryst. Growth Des.* **10,** 1346–1350 (2010).

4. Han, W. *et al.* Growth of single-crystalline, atomically smooth MgO films on Ge(001) by molecular beam epitaxy. *J. Cryst. Growth* **312,** 44–47 (2009).

5. Schöllhorn, C., Oehme, M., Bauer, M. & Kasper, E. Coalescence of germanium islands on silicon. *Thin Solid Films* **336,** 109–111 (1998).

6. Lou, X. *et al.* Electrical detection of spin transport in lateral ferromagnet–semiconductor devices. *Nat. Phys.* **3,** 197–202 (2007).

7. Nakane, R., Sato, S., Kokutani, S. & Tanaka, M. Appearance of anisotropic magnetoresistance and electric potential distribution in Si-based multiterminal devices with Fe electrodes. *IEEE Magn. Lett.* **3,** (2012).

8. Johnson, M. & Silsbee, R. H. Interfacial charge-spin coupling: Injection and detection of spin magnetization in metals. *Phys. Rev. Lett.* **55,** 1790–1793 (1985).

CHAPTER 4

INVESTIGATION of SPIN-VALVE DEVICES FABRICATED by ELECTRON BEAM EVAPORATION

In this chapter, the investigation of the spin transport in nanoscale silicon (Si)-based spin-valve devices with Fe electrodes, MgO/Ge tunnel barriers, and a 20 nm-long Si channel was conducted. I observed a clear spin-valve effect when a magnetic field was applied in the film plane along and perpendicular to the Si channel transport direction. Systematic investigations of the bias voltage dependence, temperature dependence, and magnetic-field direction dependence of the magnetoresistance indicate that the observed spin-valve effect is governed by the spin transport through the nanoscale Si channel. The spin-valve effect remains observable up to 200 K. For the device with MgO/Ge tunnel barriers, with a bias voltage of 1.7 V at 50 K, the spin-dependent output voltage is 13 mV, which is among the highest values reported so far. The results in this chapter have been published on APL **109**, 232402 (2016).

Chapter 4

4.1. Spin-valve device structures

The nanoscale spin-valve devices were fabricated on a highly doped n-type Si (100) substrate with an electron density $n = 1 \times 10^{18}$ cm^{-3}. The Si substrates were cleaned by acetone – H_2SO_4/H_2O_2 – BHF, then rinsed in DI water. After that, the samples were introduced into an ultra-high-vacuum electron-beam (EB) evaporation chamber to deposit a 10 nm Fe layer, and finally capped with a 3 nm Au layer.

To enhance the spin injection efficiency from Fe to Si, I inserted an MgO/Ge double layer between the Fe electrodes and Si substrates. Recently, a number of studies have shown that MgO is a promising tunnel barrier for efficient spin injection to semiconductors (SCs) [1,2]. While it is known that one can grow a relatively thick (~10 nm) MgO layer of good quality on Si at high growth temperature (~ 300 ^oC) [3], it is difficult to grow a very thin MgO layer with a thickness of 1~2 nm on Si at room temperature for use as a tunnel barrier. On the other hand, epitaxial growth of MgO on Ge has been reported [4,5]. Moreover, deposition of smooth thin film of Ge on Si has been demonstrated at low deposition temperature [6]. In this work, to improve the quality of MgO layer at room temperature, I employed an ultra-thin film of Ge as a buffer layer between MgO and Si. In order to investigate the role of the MgO/Ge double layer comparing with conventional MgO single barrier, 3 spin-valve device structures have been prepared; Device 1 with Fe electrodes deposited directly on the Si channel; Device 2 with 2 nm MgO inserted between Fe electrodes and Si channel; and Device 3 with an 2 nm-thick MgO / 1 nm-thick Ge double layer as the tunnel barrier. Figure 4.1 shows the schematic structure of 3 devices with different tunnel barriers.

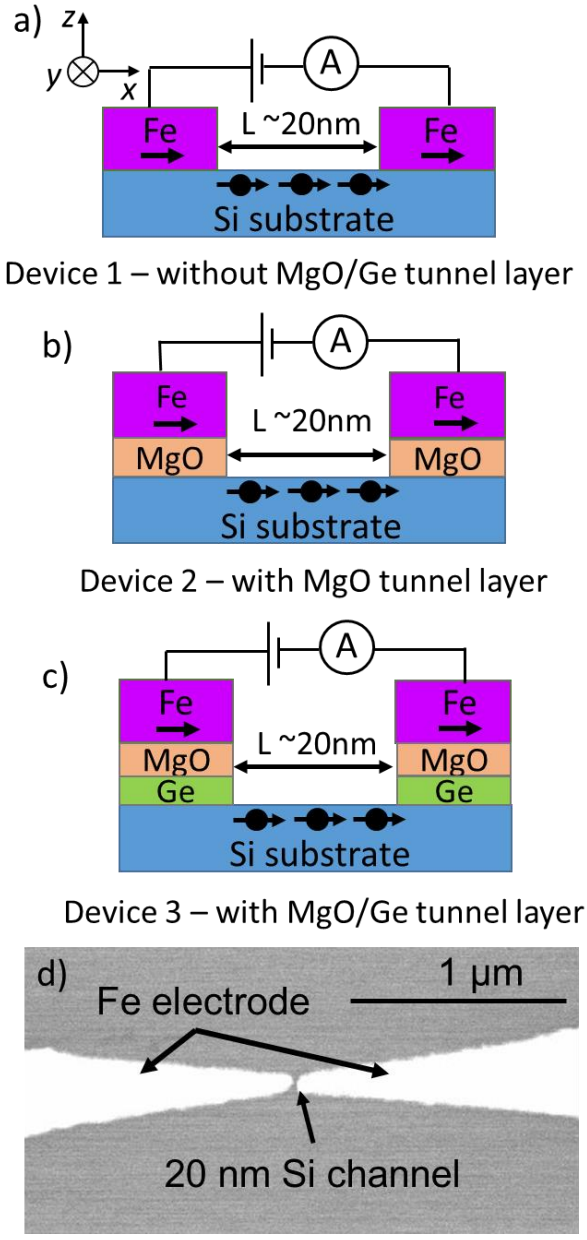

Figure 4.1: The schematic spin-valve device structures used in this chapter. (a) Device 1 with Fe electrodes deposited directly on the Si channel; (b) Device 2 with 2 nm MgO tunnel barrier; (c) Device 3 with a 2 nm-thick MgO / 1 nm-thick Ge double tunnel barrier; and (d) SEM image of Device 3.

After depositing the tunnel barrier and FM layer, e-beam lithography (EBL) and ion-milling techniques were used to fabricate nanoscale Si spin-valve devices. Finally, I fabricated Au (40 nm) / Cr (5 nm) pad electrodes by EB evaporation and standard photolithography. Figure 4.1(d) shows a top-view image of Device 3 taken by scanning electron microscopy (SEM). A Si channel with a length of 20 nm and a width of 100 nm was formed between the Fe electrodes. Note that although the shape of the Fe electrodes looks symmetric, their coercive forces can be different. The coercive forces of Fe electrodes are determined by the domain wall pinning potential at grain boundaries or defects. In reality, details of such grain boundaries or defects are not exactly the same in the left and right electrodes, which results in different coercive forces. Indeed, I found that the coercive force differs by 200 G, as shown later. This small difference establishes a narrow range of magnetic field where the anti-parallel magnetization configuration is realized, thus the spin-valve effect is observed.

4.2. Conductance characteristics

In this section, the conductance characteristics of the Si-based nanoscale 2 terminal spin-valve device fabricated by EB evaporation method is investigated.

Firstly, I measure the current – voltage characteristics (*I-V* curves) of the devices. Figure 4.2 shows the *I-V* curves and the resistances of Device 3 at different temperatures. In the figure 4.2(a), the *I-V* curves clearly show non-linear dependence of the current on the bias

voltage, indicating that the current is governed by the tunneling process at the Fe/MgO/Ge/Si interfaces. Furthermore, the strong temperature dependence of the *I*-*V* curves was also observed. At low temperatures, thermionic emission of electrons from the Fe electrodes to the Si over the tunnel barrier is suppressed. In addition, free carriers in the Si channel are partly quenched. Therefore, the current becomes smaller at low temperatures. This suggests that the resistance of the device is dominated by the transport through the spin-valve structure consisting of Fe(interface)/(MgO/Ge)/Si/(Ge/MgO)/Fe(interface). In reality, however, there is always contribution of the parasitic resistance of the Fe electrodes, especially at low bias voltages. In general, the resistance R can be decomposed into two components: $R = R_{Fe} + R_{sv}$, where R_{Fe} is the parasitic resistance of the Fe electrodes and R_{sv} is the resistance of the Fe(interface)/(MgO/Ge)/Si/(Ge/MgO)/Fe(interface) spin-valve structure. In order to quantitatively estimate the contribution of R_{Fe}, I have measured the dependence of R on temperature from 300 K to 4.3 K which is plotted in the Fig. 4.2(b). Here, R is measured at V = 20 mV. As temperature decreases, R increases rapidly. From this data, the ratio R_{Fe}/R could be estimated as follows. Since the parasitic $R_{Fe}(T)$ decreases as temperature decreases, $R_{Fe}(T) \leq R_{Fe}(300\text{K}) < R(300\text{K})$. Therefore, $R_{Fe}(T)/R(T)$ should be smaller than $R(300\text{K})/R(T)$. From this consideration, it is reasonable to estimate that R_{Fe}/R is smaller than 4% and 9% at 4.3 K and 200 K, respectively. This estimation will be used to distinguish the intrinsic spin-valve effect from parasitic local magnetoresistance (MR) effects of the Fe electrodes, as discussed later.

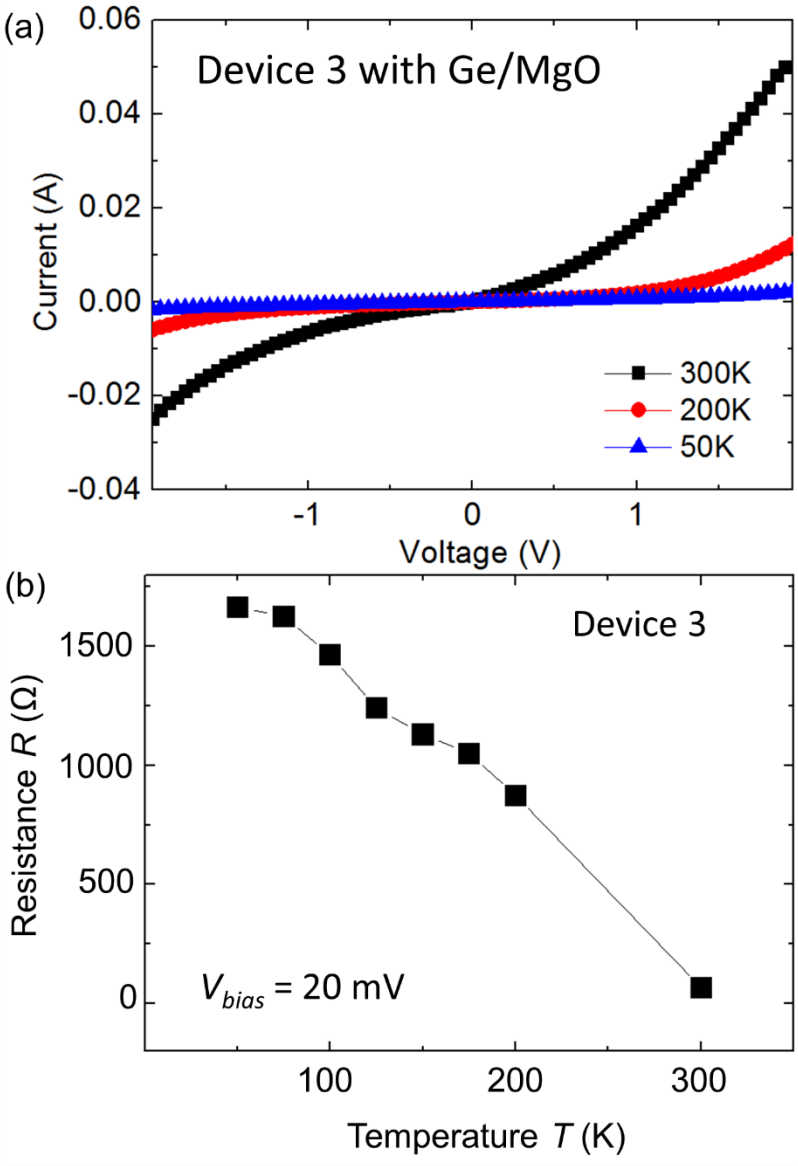

Figure 4.2: Conductance characteristics of the Si-based nanoscale spin-valve devices fabricated by EB evaporation (Device 3 with MgO/Ge double layer). a) *I-V* curves of Device 3 at different temperatures; b) The dependence of resistance on temperature of Device 3 measured at 20 mV. Reprinted from Appl. Phys. Lett. 109, 232402 (2016), with the permission of AIP Publishing.

4.3. Spin-dependent transport characteristics

In this section, the systematic investigation of the spin-dependent transport characteristics of the Si-based nanoscale 2 terminal spin-valve device fabricated by EB evaporation method in the aspect of bias voltage dependence, temperature dependence and magnetic-field direction dependence was conducted.

In conventional two-terminal spin-valve effect measurements, the spin-injecting and spin-detecting terminals are the same. Thus, they suffer from parasitic local magnetoresistance effects, such as the anisotropic magnetoresistance (AMR) effect of the FM electrodes and the tunneling anisotropic magnetoresistance (TAMR) effect at the FM / SC interfaces. To avoid such local effects, two well-known methods have been used to detect intrinsic spin transport in μm-long SC channels. The first is the non-local spin-valve effect in a four terminal configuration, where the spin-injecting terminals and the spin-detecting terminals are different. If the distance l between the spin-injecting and spin-detecting terminals is far enough compared with the depth d of the SC channel where the electric current flows, then the spin-detecting terminal voltage will not be affected by local effects and can detect a pure spin current [7]. However, if l is comparable or shorter than d, the non-local voltage is also affected by local effects as shown by careful experiments and device simulations [8]. As a result, the four-terminal configuration has no advantage over the two-terminal configuration in our case of nanoscale SC channels, because both methods suffer from local effects. The second is to observe spin precession when the spin-polarized electrons diffuse through the SC channel under an applied magnetic field (the Hanle effect) [9]. In this

method, however, the SC channels have to be long enough so that considerable spin precession can occur. Therefore, the Hanle effect cannot be used in our 20 nm-long Si channels, where the spin precession is negligible. Finally, it is noticed that any realistic nanoscale spin MOSFETs should operate only with source and drain electrodes, corresponding to the two terminal configuration. Taking the above into consideration, it could be concluded that the two-terminal spin-valve effect measurement is a realistic way to detect the spin transport in our devices, even though this method suffers from local effects. To distinguish the intrinsic spin-valve effect from the parasitic local effects in the two-terminal configuration, I systematically investigated the bias voltage dependence, temperature dependence, and magnetic-field direction dependence of MR in our devices.

4.3.1. Local spin-valve effect

Firstly, the local spin-valve effect is measured. Figure 4.3 shows the resistance-magnetic field (magnetoresistance – MR) characteristics of Device 1 – 2 – 3, respectively, measured at 50 K with a magnetic field applied along the Si channel (along the *x*-direction in Fig. 4.1(a)), and a bias voltage of 100 mV applied between the two FM electrodes. In Fig. 4.3, blue dots are data taken when the magnetic field was swept from +5 kG to -5 kG, while red dots are data taken when the magnetic field was swept from -5 kG to +5 kG. In Device 1 with Fe electrodes deposited directly on the Si channel, I have observed the small local signal ΔR of 0.6 Ω, corresponding to MR ratio of 0.03% as shown in fig. 4.3(a). In Device 2, by using 2 nm MgO conventional tunnel barrier between Fe electrodes and Si channel as previous studies, the local signal is increased to ΔR of 3 Ω – MR of 0.25% (Fig. 4.3(b)). In Device 3

with a 2 nm-thick MgO / 1 nm-thick Ge double layer as the new tunnel barrier, I achieved a strong local signal up to 12 Ω – corresponding to MR ratio of 0.8% in the device with MgO/Ge tunnel barrier as depicted in figure 4.3(c). This is also the highest local spin-valve signal in lateral Si-based spin-valve device at that time. It strongly demonstrates the advantage of my new double tunnel barrier compare to the conventional single MgO tunnel barrier. It could be understood that the spin coherence of tunneling electrons through the tunnel barrier has been improved by using the MgO/Ge as the tunnel barrier. Therefore, in the following sections, I focus on the spin-valve effect of the Device 3 with MgO/Ge tunnel barrier.

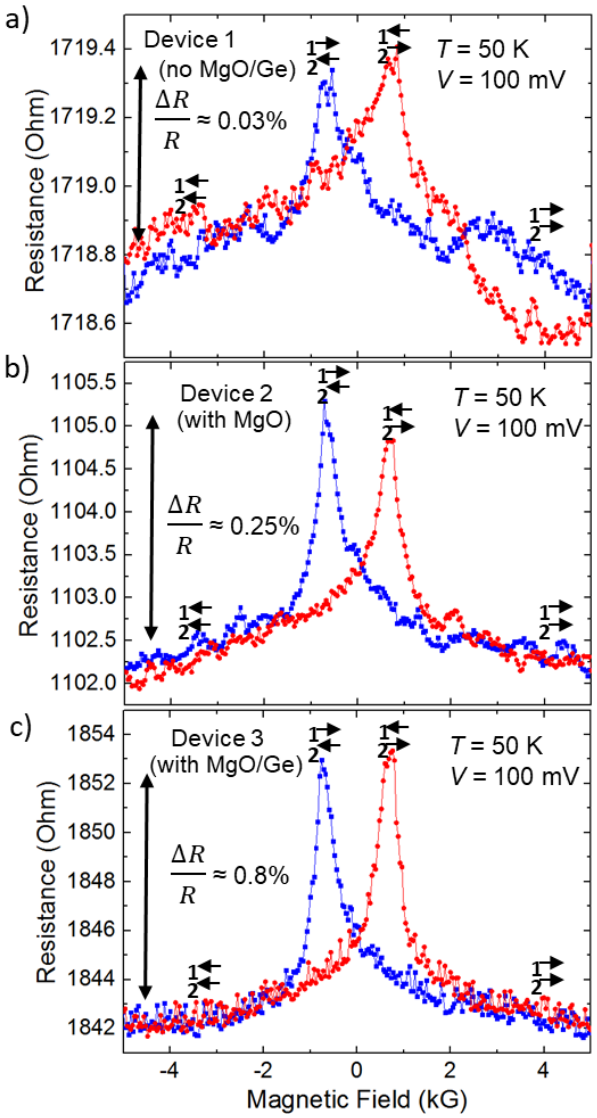

Figure 4.3: Resistance – magnetic field (magnetoresistance, MR) characteristics of (a) Device 1 with Fe electrodes deposited directly on the Si channel, (b) Device 2 with 2 nm MgO conventional tunnel barrier, and (c) Device 3 with a 2 nm-thick MgO / 1 nm-thick Ge double tunnel barrier, respectively, measured at 4.3 K with a bias voltage of 100 mV. Here, a magnetic field was applied along the Si channel transport direction (along the *x*-direction). Blue dots are data taken when the magnetic field was swept from +5 kG to -5 kG, while red dots are data taken when the magnetic field was swept from -5 kG to +5 kG.

4.3.2. Dependence of spin-valve signal on bias voltage and temperature

In order to verify that the observed MR originates from the spin-valve effect rather than the AMR effect of the Fe electrodes, the dependence of local spin-valve signal ΔR on bias voltages V was measured. Since the parasitic R_{Fe} of the metallic Fe electrodes does not depend on the bias voltage, the resistance change ΔR_{Fe} due to the AMR effect of Fe should not depend on V. In contrast, the spin-valve signal ΔR_{sv} due to the spin-valve effect varies with V due to the bias dependence of the spin-injection / detection efficiency [7]. Figures 4.4 shows the dependence of ΔR on bias voltage V of device 1 – 2 – 3, respectively. I found that ΔR decreases as V increases in all three devices, contrary to the AMR effect theory. It indicates that the AMR effect of the Fe electrodes is not the origin of the observed MR.

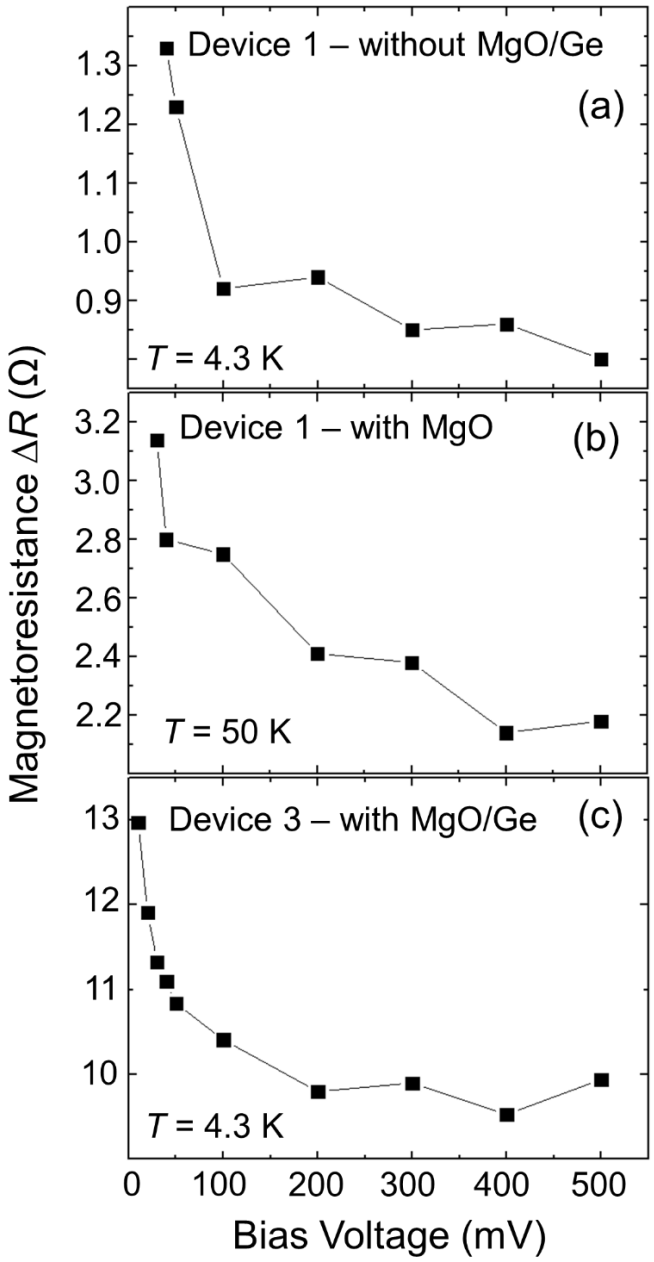

Figure 4.4: Bias voltage dependence of the magnetoresistance ΔR of Device 1 – 2 – 3, respectively. a) Relationship of ΔR – V_{bias} of Device 1 measured at 4.3 K. b) Relationship of ΔR – V_{bias} of Device 2 measured at 50 K. c) Relationship of ΔR – V_{bias} of Device 3 measured at 4.3 K. All devices show the decrease of ΔR as bias voltage increases. Reprinted from Appl. Phys. Lett. 109, 232402 (2016), with the permission of AIP Publishing.

It is also possible to distinguish the intrinsic spin-valve effect from the parasitic AMR effect by measuring the temperature dependence of ΔR. Since the parasitic R_{Fe} increases with increasing temperature, ΔR_{Fe} also increases with increasing temperature. In contrast, the resistance change ΔR_{sv} due to the spin-valve effect is expected to decrease with increasing temperature because the spin-life time of electrons in the Si channel becomes shorter as temperature increases [10]. Figures 4.5 shows the dependence of ΔR on temperature T of device 1 – 2 – 3, respectively. I have observed the ΔR decreases with increasing temperature in all devices, which is conflicted with the AMR effect theory, demonstrating that the observed MR is not related to the AMR effect.

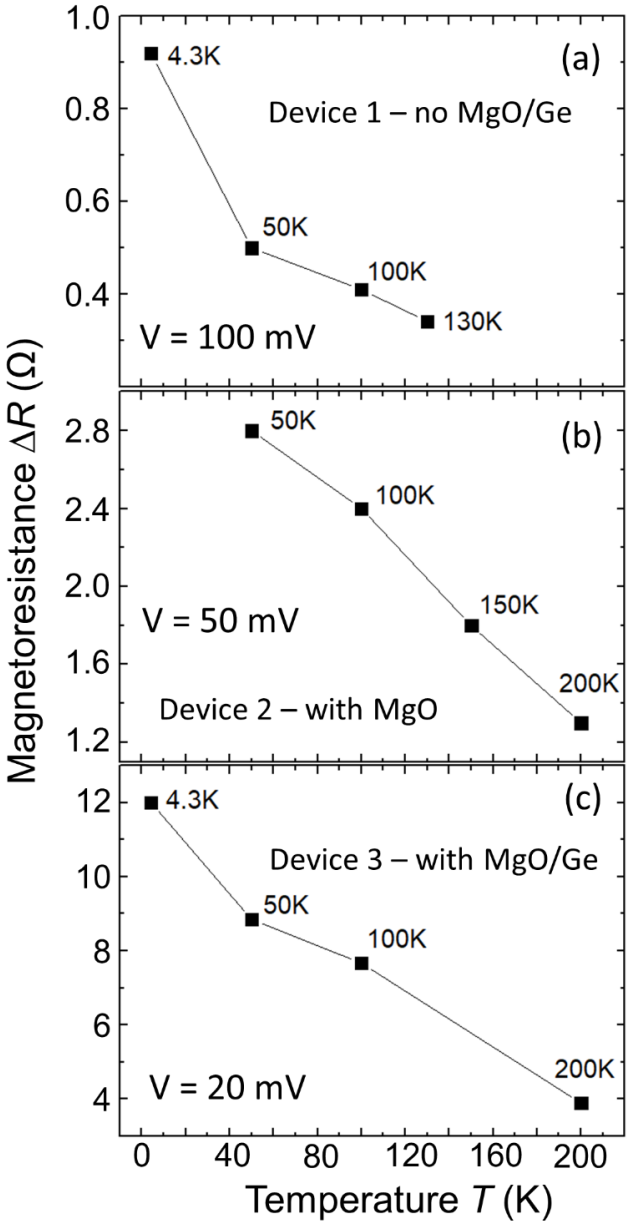

Figure 4.5: The temperature dependence of local spin-valve signal ΔR of (a) Device 1 measured at a bias voltage of 100 mV, (b) Device 2 measured at a bias voltage of 50 mV, and (c) Device 3 measured at a bias voltage of 100 mV. All devices show the ΔR decreases with increasing temperature. Reprinted from Appl. Phys. Lett. 109, 232402 (2016), with the permission of AIP Publishing.

Furthermore, since R_{Fe}/R is at most 4% at 4.3 K for Device 2 and the AMR ratio $\Delta R_{Fe}/R_{Fe}$ of Fe is in the order of 0.1%, the contribution of the AMR effect to the MR ratio $\Delta R_{Fe}/R$ should be at most $(\Delta R_{Fe}/R_{Fe})\times(R_{Fe}/R) \sim 10^{-5}$, which is too small to account for the observed MR ratio of 0.8%. From the above qualitative and quantitative considerations, it could be concluded that the contribution of the parasitic AMR effect is negligible.

4.3.3. Dependence of spin-valve signal on magnetic-field direction

There is another local effect that should be addressed; the TAMR effect at the Fe(interface)/MgO/Ge/Si. The TAMR effect originates from the dependence of the tunneling density of states (DOS) in the FM electrodes on the magnetization direction. The contribution of TAMR to the spin valve signals was investigated by measuring the dependence of the magnetoresistance on the magnetic-field direction ϕ with respect to the *x*-direction, as shown in Fig. 4.6(a). Figures 4.6(b)-(e) show the MR curves of Device 3 measured at 50 K when the magnetic field was applied along $\phi = 0^o$, 30^o, 60^o, and 90^o, respectively. In these measurement, if the observed MR originated from the TAMR effect, the MR signal would be reversed when ϕ changes from 0^o to 90^o; that is, there would be two drops in the MR curve at $\phi = 0^o$, but two jumps at $\phi = 90^o$ [11,12,13]. However, the same shape and polarity of the MR curves for all ϕ have been observed. Furthermore, I observed clear minor loops (green curves) in all cases. (Note the difference of about 200 G of the coercive force between the major and minor loops.) These results indicate that the observed resistance jumps depend only on the relative angle between the magnetization directions of the two FM electrodes, consistent with the behavior of the spin-valve effect. It could be concluded that, while there might be TAMR in my devices,

its contribution should be smaller than the experimental noise level (<0.1%), and cannot be observed in our experiments. The absence of the TAMR effect in my devices can be explained by the fact that the Fe electrodes are polycrystalline, thus the change of tunneling DOS with the direction of magnetization in different crystal grains is canceled and becomes zero. It is also noted that the observed MR effect remains observable up to 200 K, which is in good agreement with previous reports on the temperature dependence of the spin-life time of electrons in Si [10,14]. All of these results strongly suggest that the observed MR is governed by spin transport through the nanoscale Si channel in our devices.

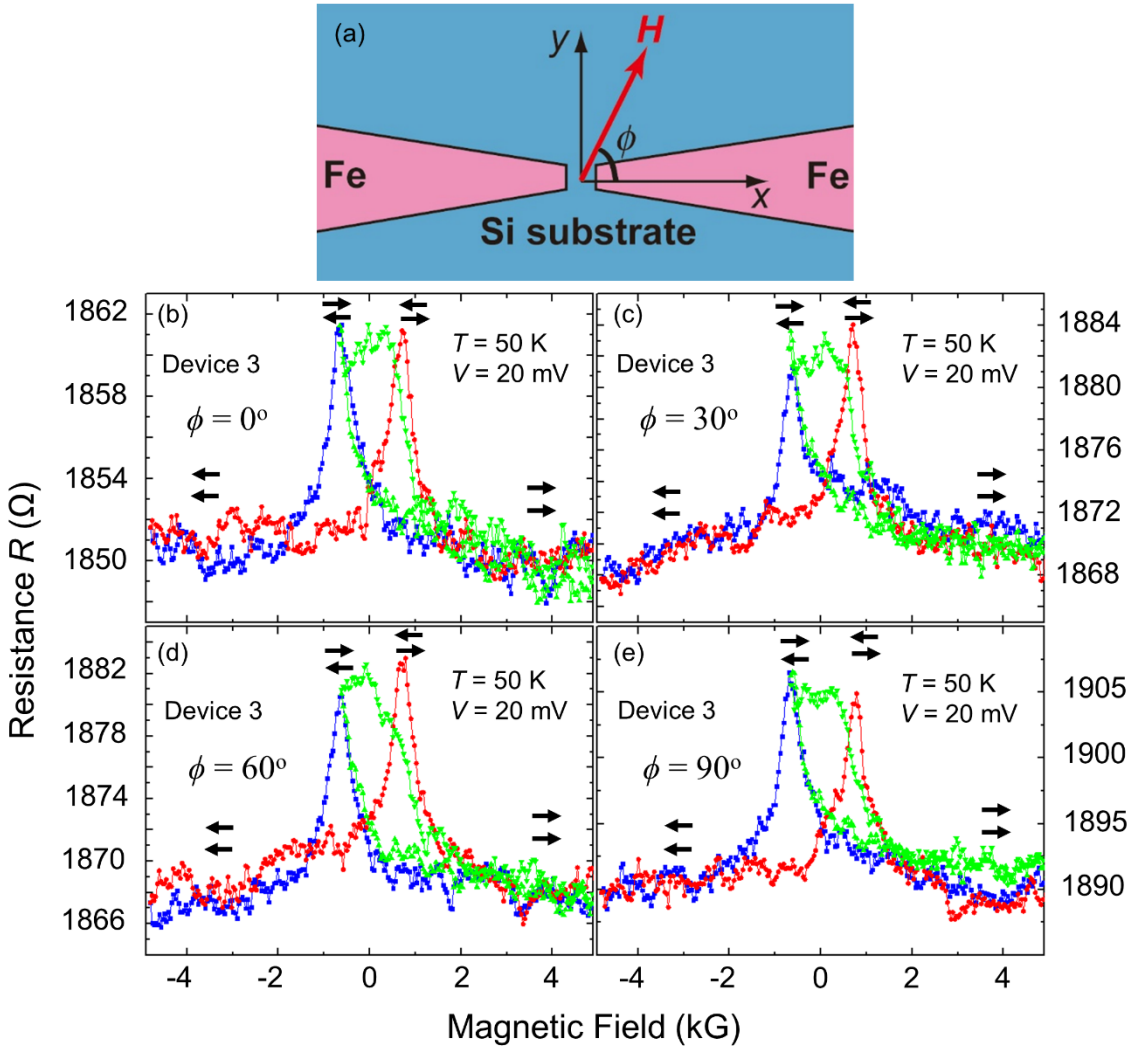

Figure 4.6: (a) Experimental setup for measurement of magnetic-field direction dependence of the magnetoresistance. Here, the magnetic field is applied in the *x*-*y* plane along the angle ϕ with respect to the Si channel (the *x*-direction). (b)-(e) Magnetoresistance of Device 3 measured at 50 K with a bias voltage of 20 mV, when ϕ = 0°, 30°, 60°, and 90°, respectively. Minor loop magnetoresistance curves (green) are also shown. Reprinted from Appl. Phys. Lett. 109, 232402 (2016), with the permission of AIP Publishing.

4.4. Spin-dependent output voltage

Finally, it is the investigation of the spin-dependent output performance of my devices. In realistic applications, a spin-dependent output $\Delta V = \Delta R \times I$ of the order of 100 mV is required for correct read-out. However, previous studies on spin injection to Si reported a read-out voltage of only a few μV in 4 terminal measurements, and about 1 mV in 3 terminal measurements. In the voltage-biased spin-valve devices of mine, the corresponding spin-dependent output is calculated by $\Delta V = \Delta R \times \left(\frac{V}{R}\right) = \left(\frac{\Delta R}{R}\right) \times V$. Figure 4.7 shows the plot of the spin-dependent output $\Delta V = (\Delta R/R) \times V$ of Device 3 as a function of the bias voltage V at 50 K. In this device, I achieved ΔV = 13 mV at V = 1.7 V. Although still far behind the target value of ~ 100 mV, this value is among the highest values reported so far at that time. According to the first principles calculation taking into account electron-phonon and electron-impurity scattering, the mean free path of electrons in n-type silicon with $n = 10^{18}$ cm^{-3} is between 20 ~ 40 nm [15]. In reality, there are many other scattering mechanisms, such as interface scattering, that can make the real mean free path shorter than the calculated value. The spin transport in our Si channel may be quasi-ballistic rather than fully ballistic. Nevertheless, it is able to observe the clear spin-valve effect and large spin-signal up to 13 mV.

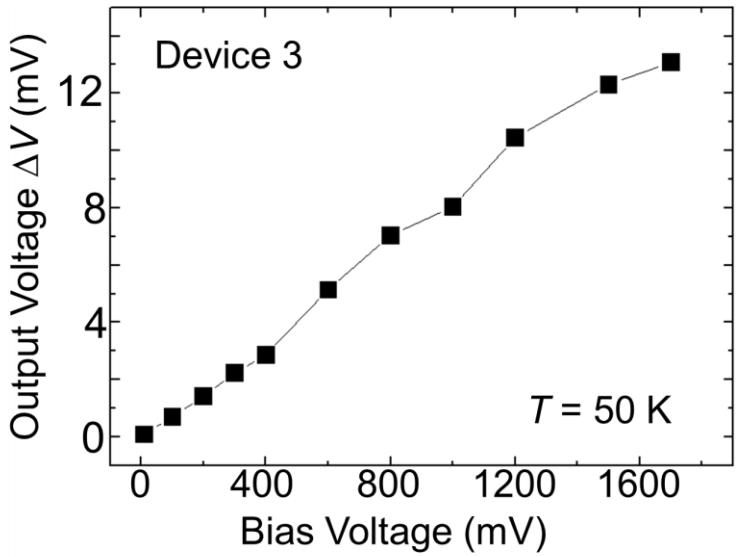

Figure 4.7: Bias voltage dependence of the spin-dependent output voltage ($\Delta R/R)V$ of device 3 at 50 K. The highest output voltage ΔV of 13 mV was achieved at the bias voltage of 1.7 V. Reprinted from Appl. Phys. Lett. 109, 232402 (2016), with the permission of AIP Publishing.

4.5. Summary

In conclusion, this chapter presents the investigation of the spin transport in nanoscale Si spin-valve devices with the FM and tunnel barrier prepared by the EB evaporation method. Systematic investigations of the bias voltage dependence, temperature dependence, and magnetic-field direction dependence of the magnetoresistance indicate that the observed spin valve effect is governed by the spin transport through the nanoscale Si channel. The highest magnetoresistance of 12 Ω corresponding to MR ratio of 0.8 % and the highest spin-dependent output voltage of 13 mV were achieved for a device with the MgO/Ge tunnel layer

at a bias voltage of 1.7 V at 50 K, which are among the highest values reported so far. The spin-valve effect decreases with increasing temperature but remains observable up to 200 K. It is expected that if the Si channel can be made shorter so that ballistic transport can occur, larger spin-valve effect can be realized. The results in this chapter have been published on APL **109**, 232402 (2016).

References

1. Jiang, X. *et al.* Highly Spin-Polarized Room-Temperature Tunnel Injector for Semiconductor Spintronics using MgO(100). *Phys. Rev. Lett.* **94,** 056601 (2005).

2. Martínez Boubeta, C. *et al.* Epitaxial Fe/MgO heterostructures on GaAs(001). *J. Cryst. Growth* **226,** 223–230 (2001).

3. Miao, G. X. *et al.* Disturbance of tunneling coherence by oxygen vacancy in epitaxial Fe/MgO/Fe magnetic tunnel junctions. *Phys. Rev. Lett.* **100,** 1–4 (2008).

4. Jeon, K.-R., Park, C.-Y. & Shin, S.-C. Epitaxial Growth of MgO and CoFe/MgO on Ge(001) Substrates by Molecular Beam Epitaxy. *Cryst. Growth Des.* **10,** 1346–1350 (2010).

5. Han, W. *et al.* Growth of single-crystalline, atomically smooth MgO films on Ge(001) by molecular beam epitaxy. *J. Cryst. Growth* **312,** 44–47 (2009).

6. Schöllhorn, C., Oehme, M., Bauer, M. & Kasper, E. Coalescence of germanium islands on silicon. *Thin Solid Films* **336,** 109–111 (1998).

7. Lou, X. *et al.* Electrical detection of spin transport in lateral ferromagnet–semiconductor devices. *Nat. Phys.* **3,** 197–202 (2007).

8. Nakane, R., Sato, S., Kokutani, S. & Tanaka, M. Appearance of anisotropic magnetoresistance and electric potential distribution in Si-based multiterminal devices with Fe electrodes. *IEEE Magn. Lett.* **3,** (2012).

9. Johnson, M. & Silsbee, R. H. Interfacial charge-spin coupling: Injection and detection of spin magnetization in metals. *Phys. Rev. Lett.* **55,** 1790–1793 (1985).

10. Huang, B., Monsma, D. J. & Appelbaum, I. Coherent Spin Transport through a 350 Micron Thick Silicon Wafer. *Phys. Rev. Lett.* **99,** 177209 (2007).

11. Gould, C. *et al.* Tunneling anisotropic magnetoresistance: A spin-valve-like tunnel magnetoresistance using a single magnetic layer. *Phys. Rev. Lett.* **93,** 1–4 (2004).

12. Rüster, C. *et al.* Very Large Tunneling Anisotropic Magnetoresistance of a (Ga,Mn)As/GaAs/(Ga,Mn)As Stack. *Phys. Rev. Lett.* **94,** 027203 (2005).

13. Moser, J. *et al.* Tunneling anisotropic magnetoresistance and spin-orbit coupling in Fe/GaAs/Au tunnel junctions. *Phys. Rev. Lett.* **99,** 1–4 (2007).

14. Sasaki, T. *et al.* Electrical spin injection into silicon using MgO tunnel barrier. *Appl. Phys. Express* **2,** (2009).

15. Qiu, B. *et al.* First-principles simulation of electron mean-free-path spectra and thermoelectric properties in silicon. *EPL (Europhysics Lett.* **109,** 57006 (2015).

CHAPTER 5

INVESTIGATION of SPIN-VALVE DEVICES FABRICATED by MOLECULAR BEAM EPIXATY

In this chapter, the investigation of the spin-valve effect in nano-scale silicon (Si)-based spin-valve devices using a Fe/MgO/Ge spin injector / detector grown on Si by molecular beam epitaxy was presented. For a device with a 20 nm Si channel, a clear magnetoresistance (MR) up to 3 % at low temperature was achieved when a magnetic field was applied in the film plane along the Si channel transport direction. A large spin-dependent output voltage of 20 mV was observed at a bias voltage of 0.9 V at 15 K, which is among the highest values in lateral spin-valve devices reported so far. Furthermore, I observed that the sign of the spin-valve effect is reversed at low temperatures, suggesting the possibility of a spin-blockade effect of defect states in the MgO/Ge tunneling barrier. The results in this chapter have been published in JAP 122, 223904 (2017) and has been selected as the AIP Science Highlight paper and JAP Featured paper.

5.1. Spin-valve device structures

All of the spin-valve devices were fabricated on n-type Si (100) substrates with an electron density $n = 1\times10^{18}$ cm^{-3}. The Si substrates were cleaned by H_2SO_4/H_2O_2 solution, followed by diluted hydrofluoric acid solution to remove the native oxide layer, and then rinsed in de-ionized water. After that, the substrates were introduced into a molecular-beam-epitaxy (MBE) chamber with a base pressure of 1×10^{-8} Pa for deposition of a 1 nm-thick Ge spacer, a 2 nm-thick MgO tunnel barrier, a 10 nm Fe layer, and a 1 nm-thick MgO capping layer. Knudsen cells were used for thermal evaporation of Ge and Fe, while a low-power electron-beam evaporator was used to deposit MgO with a slow rate of 0.03 Å/s. In-situ reflection high energy electron diffraction confirmed that MgO grown on the Ge buffer layer became crystalline when the MgO thickness exceeded 1 nm.

After depositing the MgO/Ge tunnel barrier and the Fe electrodes by MBE, e-beam lithography and Ar ion-milling techniques were used to fabricate nanoscale spin-valve devices. Details of the fabrication process are described in chapter 3. Figure 5.1(a) illustrates the device structure examined in this work. Figure 5.1(b) shows a scanning electron microscopy image of a spin-valve device. A Si channel with a length of 20 nm was formed between the Fe electrodes. The coercive forces of the Fe electrodes are determined by the domain wall pinning potentials at grain boundaries or defects of the Fe electrodes near the nanoscale Si channel, which are not exactly the same but slightly different between the left and right electrodes. Indeed, it is found that the coercive force of the left and the right electrode differs by 120 G. This small difference establishes a narrow range of magnetic field

where the anti-parallel magnetization configuration is realized, thus the spin-valve effect can be observed.

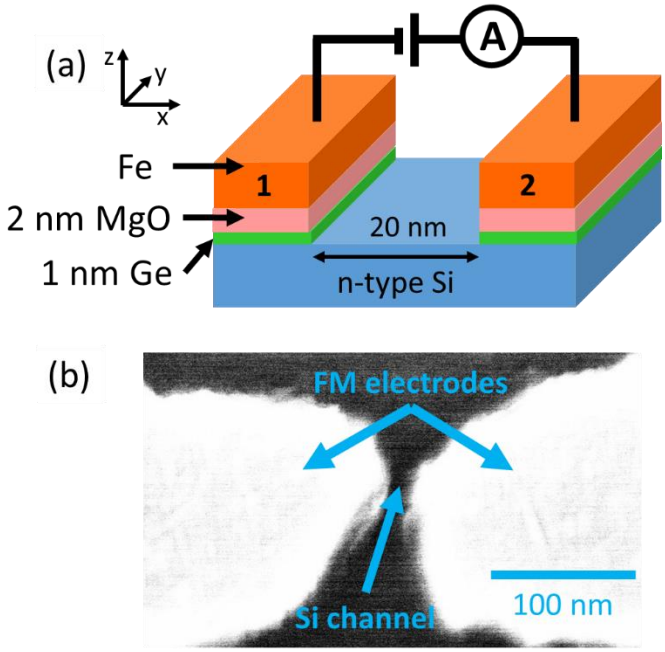

Figure 5.1**:** (a) Schematic spin-valve device structure with a Fe/MgO/Ge spin injector / detector and a 20 nm-long Si channel. (b) Scanning electron microscopy image (top view) of a device. A silicon channel with a length of 20 nm was formed between the Fe electrodes. Reprinted from J. Appl. Phys. 122, 223904 (2017), with the permission of AIP Publishing.

5.2 Structural characterization

In this section, the crystal quality of Ge, MgO, and Fe structure in my spin-valve devices was investigated.

Chapter 5

In order to investigate the crystal quality of the MgO, Fe, and Ge layers in my devices, several reference samples were prepared; a 40 nm-thick Ge layer, MgO(40 nm)/Ge(1nm) and Fe(40 nm)/MgO(2 nm)/Ge(1 nm) multilayers [denoted as Ge, MgO, and Fe samples, respectively] on Si substrates prepared both by EB evaporation and by MBE. Then X-ray diffraction (XRD) measurements were conducted on these reference samples. Figure 5.2 shows the XRD spectra of the reference samples deposited by EB evaporation and MBE, respectively. In Fig. 5.2(a) of the EB evaporation samples, the XRD spectrum of the Ge sample shows no peak. Meanwhile, the XRD spectrum of the MgO sample shows a weak MgO(200) peak, and that of the Fe sample shows both Fe(110) and Fe(211) peaks. These results indicate that the Ge layer was amorphous, while the crystal quality of the MgO layer was not good, and the Fe layer was poly-crystalline with dominant (110) and (211) orientations. On the contrary, all of the MBE-grown samples show clear peaks corresponding to Ge(400), MgO(200) and (400), and Fe(110) and (220) as shown in Fig. 5.2(b), indicating much improved crystal quality. Based on these results, it is expected that the crystal quality of spin injectors/detectors grown by MBE is much better than those deposited by EB evaporation.

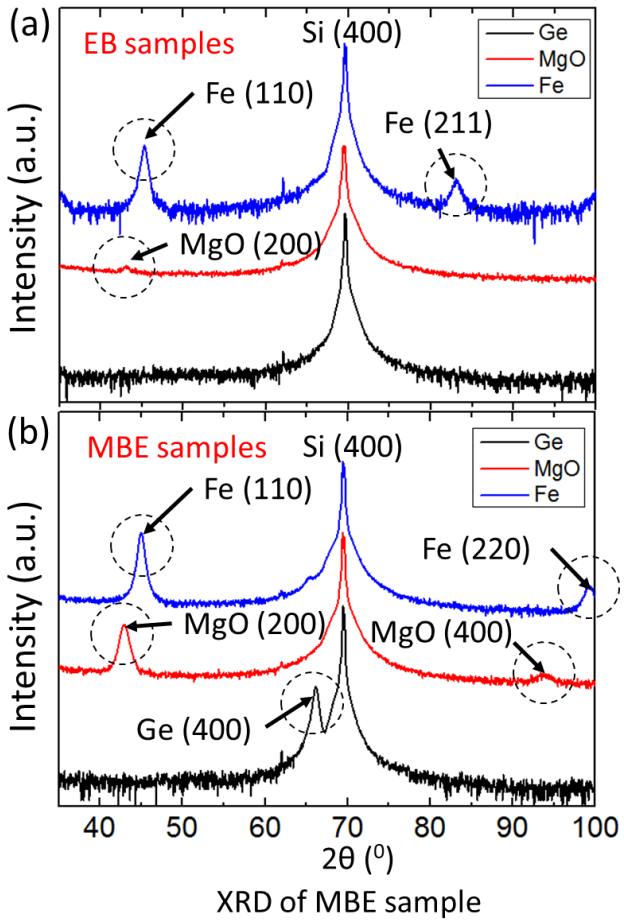

Figure 5.2: (a) – (b) X-ray diffraction (XRD) spectra of reference samples fabricated by EB evaporation and MBE, respectively.

5.3. Conductance characteristics

This section describes the investigation of the conductance characteristics of the Si-based nanoscale 2 terminal spin-valve devices fabricated by the MBE method.

Figure 5.3(a) shows representative current – voltage characteristics (*I-V* curves) of a spin-valve device with a 2 nm MgO / 1 nm Ge tunnel barrier at various temperatures, which

clearly show non-linear dependence of the current on the bias voltage, suggesting that tunneling transport occurs at the Fe/MgO/Ge/Si junctions. Furthermore, a strong dependence of *I*-*V* curves on temperature also was observed. Figure 5.3(b) shows the device resistance as a function of temperature, measured at V = 150 mV. I have observed that the resistance rapidly increases with temperature, from the order of ~ 10^1 Ω at 300 K to ~ 10^8 Ω at 4.3 K. The origin of this behavior will be discussed in the later section. From this data, it is able to estimate the contribution of the parasitic anisotropic magnetoresistance (AMR) of the Fe electrodes to the total spin-valve effect as follows. The total device resistance R can be decomposed into two components: $R = R_{Fe} + R_{sv}$, where R_{Fe} is the parasitic resistance of the Fe electrodes and R_{sv} is the intrinsic resistance of the Fe(interface)/(MgO/Ge) /Si/(Ge/MgO)/Fe(interface) spin-valve structure. Since the parasitic $R_{Fe}(T)$ decreases as temperature decreases, $R_{Fe}(T) \leq R_{Fe}(300K) < R(300K) = 30\ \Omega$. The AMR effect $|\Delta R_{Fe}/R_{Fe}|$ of Fe is in the order of 0.1%, thus $|\Delta R_{Fe}|$ is in the order of 0.3 Ω. From this consideration, it is possible to estimate the contribution of the parasitic AMR effect of $|\Delta R_{Fe}/R(T)|$ at various temperatures. For example, $|\Delta R_{Fe}/R(T)|$ at 15 K should be in the order of 10^{-8}. Therefore, it could be concluded that the contribution of the parasitic AMR effect of the Fe electrodes is negligible at low temperatures.

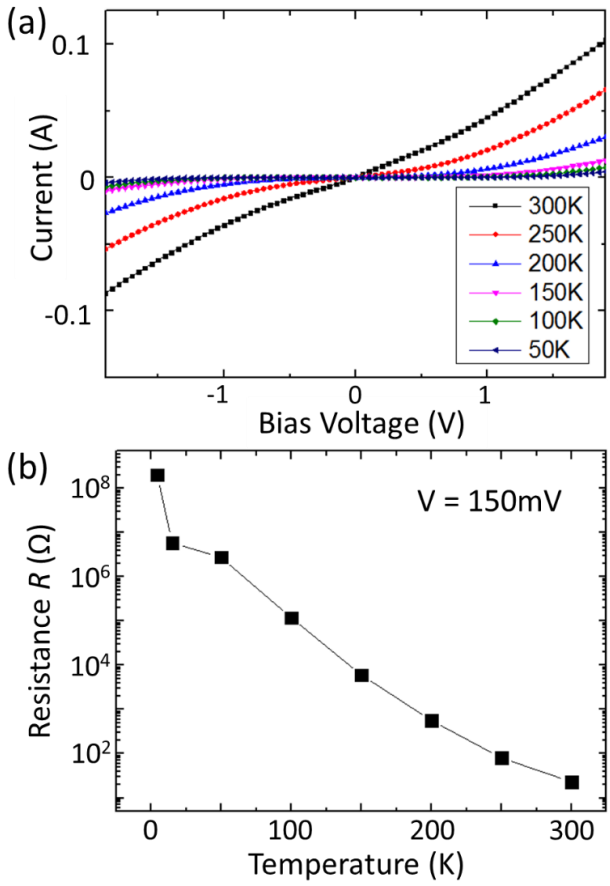

Figure 5.3: (a) Current–voltage characteristics (*I*-*V* curves) of a device with a 2 nm MgO / 1 nm Ge tunnel barrier grown by MBE at various temperatures. (b) Temperature dependence of the resistance measured at 150 mV. Reprinted from J. Appl. Phys. 122, 223904 (2017), with the permission of AIP Publishing.

5.4. Spin-dependent transport characteristics

In this section, the systematic investigation of the spin-dependent transport characteristics of the Si-based nanoscale 2 terminal spin-valve devices fabricated by the MBE method at various bias voltages, temperatures and magnetic-field directions was conducted.

5.4.1. Local spin-valve effect

Traditionally, the spin transport in Si has been studied by using the Hanle effect. In this method, however, the semiconductor channels have to be long enough so that considerable spin precession can occur. In the 20 nm-long Si channels, the spin precession is negligible. Therefore, the Hanle effect cannot be used. In this work, the local spin-valve effect was used to characterize the spin transport. Although this method suffers from parasitic local effects, such as the AMR effect of the FM electrodes and the tunneling anisotropic magnetoresistance (TAMR) effect at the FM/SC interfaces, it was shown in Chapter 4 that it is possible to distinguish the intrinsic spin-valve effect from parasitic local effects by systematic measurements of the bias voltage dependence, temperature dependence, and magnetic-field direction dependence of magnetoresistance (MR) [1]. Figure 5.4(a) shows the MR characteristic of our spin-valve device measured at 15 K with a bias voltage of 300 mV and a magnetic field applied along the Si channel (*x*-direction in Fig. 5.1(a)). In Fig. 5.4(a), blue dots are the resistance data taken when the magnetic field was swept from +3 kG to -3 kG, while red dots are taken when the magnetic field was swept from -3 kG to +3 kG. The inset shows the minor loop MR, when the magnetic field was swept from 3 kG to -0.08 kG, then back to 3 kG. An enormous drop of resistance $|\Delta R| \sim 57$ kΩ, corresponding to $|\Delta R/R| = 3\%$ was observed. This $|\Delta R|$ and $|\Delta R/R|$ values are five orders of magnitude larger than that of the parasitic AMR effect of the Fe electrodes at 15 K ($|\Delta R_{Fe}| \sim 0.3$ Ω and $|\Delta R_{Fe}/R|=10^{-8}$). Furthermore, I measured $|\Delta R|$ at various bias voltage V, and found that $|\Delta R|$ also strongly depends on V, as shown in Fig. 5.4(b). This cannot be explained by the AMR effect, because

$|\Delta R_{Fe}|$ does not depend on the bias voltage. From the above quantitative and qualitative considerations, it is concluded that the contribution of the parasitic AMR effect is negligible. The $|\Delta R|$-V relationship closely follows R-V as shown in Fig. 5.4(b), indicating that the observed MR effect originates from the spin-dependent tunneling process of electrons between the Fe electrodes and the Si channel through the MgO/Ge barrier.

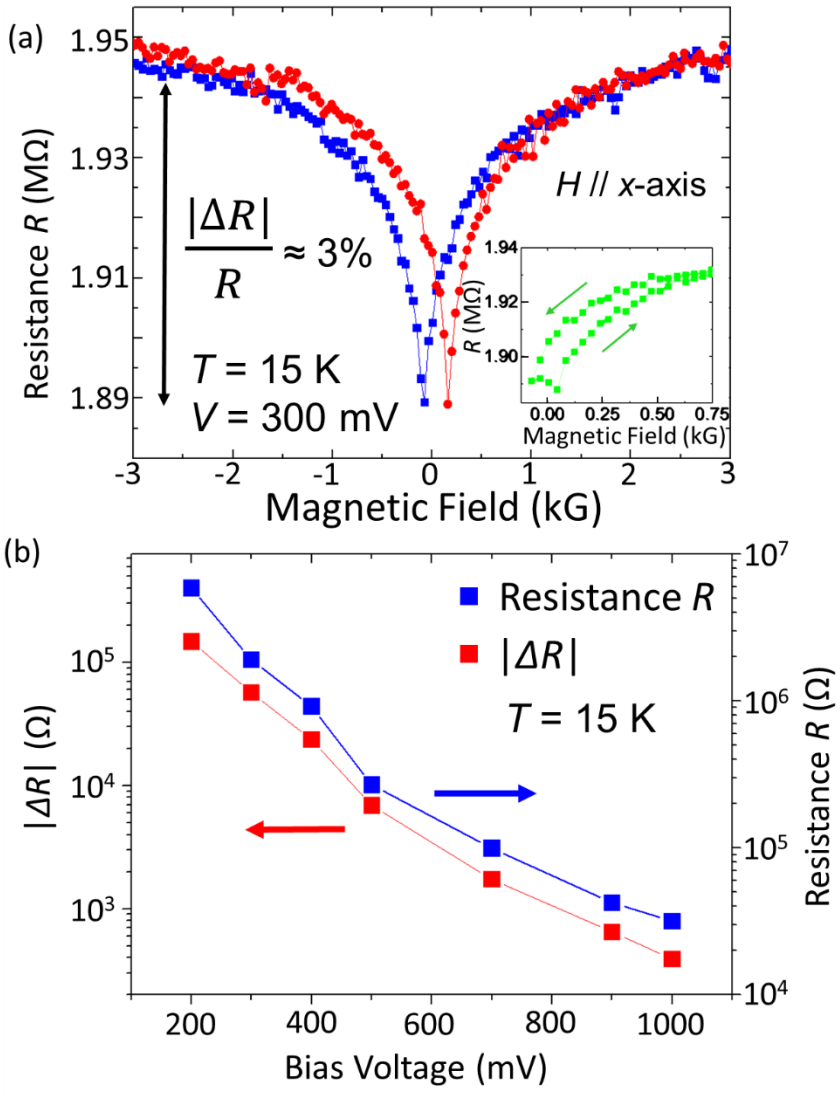

Figure 5.4: (a) Magnetoresistance characteristics of the device measured at 15 K with a bias voltage of 300 mV. Blue dots are the resistance data taken when the magnetic field was swept from +3 kG to -3 kG, while red dots are taken when the magnetic field was swept from -3 kG to +3 kG. Inset shows the minor loop of the device. (b) Magnetoresistance $|\Delta R|$ and device resistance R as a function of bias voltage at 15 K. Reprinted from J. Appl. Phys. 122, 223904 (2017), with the permission of AIP Publishing.

5.4.2. Dependence of the spin-valve signal on the magnetic-field direction

In order to distinguish the intrinsic spin-valve effect from the TAMR effect at the Fe(interface)/MgO/Ge/Si interface, the dependence of the MR curve on the magnetic-field direction ϕ with respect to the *x*-direction was measured, as shown in Fig. 5.5(a). Here, the TAMR effect originates from the dependence of the tunneling density of states (DOS) in the FM electrodes on the magnetization direction. Figures 5.5(b)-(f) show the MR curves measured at 100 K when the magnetic field was applied along ϕ = 0°, 30°, 45°, 60°, and 90°, respectively. In these measurement, if the spin-valve signals are caused by the TAMR effect, the MR curve would be reversed or changed in shape when ϕ changes from 0° to 90° [2,3,4]. However, the same shape and polarity of the MR curves for all the ϕ values were observed. These results indicate that the observed MR depends only on the relative angle between the magnetic moments of the two Fe electrodes, thus it is caused by the spin-valve effect. Note that observed MR is negative at 100 K, as shown in Figs. 5.5(b)-(f), and the sign of MR will be discussed in the next sub section.

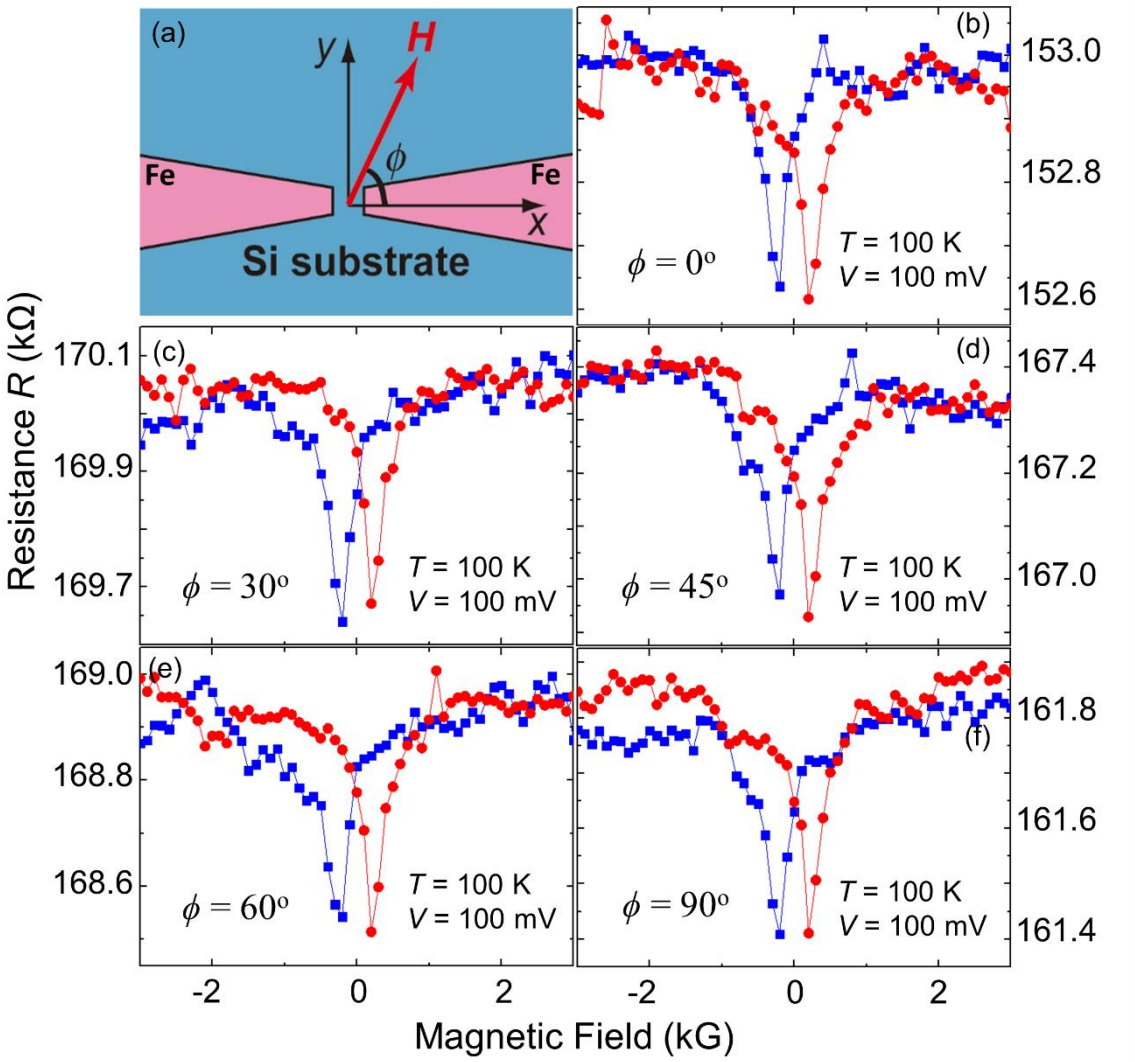

Figure 5.5: (a) Measurement configuration of magnetic-field direction dependence of the magnetoresistance. Here, the magnetic field is applied in the *x*-*y* plane along the angle ϕ with respect to the Si channel (the *x*-direction). (b)-(f) Magnetoresistance curves measured at 100 K with a bias voltage of 100 mV, when ϕ = 0°, 30°, 45°, 60°, and 90°, respectively. Reprinted from J. Appl. Phys. 122, 223904 (2017), with the permission of AIP Publishing.

5.4.3. Dependence of the spin-valve signal on temperature – The inverse spin-valve effect

Figure 5.6(a) shows the temperature dependence of the spin-valve MR ratio ($\Delta R/R$). Here, the negative (positive) spin-valve MR ratio corresponds to the resistance drop (jump) in the MR curves. It was found that the spin-valve MR ratio is negative at temperatures lower than 200 K, and becomes positive at temperatures higher than 200 K. A representative positive MR curve at 250 K is shown in the inset of Fig. 4(a). Such behavior is unusual and has not been observed before in Si-based spin-valve devices.

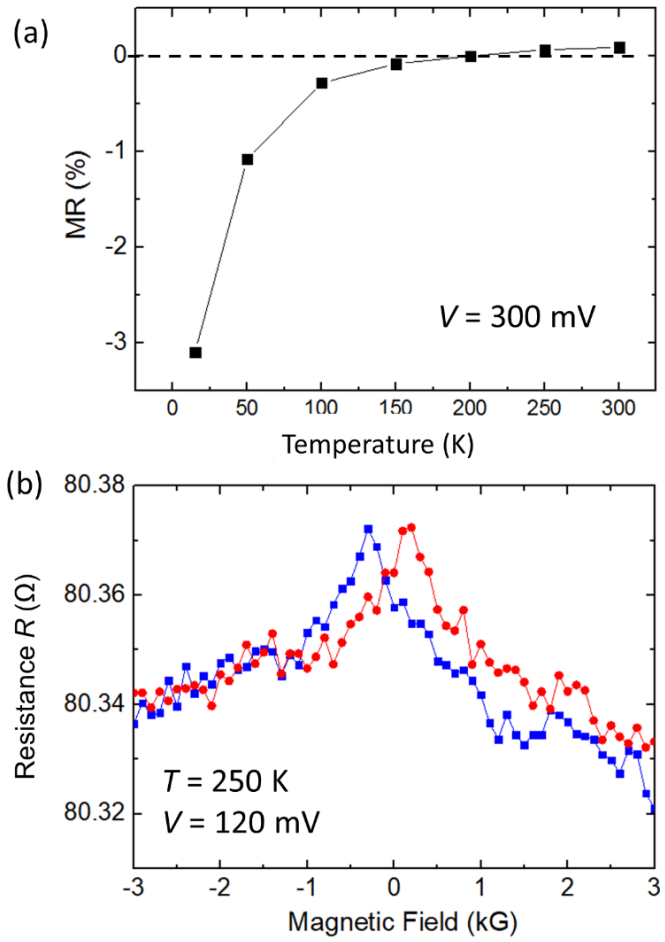

Figure 5.6: (a) Temperature dependence of the spin-valve MR ratio (defined as $\Delta R/R$) measured at a bias voltage of 300 mV. The spin-valve MR ratio is positive at temperatures higher than 200 K, but become negative at temperatures lower than 200 K, (b) the local spin-valve signal of device measured at 250 K with a bias voltage of 120 mV. Reprinted from J. Appl. Phys. 122, 223904 (2017), with the permission of AIP Publishing.

In order to understand the origin of such "inverse" spin-valve effect, I focus on the electron tunneling process between the Fe electrodes and Si channel. It is firstly reminded that the device resistance increases rapidly as temperature decreases, from the order of 10^1 Ω

at 300 K to 10^8 Ω at 4.3 K, as shown in Fig. 5.2(b). This fact immediately indicates that direct tunneling of electrons between the Fe electrodes and Si channel through the MgO tunnel barrier is not dominant, because the resistance due to direct tunneling does not or very weakly depends on temperature. Instead, the strong temperature dependence of the device resistance *R* suggests that the electron transport through the barrier is governed by thermally activated tunneling through some defect states in the barrier, whose energy level is much smaller than the intrinsic barrier height between Fe an MgO. Such defect states in MgO barriers are well known. For example, in Fe/MgO/Fe magnetic tunnel junctions, oxygen vacancy defects in the MgO barrier form gap states at about 1.2 eV below the conduction band bottom of MgO, which reduces the MgO barrier height to just 0.39 eV [5]. Therefore, it is reasonable to assume such defect-induced gap states inside the MgO barrier of our spin-valve devices. Figures 5.7 shows my model to explain the "inverse" spin-valve effect. In this model, the two Fe electrodes work as a spin injector and detector. Spin-polarized electrons tunnel from the Fe spin injector to the Si channel through defects-induced gap states inside the MgO barrier. The electrons then transport in the Si channel without or with little scattering (ballistic or quasi ballistic transport), and reach the opposite MgO barrier with higher kinetic energy. Finally, the electrons tunnel through gap states inside another MgO barrier to the Fe spin detector. In this picture, the relevant gap states are those with energy levels higher than the Fermi level of the Fe spin injector. At high temperatures, electrons in the Fe spin injector with high enough thermal energy can tunnel to the gap states (thermally activated tunneling), and the device resistance is low (~ 10^1 Ω at 300 K). At low temperatures, however, the number of thermal electrons drastically decreases, resulting in much higher resistance (~ 10^8

Ω at 4.3 K). Note that at low temperatures, only a limited number of the gap states whose energy levels are very close to the Fermi level of the Fe spin injector can allow such tunneling. If these gap states are filled with majority spins whose residence time is long enough at low temperatures, only minority spins from the spin injector can go through. Such a "spin-blockade" phenomenon, originated from the Pauli exclusion principle, is well known and has been observed in many quantum dot systems as well as defect states in semiconductors [6,7]. In contrast, the electrons that arrive at the opposite MgO barrier can have higher kinetic energy, thus they can tunnel through many available gap states whose energy levels are higher than the Fermi level of the Fe spin detector. Thus, spin-blockade strongly occurs only at the spin injector side, and not at the spin detector side. In such a situation, the device resistance becomes high (low) at parallel (antiparallel) magnetization configuration, as shown in Figs. 5.7(a) and 5.7(b). This explains the observed inverse spin-valve effect at low temperatures. As temperature increases, there are more available gap states with higher energy levels for thermally activated tunneling from the spin injector. Furthermore, the residence time of majority spins at the defect states can be much shorter at high temperatures. As a result, the spin-blockade is not effective anymore, thus the normal spin-valve effect is dominant at higher temperature as shown in Fig. 5.7(c) and 5.7(d). My model is also consistent with the impurity assisted tunneling model proposed for explanation of the three-terminal Hanle effect observed in some FM/SC systems [8].

In fact, the negative MR has been reported in Co nanoparticle systems by Yakushiji *et al.* [9]. In their experiment, Yakushiji has investigated the magnetotransport properties of the Co nanoparticles with the particle size ~ 5 nm sandwiched between a Co and Al electrode,

and observed an oscillation of MR behavior in the range from -10 % to +15 % as shown in Fig. 5.8(a). Fig. 5.8(b) shows a negative MR signal observed at the bias voltage of 0.05 V. Here, the MR ratio is defined as $= \frac{R_{AP}-R_P}{R_{AP}}$, where R_P (R_{AP}) is the resistance of the system in parallel (anti-parallel) alignment. This negative MR arises due to the long spin-relaxation time τ_s of electrons in the Co nanoparticle (~ 150 ns). In the nanoscale confinement particles, the spin-relaxation is predicted to be strongly suppressed because of the quantum-size effect. If this spin-laxation time τ_s is smaller than tunneling time τ of electrons for jumping in/out the nanoparticles ($\tau_s << \tau$), there is no spin accumulation in the nanoparticles. In that case, the spin transport is governed simply by the Jullier model of tunneling magnetoresistance (TMR) effect for which there is no negative MR. On the contrary, in case of $\tau_s >> \tau$, there is a strong spin accumulation inside the nanoparticles, leading to the difference between the Fermi levels of majority and minority spin of the nanoparticles. This spin accumulation causes the oscillation and the negative MR. This phenomenon could be understood as in the model shown in Fig. 5.8(c)-(d). At a certain bias voltage close to a Coulomb staircase (discrete energy level of Coulomb blockade), the majority spin is blocked due to the higher discrete charging level inside the nanoparticle, thus only the minority can pass through as shown in Fig.5.8(c). Thus, the current is small in the parallel state. On the other hand, in the anti-parallel state, the majority spin is not blocked in the nanoparticle as shown in Fig. 5.8(d). In such a situation, the device resistance becomes high (low) at parallel (antiparallel) magnetization configuration. This is the reason for the negative MR in the nanoparticle system. In my devices, the similar negative MR, which is originated from the spin blockade of majority spins in the parallel state, has been observed. There is clear analogy between my

inverse MR and that by Yakushuji *et al.*, even though the physics is different. The inverse MR in my devices is due to spin-blockage at defect states in the MgO tunnel barrier, which originates from the Pauli exclusion principle. Meanwhile, the negative MR in Yakushuji's devices is due to Coulomb blockade and spin accumulation.

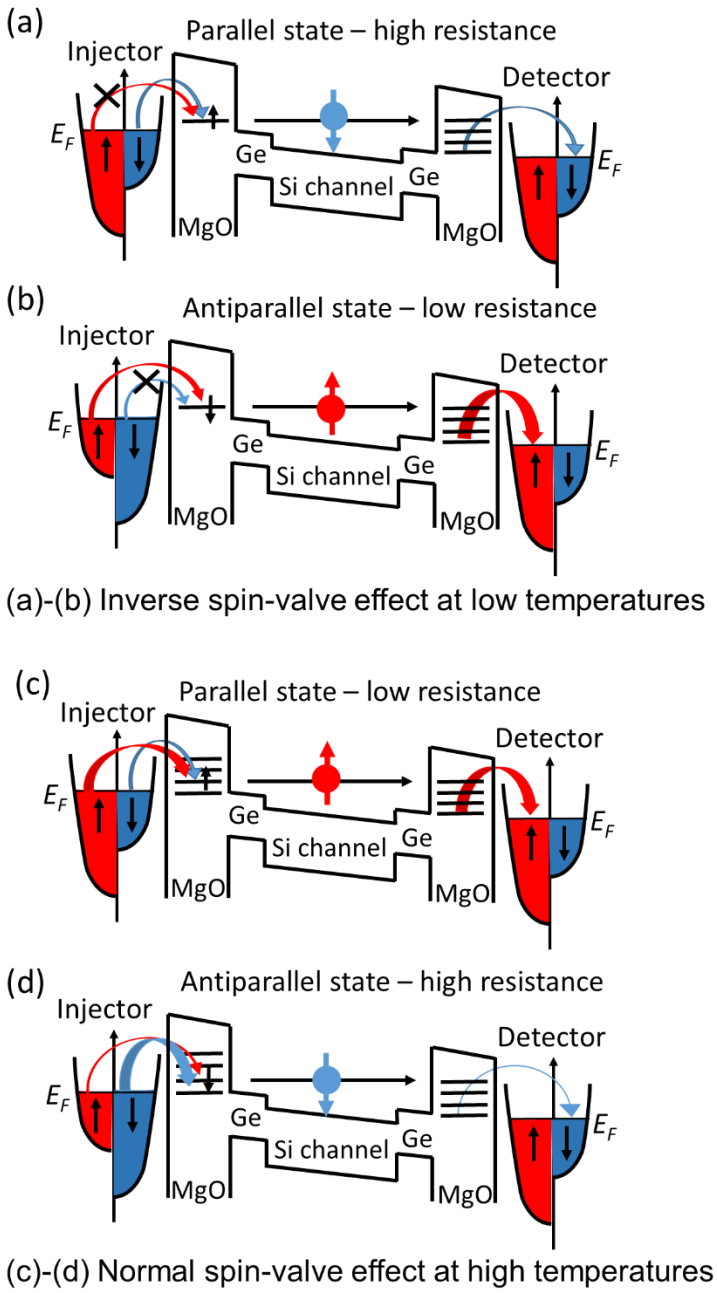

Figure 5.7: Proposed spin-dependent transport model through defect-induced gap states in the MgO barriers for parallel and anti-parallel magnetization configuration, respectively. (a)-(b) At low temperatures, defect-induced gap states in the MgO barrier at the spin injector

side are occupied with majority spins, thus only minority spins can tunnel through the MgO barrier because of the Pauli exclusion principle (spin-blockade effect). This leads to the inverse spin-valve effect, where the resistance is high at (a) parallel and low at (b) antiparallel magnetization configuration. (c)-(d) At high temperatures, there are more available gap states with higher energy levels for thermally activated tunneling from the spin injector. Moreover, the residence time of majority spins at the defect states can be much shorter at high temperatures. Therefore, the spin-blockade is not effective, thus the normal spin-valve effect is dominant at higher temperature with low resistance at (c) parallel and high resistance at (d) antiparallel magnetization configuration. Reprinted from J. Appl. Phys. 122, 223904 (2017), with the permission of AIP Publishing.

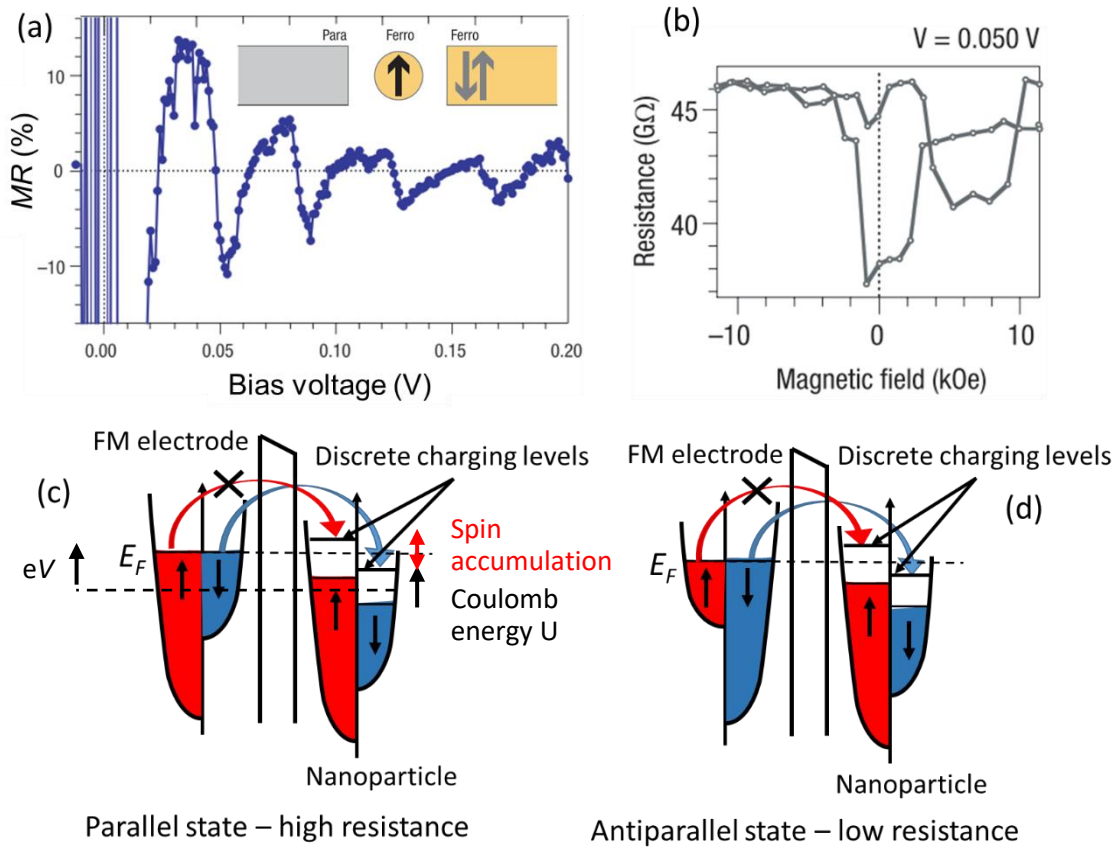

Figure 5.8: (a) Oscillation with negative MR in the Co nanoparticle system. Inset shows the spin transport model of the nanoparticle system: paramagnet / ferromagnetic nanoparticle / ferromagnet double tunnel junction. (b) The negative MR signal of the Co nanoparticle system observed at a bias voltage $V = 0.05$ V [9]. (c)-(d) Model for negative MR in the parallel and anti-parallel state at a certain bias voltage close to a Coulomb staircase (discrete energy level of Coulomb blockade). Reprinted from Nature Mater. 4, 57-61 (2005), with the permission of Nature Publishing Group.

5.5. Spin-dependent output voltage

In this section, I investigate the spin-dependent output performance of our devices. Previous studies on the spin injection into Si channels reported a low read-out voltage of only a few μV in 4 terminal measurements, and about 1 mV in 3 terminal measurements. In Chapter 4, it is succeeded in increasing the spin-dependent output voltage up to 13 mV in nanoscale spin-valve devices with EB evaporated Fe/MgO/Ge junctions [1]. In this chapter, I have significantly improved the crystal quality of the Fe/MgO/Ge junctions by using MBE, as evidenced by the much higher device resistance at 4.3 K (~ 10^8 Ω compared to ~ 10^3 Ω of my previous devices fabricated by EB evaporation). Therefore, it is reasonable to expect higher spin-dependent output voltage. In Fig. 5.9(a), the spin-dependent output $|\Delta V| = |\Delta R/R|V$ was plotted as a function of the bias voltage V at 15 K. The Fig. 5.9(b) shows the dependence of MR ratio on bias voltage. In this device, I achieved $|\Delta V|$ = 20 mV at V = 0.9 V, which is among the highest values reported so far in lateral Si-based spin-valve devices.

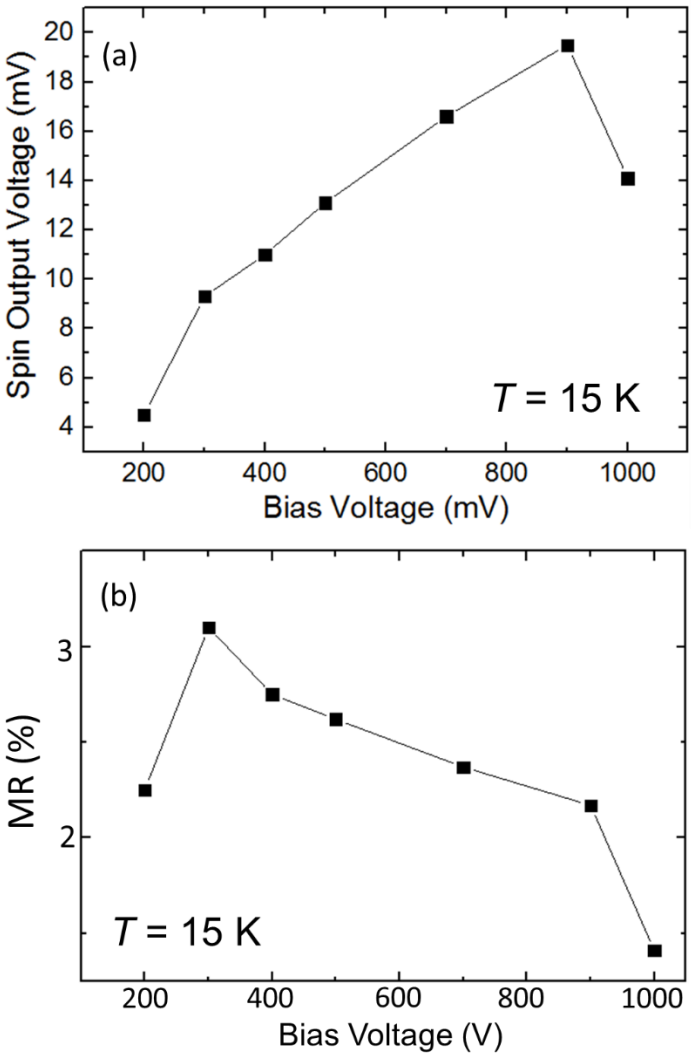

Figure 5.9: (a) Bias voltage dependence of the spin-dependent output voltage $|\Delta V| = (|\Delta R|/R)V$ of the device at 15 K. The highest output voltage $|\Delta V|$ of 20 mV was achieved at the bias voltage of 0.9 V. (b) The bias voltage dependence of $|\Delta R|/R$ at 15 K. Reprinted from J. Appl. Phys. 122, 223904 (2017), with the permission of AIP Publishing.

5.6. Summary

In this chapter, the investigation of the spin transport in the nano-scale Si spin-valve devices prepared by MBE was presented. A large spin-valve effect with $|\Delta R|$ up to 57 kΩ, corresponding to $|\Delta R/R| = 3\%$, has been clearly observed. The sign of the spin-valve effect is reversed at low temperatures, suggesting the possibility of the spin-blockade effect of defect states in the MgO tunnel barrier. The highest spin-dependent output voltage is 20 mV at the bias voltage of 0.9 V at 15 K, which is among the highest values reported so far in lateral Si-based spin-valve devices. My result is an important step towards the realization of nano-scale spin-MOSFETs. The results in this chapter have been published in JAP **122**, 223904 (2017) and has been selected as the AIP Science Highlight paper and JAP Featured paper.

References

1. Hiep, D. D., Tanaka, M. & Hai, P. N. Spin transport in nanoscale Si-based spin-valve devices. *Appl. Phys. Lett.* **109,** 232402 (2016).
2. Gould, C. *et al.* Tunneling anisotropic magnetoresistance: A spin-valve-like tunnel magnetoresistance using a single magnetic layer. *Phys. Rev. Lett.* **93,** 1–4 (2004).
3. Rüster, C. *et al.* Very Large Tunneling Anisotropic Magnetoresistance of a (Ga,Mn)As/GaAs/(Ga,Mn)As Stack. *Phys. Rev. Lett.* **94,** 027203 (2005).
4. Moser, J. *et al.* Tunneling anisotropic magnetoresistance and spin-orbit coupling in Fe/GaAs/Au tunnel junctions. *Phys. Rev. Lett.* **99,** 1–4 (2007).

5. Yuasa, S., Nagahama, T., Fukushima, A., Suzuki, Y. & Ando, K. Giant room-temperature magnetoresistance in single-crystal Fe/MgO/Fe magnetic tunnel junctions. *Nat. Mater.* **3,** 868–871 (2004).

6. Weber, B. *et al.* Spin blockade and exchange in Coulomb-confined silicon double quantum dots. *Nat. Nanotechnol.* **9,** 430–435 (2014).

7. Ono, K., Austing, D. G., Tokura, Y. & Tarucha, S. Current Rectification by Pauli Exclusion in a Weakly Coupled Double Quantum Dot System. *Science (80-.).* **297,** 1313–1317 (2002).

8. Txoperena, O. *et al.* Impurity-Assisted Tunneling Magnetoresistance under a Weak Magnetic Field. *Phys. Rev. Lett.* **113,** 1–6 (2014).

9. Yakushiji, K. *et al.* Enhanced spin accumulation and novel magnetotransport in nanoparticles. *Nat. Mater.* **4,** 57–61 (2005).

CHAPTER 6

INVESTIGATION of THE ROLE of BALLISTIC TRANSPORT IN NANOSCALE Si CHANNEL

In this chapter, the investigation of the role of ballistic transport in my nanoscale Si spin-valve device was described. I have prepared the Si devices with the long channel lengths of L = 500 nm, 1 μm, and 6 μm, and measured the spin-valve effect in these devices, to compare to the 20 nm Si channel device. Two important roles of (quasi) ballistic transport in the nanoscale Si channel have been demonstrated: (i) generation of spin-valve effect even when there is no barrier at room temperature, and (ii) suppress spin-flip scattering to achieve a higher spin-valve ratio at low temperature. The results in this chapter have been published in AAPPS Bulletin 28, 7-15 (2018) – Featured paper.

Chapter 6

6.1. Spin-valve device structures

All of the spin-valve devices were fabricated on n-type Si (100) substrates with an electron density $n = 1\times10^{18}$ cm^{-3}. The Si substrates were cleaned by H_2SO_4/H_2O_2 solution, followed by diluted hydrofluoric acid solution to remove the native oxide layer, and then rinsed in de-ionized water. After that, the substrates were introduced into a molecular-beam-epitaxy (MBE) chamber with a base pressure of 1×10^{-8} Pa for deposition of a 1 nm-thick Ge spacer, a 2 nm-thick MgO tunnel barrier, a 10 nm Fe layer, and a 1 nm-thick MgO capping layer. Knudsen cells were used for thermal evaporation of Ge and Fe, while a low-power electron-beam evaporator was used to deposit MgO with a slow rate of 0.03 Å/s. In-situ reflection high energy electron diffraction confirmed that MgO grown on the Ge buffer layer became crystalline when the MgO thickness exceeded 1 nm.

After depositing the MgO/Ge tunnel barrier and the Fe electrodes by MBE, e-beam lithography and Ar ion-milling techniques were used to fabricate the long Si channel length spin-valve devices. Details of the fabrication process are described in Chapter 3. Figure 6.1 illustrates the device structure examined in this work. In this chapter, I have fabricated devices with different Si channel length from 500 nm to 6 μm, to compare with the 20 nm Si channel spin-valve device, in order to investigate the role of ballistic transport in the nanoscale Si channel spin-valve device.

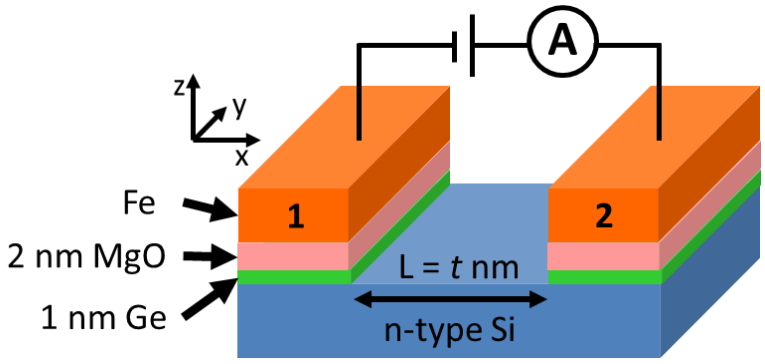

Figure 6.1: Schematic spin-valve device structure with a Fe/MgO/Ge spin injector / detector and the variable Si channel length. The Si channel length L is varied from 500 nm to 6 μm to compare with the 20 nm Si channel length device in the similar growing condition.

6.2. Spin-valve signal in the diffusive regime

It is well-known that when spin polarized electrons are injected from FM into SC, the spin injection efficiency is strongly suppressed by the conductivity mismatch problem [1,2]. When there is no barrier between the FM layer and the SC channel, the spin polarization of the current at the FM/SC interface is given by $(SP)_I = \left(\frac{J_+ - J_-}{J_+ + J_-}\right)_I = \frac{\beta}{1 + r_N / r_F}$. Here, β is the spin-polarization of the FM layer, r_F and r_N are characteristic resistances defined by $r_F = \rho_F l_{sf}^F$ and $r_N = \rho_N l_{sf}^N$, where ρ_F, ρ_N are the resistivity of the FM and SC, and l_{sf}^F, l_{sf}^N are the spin-diffusion length in FM and SC. The ratio r_N / r_F determines the spin polarization at the interface. Using $\rho_F \sim 1\times10^{-5}$ Ωcm and $l_{sf}^F \sim 2$ nm for Fe, $\rho_N = 2\times10^{-2}$ Ωcm for n-Si ($n = 10^{18}$

cm^{-3}) and assuming that l_{sf}^{N} ~10 μm, the ratio r_N / r_F is as large as 1×10^7. This means that there is almost no spin polarization at the interface between Fe and n-Si. The situation is even worse for the spin-valve ratio in the FM/SC/FM structure. Assuming that the length of the SC layer $t_N << l_{sf}^{N}$, the spin-valve ratio is given by $\frac{\Delta R}{R} = 8\beta^2 \left(\frac{r_F}{r_N} \frac{l_{sf}^{N}}{t_N} \right)^2$. For the Fe/n-Si interface, even when t_N = 20 nm, the ratio $\left(\frac{r_F}{r_N} \frac{l_{sf}^{N}}{t_N} \right)^2$ is of the order of 10^{-9}, which means that there is almost no spin-valve effect. The conductivity mismatch problem can be avoided by inserting a barrier between the FM and SC [2,3], which has been widely used to obtain spin injection into SC. However, this method still has some problems. While spin injection from FM into SC through a barrier has been definitely demonstrated, typical values of the spin-valve ratio reported so far in lateral devices are as small as 0.01% ~ 0.1%. Furthermore, high-resistance barriers at the source/drain electrodes are not desired from the viewpoint of current-driving capability of spin-transistors. On the other hand, the conductivity mismatch problem can also be avoided by using nanoscale SC channels with ballistic (or quasi-ballistic) transport. If the SC channel length is comparable or shorter than the electron mean free path, the transport regime changes from diffusive to (quasi) ballistic. In this case, the Ohm's law and diffusion equations used to derive the spin-polarized current are no longer valid. The transport in the SC channel may be modeled using quantum mechanics rather than classical transport equations of electrons. In such a case, the transfer matrix method may be used to calculate the spin-polarized transport in the SC channel. Such a method was used to calculate the magnetocurrent in spin-MOSFETs [4]. The advantages of using ballistic transport to

overcome the conductivity mismatch are (i) high spin-valve ratio, similar to tunneling magnetoresistance (TMR), can be achieved, and (ii) spin-valve effect can be observed even if there is no tunnel barrier, allowing high current driving capability. Unfortunately, there have been very few experimental studies on the FM/SC/FM structure with a nanoscale SC channel. Exceptional one is MnAs / GaAs (10-30nm) / MnAs vertical spin-valve structures grown by MBE [5], which demonstrates a spin-valve ratio as large as 8%.

6.3. Role of ballistic transport in the nanoscale Si channel

To demonstrate the role of ballistic transport in our nanoscale Si channel, the Si spin-valve devices with the long channel lengths of L = 500 nm, 1 μm, and 6 μm have been prepared and measured. The channel of these devices is long enough so that electron transport is diffusive, making it possible to compare them with the nanoscale Si spin-valve devices. The table 6.1 shows the comparison of the spin-valve MR ratio between the long Si channel lengths, where the electron transport is diffusive, and the 20 nm Si channel length in which electron transport is considered as ballistic.

Temp	***L* = 20 nm**	***L* = 500 nm**	***L* = 1 μm**	***L* = 6 μm**
	Δ*R/R* (%)	**Δ*R/R* (%)**	**Δ*R/R* (%)**	**Δ*R/R* (%)**
15	**-3.1**	**-2.2**	**-2**	**-1.8**
50	-1.08	-0.86	-0.74	-0.7
100	-0.4	-0.33	-0.31	-0.28
150	-0.09	-0.08	-0.08	-0.057
200	0	0	0	0
250	0.033	0.02	0.018	0.011
300	**0.042**	**0**	**0**	**0**

Table 6.1: The comparison of the spin-valve MR ratio measured at different temperatures of various devices with different Si channel length.

6.3.1. Generation of the spin-valve effect without a tunnel barrier

The first advantage of ballistic transport in the Si-based spin-valve channel is the ability of generating the spin-valve effect even without a tunnel barrier. Figure 6.2(a) shows the MR curves measured at room temperature for the nanoscale channel device with L = 20 nm, while Figs. 6.2(b)-(d) show those of long-channel devices with L = 500 nm, 1 μm, and 6 μm, respectively. Here, the MR curves in Figs. 6(a)-(d) are measured with a bias voltage of 80 mV. At room temperature, all the devices show low resistance values of the order of 10 Ω. The low resistance indicates that the tunnel barriers of those devices are no longer effective

due to various thermally activated transport processes through defect states in the barriers. Thus, the barrier resistance is negligible, and no spin-valve effect can be expected for the long-channel devices. Indeed, the data in Figs. 6.2(b)-(d) show no spin-valve effect for the devices with L = 500 nm, 1 μm, and 6 μm, as expected from the diffusion theory. In contrast, Fig. 6(a) shows a clear spin-valve effect of about 0.042% for the nanoscale device, even though there is no barrier for this device at room temperature. This demonstrates the important role of (quasi) ballistic transport in generating the spin-valve effect when there is no barrier.

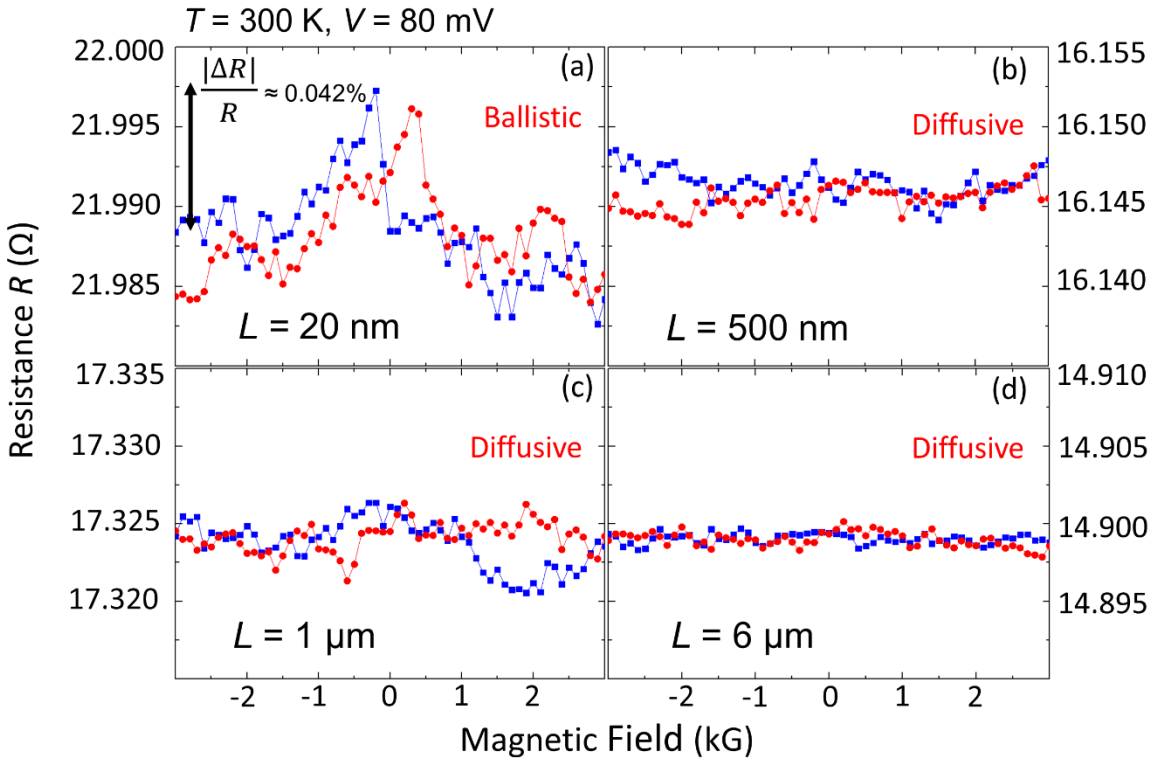

Figure 6.2: (a)-(d) Magnetoresistance of local spin-valve effect of several Si spin-valve devices with different channel length of L = 20 nm, 500 nm, 1 μm, and 6 μm, respectively, measured at 300 K with a bias voltage of 80 mV. All the devices show the low resistance values of the order of 10 Ω, indicating that the tunnel barriers of those devices are no longer effective. Reprinted from J. Appl. Phys. 122, 223904 (2017), with the permission of AIP Publishing.

6.3.2. Suppression of spin-flip scattering to achieve a higher spin-valve ratio at shorter channel length

The second advantage of ballistic transport in the Si-based spin-valve channel is the ability of suppressing the spin-flip scattering to achieve a higher spin-valve ratio at shorter channel length. Figures 6.3 shows the MR curves of devices at 15 K, measured with a bias voltage of 300 mV. At this low temperature, all the devices show high resistance values of MΩ, indicating that thermally activated transport processes through defect states are strongly suppressed and that the barriers are effective for suppressing the conductivity mismatch in long-channel devices. As a result, all the devices show relatively large spin-valve ratios. However, the data clearly show that the spin-valve ratio systematically decreases with increasing channel length; the MR ratio decreases from ~ 3% for L = 20 nm to 2.2%, 2% and 1.8% for L = 500 nm, 1 μm, and 6 μm, respectively. Figure 6.4 shows the dependence of spin-valve ratio $|\Delta R/R|$ on the channel length L in the long channel devices (L = 0.5 μm, 1 μm and 6 μm), in which the electron transport is under diffusive regime. The drop of the spin-valve ratio is slow, consistent with the long spin-diffusion length in Si. Performing the best fitting with $|\Delta R/R| \sim e^{\frac{-L}{\lambda_n}}$, where λ_N is the spin diffusion length in Si, I deduce the λ_N ~ 5.5 μm, which is consistent with data reported in literature.

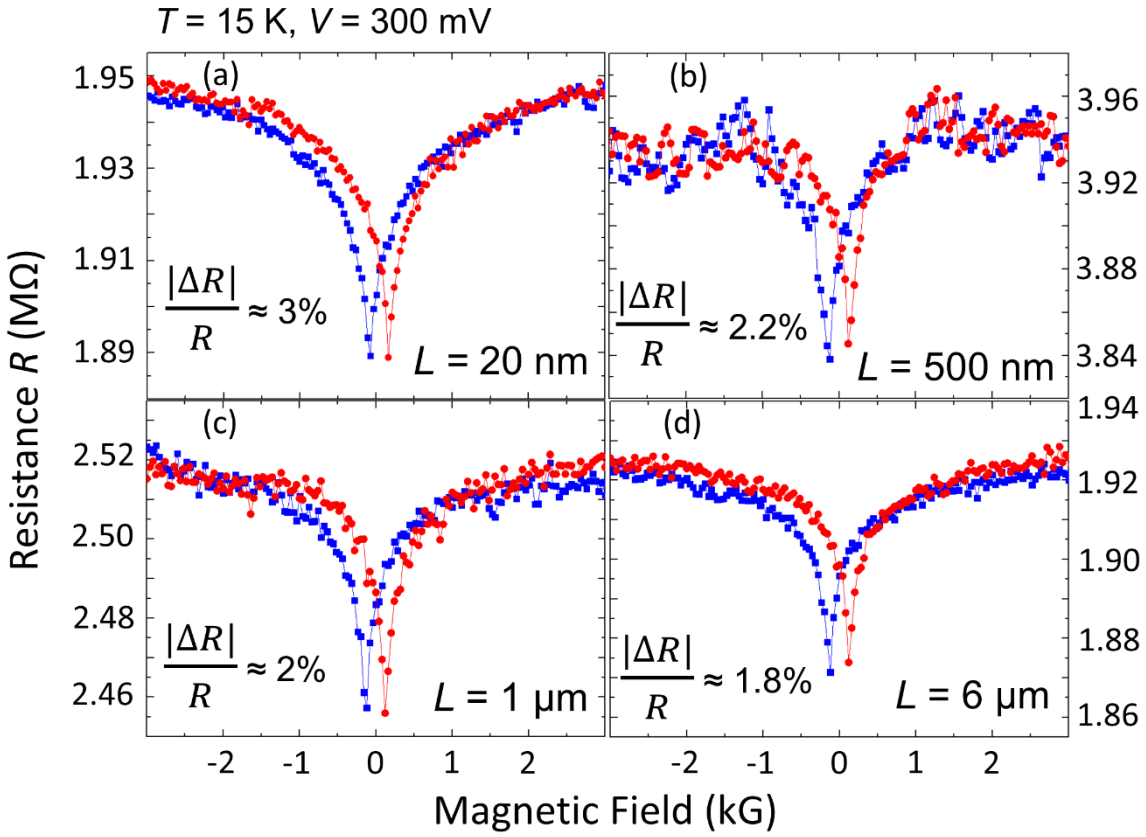

Figure 6.3: (a)-(d) Magnetoresistance of local spin-valve effect of several Si spin-valve devices with different channel length of L = 20 nm, 500 nm, 1 μm, and 6 μm, respectively, measured at 15 K with a bias voltage of 300 mV. All the devices show the high resistance values of the order of MΩ, indicating effectiveness of the tunnel barriers. Reprinted from J. Appl. Phys. 122, 223904 (2017), with the permission of AIP Publishing.

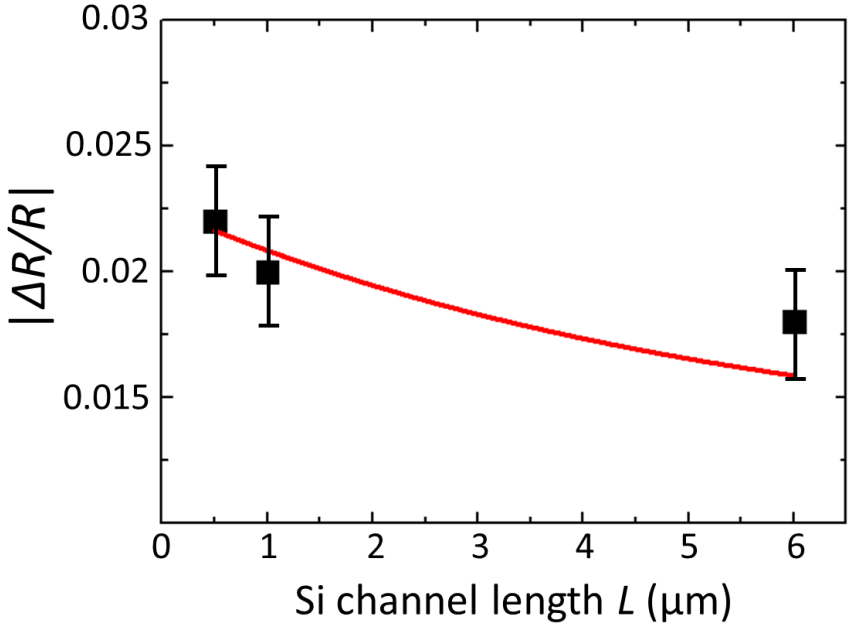

Figure 6.4: The dependence of spin-valve ratio on the Si channel length in the long channel devices. The red line shows the best fitting curve $|\Delta R/R| \sim e^{\frac{-L}{\lambda_n}}$, with $\lambda_n \sim 5.5$ μm.

6.4. Summary

The results in this chapter demonstrate two important roles of (quasi) ballistic transport in the nanoscale Si channel: (i) generation of spin-valve effect even when there is no barrier at room temperature, and (ii) suppress spin-flip scattering to achieve a higher spin-valve ratio at low temperature. Indeed, a large spin-valve ratio of 3%, which is much larger than that observed in μm-long Si channel devices reported before, has been obtained. Nevertheless, the electron transport in my nanoscale devices may be quasi ballistic rather than fully ballistic, because the channel length (20 nm) is not much shorter than that of the mean free path of 20

~ 40 nm for n-type Si with $n = 10^{18}$ cm^{-3} [6]. By using lightly-doped Si substrates and further downsizing the Si channel length to sub-10 nm, it is possible to achieve fully ballistic transport and higher spin-valve signals. The results in this chapter have been published in AAPPS Bulletin 28, 7-15 (2018) – Featured paper.

References

1. Schmidt, G., Ferrand, D., Molenkamp, L. W., Filip, A. T. & van Wees, B. J. Fundamental obstacle for electrical spin injection from a ferromagnetic metal into a diffusive semiconductor. *Phys. Rev. B* **62,** R4790–R4793 (2000).

2. Fert, A. & Jaffrès, H. Conditions for efficient spin injection from a ferromagnetic metal into a semiconductor. *Phys. Rev. B* **64,** 184420 (2001).

3. Rashba, E. I. Theory of electrical spin injection: Tunnel contacts as a solution of the conductivity mismatch problem. *Phys. Rev. B* **62,** R16267–R16270 (2000).

4. Sugahara, S. & Tanaka, M. A spin metal–oxide–semiconductor field-effect transistor using half-metallic-ferromagnet contacts for the source and drain. *Appl. Phys. Lett.* **84,** 2307–2309 (2004).

5. Hai, P. N., Sakata, Y., Yokoyama, M., Ohya, S. & Tanaka, M. Spin-valve effect by ballistic transport in ferromagnetic metal (MnAs)/semiconductor (GaAs) hybrid heterostructures. *Phys. Rev. B - Condens. Matter Mater. Phys.* **77,** 1–6 (2008).

6. Qiu, B. *et al*. First-principles simulation of electron mean-free-path spectra and thermoelectric properties in silicon. *EPL (Europhysics Lett.* **109,** 57006 (2015).

CHAPTER 7

OPTIMIZATION of THE MgO TUNNEL BARRIER THICKNESS

In this chapter, the investigation of the spin transport in nanoscale silicon (Si)-based spin-valve devices with a 20 nm Si channel and various stacks of Fe/MgO/Ge as the spin injector/detector was conducted. By optimizing the MgO barrier thickness, a large spin-dependent output voltage of 25 mV at 15 K, which is the highest value reported so far, was achieved.

7.1. Spin-valve device structures

In this chapter, the spin-valve devices were fabricated with ferromagnetic electrodes and a tunnel barrier deposited on highly doped n-type Si (100) substrates with an electron density $n = 1\times10^{18}$ cm^{-3}. Before thin film deposition, the substrates were cleaned by acetone, followed by H_2SO_4/H_2O_2 solution, then etched in diluted hydrofluoric acid solution to remove the native oxide layer, and rinsed in de-ionized water. After the cleaning process, stacking layers of Fe (electrode) / MgO (tunnel barrier) / Ge (buffer layer) (from the top to the bottom) for the ferromagnetic electrodes and the tunnel barrier were deposited on Si.

These stacking layers were deposited by molecular-beam epitaxy (MBE). After the cleaning process, Si substrates were introduced into a MBE chamber with a base pressure of 1×10^{-8} Pa. In this study, in order to optimize the MgO tunnel barrier layer, the stack of 1.1 nm MgO capping layer / 10 nm Fe / (1.5 – 3.5 nm) MgO / 1 nm Ge on Si substrates was grown from the top to the bottom. In the MBE growth, Knudsen cells were used for thermal evaporation of Ge and Fe, while a low-power electron-beam evaporator was used to deposit MgO at a slow rate of 0.03 Å/s.

After depositing the tunnel barrier and the ferromagnetic layer, the electron-beam lithography (EBL), EB evaporation, lift-off, and ion-milling techniques were employed to fabricate nanoscale Si spin-valve devices. Finally, the Au (40 nm) / Cr (5 nm) pad electrodes were formed by EB evaporation. Figure 7.1(a) shows the schematic structure of our devices. A typical top-view scanning electron microscopy (SEM) image of our spin-valve devices with a 20 nm Si channel is shown in the Fig. 7.1(b).

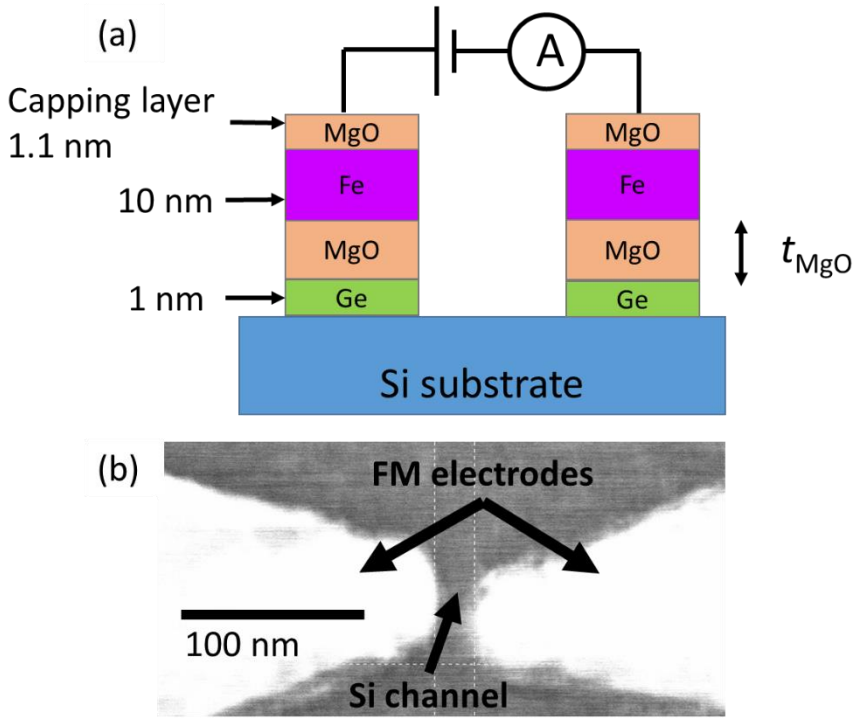

Figure 7.1: (a) Schematic spin-valve device structure with a Fe/MgO/Ge spin injector / detector and a 20 nm Si channel. The MgO thickness t_{MgO} is varied from 1.5 to 3.5 nm. (b) Scanning electron microscopy image (top view) of a device with a 20 nm Si channel between the Fe electrodes.

7.2. Conductance characteristics

This section describes the investigation of the conductance characteristics of the Si-based nanoscale 2 terminal spin-valve device with different thicknesses of the MgO tunnel barrier layer.

Figure 7.2(a) shows the current – voltage characteristic (*I* – *V* curves) at 50 – 300 K of devices grown by MBE with a 1.5 nm-thick MgO tunnel barrier. The non-linear *I* – *V* curves were observed, suggesting that the resistances of the devices are dominated by the electron transport through the spin-valve structure consisting of Fe/MgO/Ge – Si – Ge/MgO/Fe. The strong dependence of the *I* – *V* curves on temperature was also found; the figure 7.2(b) shows the resistance of this device as a function of temperature, measured with a bias voltage of 300 mV. I observed a rapid increase of the resistance as temperature decreases, from the order of ~ 10^1 Ω at 300 K to ~ 10^7 Ω at 15 K. Such behavior indicates that the electron transport through the barrier occurs not by direct tunneling, but by thermally activated hopping through defect states in the MgO tunnel barrier [1]. From the temperature dependence of the resistance, it is able to evaluate the contribution of the parasitic AMR of the Fe electrodes to the total spin-valve effect at various temperatures as follows. The total device resistance R can be decomposed into two components: $R = R_{Fe} + R_{sv}$, where R_{Fe} is the parasitic series resistance of the Fe electrodes and R_{sv} is the intrinsic tunneling resistance of the spin-valve structure. Since the parasitic $R_{Fe}(T)$ decreases as temperature decreases, $R_{Fe}(T) \leq R_{Fe}(300K) < R(300K) \approx 20\ \Omega$. The AMR effect $|\Delta R_{Fe}/R_{Fe}|$ of Fe is in the order of 0.1%, thus the magnetoresistance of Fe $|\Delta R_{Fe}|$ is in the order of 0.2 Ω. From this consideration, it is possible to estimate the contribution of the parasitic AMR effect of $|\Delta R_{Fe}/R(T)|$ at various temperatures: For example, $|\Delta R_{Fe}/R(T)|$ at 15 K should be in the order of 10^{-8} which is extremely small compared with the observed MR signal of 2% – 3%, as shown later. Therefore, the contribution of the parasitic AMR effect of the Fe electrodes is negligible at low temperatures.

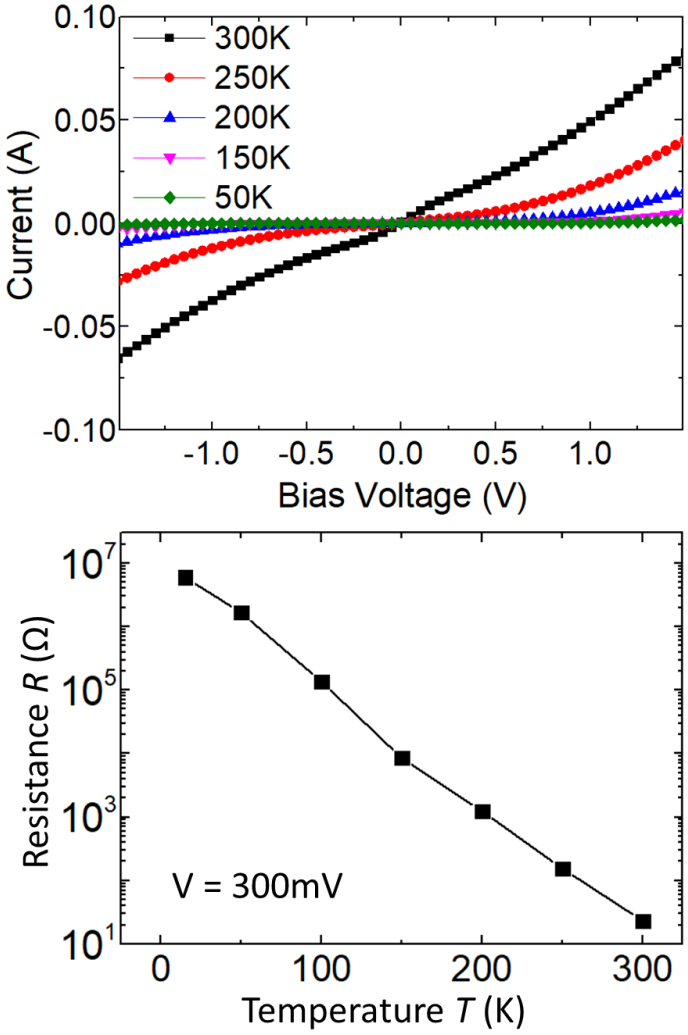

Figure 7.2: (a) Current – voltage characteristics (I – V curves) of a MBE-grown device with an MgO thickness t_{MgO} = 1.5 nm. (b) shows the temperature (T) dependence of the resistance R measured at 300 mV.

7.3. Spin-dependent transport characteristics

In this section, the investigation of the spin-dependent transport characteristics of the Si-based nanoscale 2 terminal spin-valve devices fabricated by the MBE method with different MgO barrier thicknesses was presented.

7.3.1 Local spin-valve effect

Conventionally, the spin transport in Si has been studied by the Hanle effect or 4-terminal non-local spin-valve measurements rather than the 2-termimal local spin-valve measurement to avoid the parasitic local MR effect, such as anisotropic magnetoresistance (AMR) or tunneling AMR (TAMR) effects. However, in nanoscale channel devices, the spin transport time in the Si channel is too short for spin precession induced by the external magnetic field, thus the Hanle effect cannot be used. Furthermore, the 4-terminal non-local measurement has no advantages compared with the local measurement in the nanoscale channels, as discussed before [1,2]. Furthermore, I have shown that it is possible to distinguish the intrinsic spin-valve effect from parasitic local effects by systematic measurements of the bias voltage dependence, temperature dependence, and magnetic-field direction dependence of the MR signal in previous chapters [2,1]. Therefore, in this chapter, I employed the two-terminal local spin-valve measurement to investigate the spin transport in the nanoscale spin-valve devices.

Figure 7.3(a) shows the MR characteristic of a MBE-grown spin-valve device with an MgO tunnel barrier (t_{MgO} = 1.5 nm) at 15 K, measured with a bias voltage of 500 mV and a magnetic field applied along the Si channel (*x* direction in Fig. 7.1(a)). The inset show the minor loop of MR signal. An inverse magnetoresistance effect with a large drop of resistance $|\Delta R| \sim 30$ kΩ, corresponding to $|\Delta R/R| = 2.5$ %, was observed. Note that the $|\Delta R|$ and $|\Delta R/R|$

values are five orders of magnitude larger than that of the parasitic AMR effect of the Fe electrodes at 15 K ($|\Delta R_{Fe}| \sim 0.2\ \Omega$ and $|\Delta R_{Fe}/R| = 10^{-8}$). Furthermore, I measured $|\Delta R|$ at various bias voltage V, and found that $|\Delta R|$ strongly depends on V, as shown in Fig. 7.3(b). This cannot be explained by the AMR effect, because $|\Delta R_{Fe}|$ does not depend on the bias voltage. Moreover, the $|\Delta R| - V$ characteristic closely follows the $R - V$ characteristic as shown in Fig. 7.3 (b), indicating that the observed MR effect originates from the spin-dependent tunneling process of electrons between the Fe electrodes and the Si channel through the MgO/Ge barrier. Note that the MR of the devices prepared by MBE is negative (inverse MR, as shown in Fig. 7.3(a)), contrasting to the positive MR in the conventional spin-valve effect. The origin of the inverse MR in MBE devices has been explained in Chapter 5 as the result of the spin-blockade effect of defect states in the MgO barrier [1].

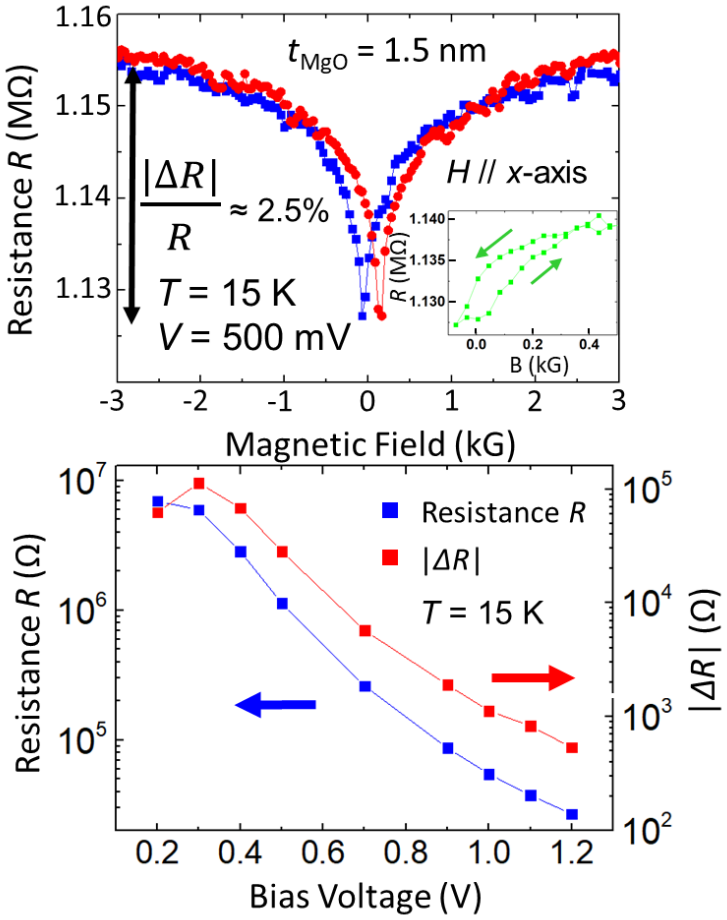

Figure 7.3: (a) Local magnetoresistance (MR) of a MBE-grown device with a 1.5 nm-thick MgO layer at 15 K, measured with a bias voltage of 500 mV. The inset shows the minor loop MR. (b) Magnetoresistance $|\Delta R|$ and device resistance R as a function of the bias voltage at 15 K of the same device as shown in (a).

7.3.2. Dependence of spin-valve signal on bias voltage in different MgO thicknesses

This part describes the investigation of the dependence of spin-valve signal on the bias voltage in different MgO thicknesses.

Figure 7.4(a) shows the dependence of the MR ratio on the bias voltage for devices with different MgO barrier thicknesses (t_{MgO} = 1.5 – 3.5 nm) at 15 K. At low bias voltages ($V \leq$ 300 mV), the device with the thinnest MgO layer (t_{MgO} = 1.5 nm) shows lower MR ratio than the devices with thicker MgO layers ($t_{MgO} \geq$ 2 nm). However, at higher bias voltages ($V >$ 300 mV), the devices with thin MgO layers (t_{MgO} = 1.5 and 2 nm) show better performance than the devices with thick MgO layers (t_{MgO} = 2.5 and 3.5 nm). Especially, the device with t_{MgO} = 1.5 nm maintains the high MR ratio over -2% at the bias voltage as high as 1.1 V.

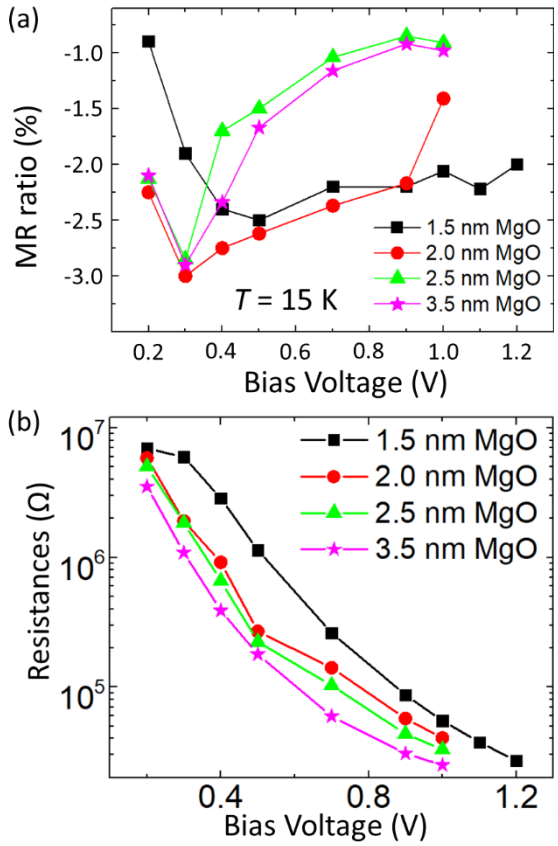

Figure 7.4: (a) Dependence of the MR ratio $|\Delta R|/R$ on the bias voltage in MBE-grown devices with various MgO thicknesses (t_{MgO} = 1.5 – 3.5 nm) at 15 K. (b) Dependence of device resistance R on the bias voltage in devices with various MgO thicknesses.

To understand the dependence of the MR ratio on the bias voltage and on the thickness of the MgO tunnel barrier, it is important to understand the tunneling process of electrons in our devices. First, the strong temperature dependence of the tunnel resistance in my devices indicates that the electron transport through the tunnel barrier is governed by thermally activated hopping via defect states in the barrier. Such defect states, such as oxygen vacancy, are well-known for MgO [3]. Second, the Fig. 7.4(b) shows that the device resistance *decreases* with increasing the MgO barrier thickness, contradicting the expectation from direct tunneling. This can be explained as my proposed model in figure 7.5. During the MgO deposition process, the thicker the MgO layer is, the longer time the MgO layer is exposed to an ultrahigh vacuum, which allows more desorption of oxygen from the MgO layer when the growth rate of MgO is very slow like our case (0.03 Å/s). As a result, the thicker MgO layers can have higher defect-state density than the thinner MgO layers, which enhances the hopping process of electrons via defect states and reduces the device resistance, as shown in the Fig. 7.5.

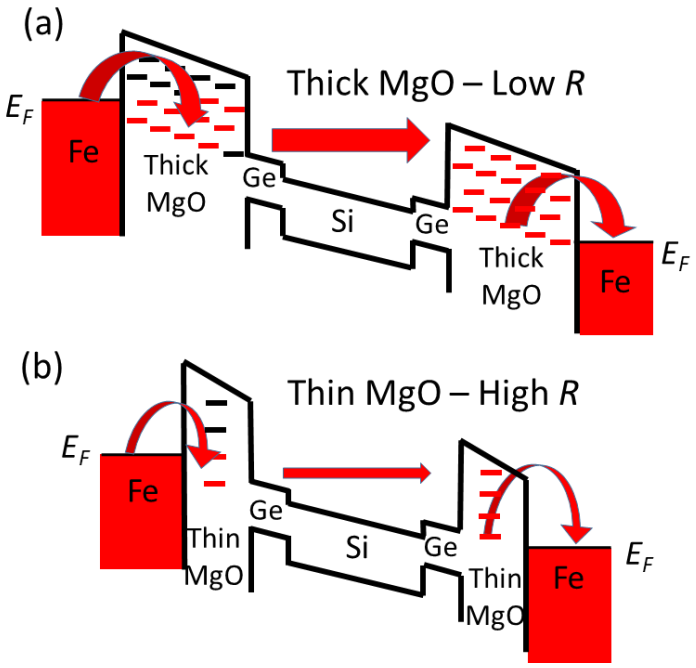

Figure 7.5: The electron transport model to explain the dependence of device resistance *R* on the thickness of MgO tunnel barrier. (a) Electron transport model when MgO layer is thicker, (b) when MgO layer is thinner.

Based on this consideration, I propose a model to explain the bias voltage dependence and the MgO barrier thickness dependence of the MR ratio, which are shown in Fig. 7.6. From the Fe injector, spin-polarized electrons tunnel to the Si channel through defect states inside the MgO barrier. If these defect states are filled with majority spins whose residence time is long enough at low temperatures, only minority spins from the spin injector can go through. Such a "spin-blockade" phenomenon, originated from the Pauli exclusion principle, is well known and has been observed in semiconductor quantum dots and various defect states in semiconductors [4,5]. In the devices grown by MBE, the spin blockade results in the inverse spin-valve effect [1]. At low bias voltages, only defect states close to the Fermi level

are relevant for spin transport. At higher bias voltages, there are more available defect states for spin transport. When the MgO layer is thin, the number of relevant defect states increases slowly with bias voltage, and the spin blockade is effective at both the low and high bias voltages, as shown in Fig. 7.6(a) and 7.6(b). Thus, the inverse MR ratio remains high at high bias voltages for the samples with a thin MgO layer. In contrast, in the devices with a thick MgO layer, the available defect-states increases rapidly with increasing the bias voltage. Thus, both minority and majority spins can transport through the barrier, resulting in the weaker spin-blockade effect, as shown in Fig. 7.6(c) and 7.6(d). Therefore, the inverse MR ratio of devices with the thicker MgO layer decreases rapidly at high bias voltages.

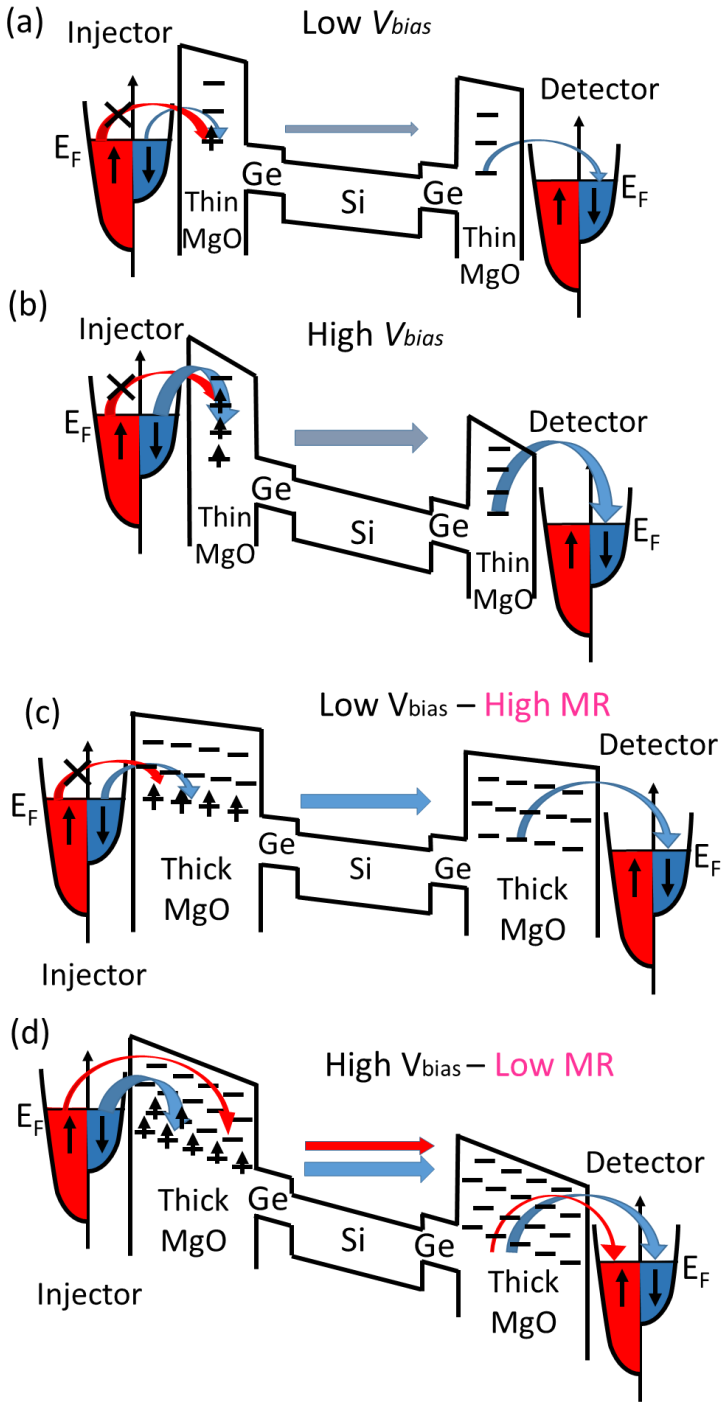

Figure 7.6: Spin-dependent transport model through defect states in the MgO barriers for devices with (a)(b) thin and (c)(d) thick MgO layers, at (a)(c) low and (b)(d) high bias

voltages, respectively. Here, the MgO barrier thickness is exaggerated for clarity. In thin MgO barriers, available defect states for electron tunnelling increase slowly with increasing the bias voltage, thus the spin blockade is effective at both low and high bias voltages. In thick MgO barriers, the available defect states increases rapidly with increasing the bias voltage, thus the spin blockade is weakened at high bias voltages, and the inverse MR ratio drops quickly with increasing the bias voltage.

7.4. Spin-dependent output voltage

This section presents the investigation of the spin-dependent output performance of my devices. Here, large $\Delta V = \Delta R \times I = \Delta R \times (V/R) = (\Delta R/R) \times V$ is important for correct read-out in realistic applications. Previous studies on the spin injection into Si channels reported a low read-out voltage of only a few μV in 4 terminal measurements, and about 1 mV in 3 terminal measurements. Chapter 5 has shown an increase of the spin-dependent output voltage up to 20 mV in nanoscale spin-valve devices Fe/MgO/Ge junctions [1]. In this chapter, by optimizing the MgO thickness, I have succeeded in improving ΔV to the maximum value of 25 mV for the device with the 1.5 nm MgO barrier, which is the highest value reported so far in lateral Si-based spin-valve devices. Figure 7.7 shows the spin-dependent output ΔV as a function of V. ΔV tends to decrease as the MgO layer thickness increases, and significantly drops when t_{MgO} is over 2.5 nm due to the rapid drop of the MR ratio at high bias voltages.

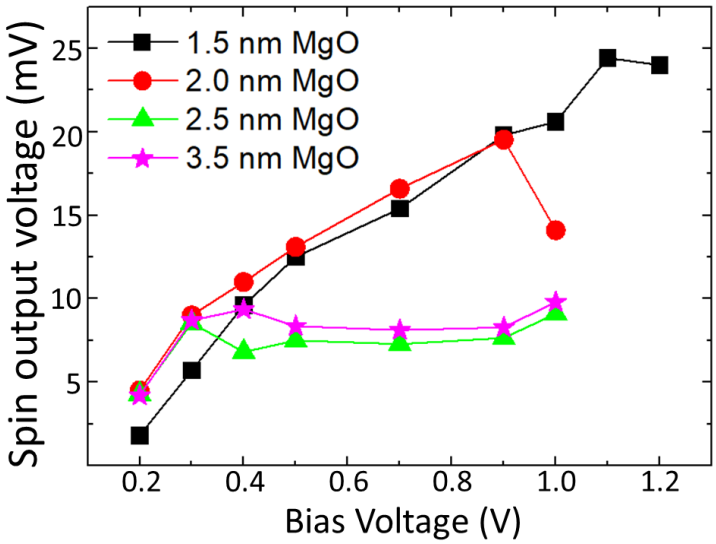

Figure 7.7: The bias voltage dependence of the spin-dependent output voltage of devices with different MgO layer thicknesses. The highest output voltage $|\Delta V|$ of 25 mV was achieved at bias voltage of 1.1 V in the device with a 1.5 nm MgO layer.

7.5. Summary

This chapter shows the investigation of the spin transport in nanoscale Si spin-valve devices prepared by MBE with various spin injectors/detectors. In the device with MgO (1.5 nm) / Ge (1 nm) double layers grown by MBE, I obtained the highest spin-dependent output voltage of 25 mV. The results in this chapter have been submitted and under review.

References

1. Hiep, D. D., Tanaka, M. & Hai, P. N. Inverse spin-valve effect in nanoscale Si-based spin-valve devices. *J. Appl. Phys.* **122,** 223904 (2017).

2. Hiep, D. D., Tanaka, M. & Hai, P. N. Spin transport in nanoscale Si-based spin-valve devices. *Appl. Phys. Lett.* **109,** 232402 (2016).

3. Yuasa, S., Nagahama, T., Fukushima, A., Suzuki, Y. & Ando, K. Giant room-temperature magnetoresistance in single-crystal Fe/MgO/Fe magnetic tunnel junctions. *Nat. Mater.* **3,** 868–871 (2004).

4. Ono, K., Austing, D. G., Tokura, Y. & Tarucha, S. Current Rectification by Pauli Exclusion in a Weakly Coupled Double Quantum Dot System. *Science (80-.).* **297,** 1313–1317 (2002).

5. Weber, B. *et al.* Spin blockade and exchange in Coulomb-confined silicon double quantum dots. *Nat. Nanotechnol.* **9,** 430–435 (2014).

CHAPTER 8

IMPROVEMENT of THE SPIN VALVE RATIO by USING AN Mg BUFFER LAYER between Fe and MgO LAYERS

In this chapter, the investigation of the spin transport in nanoscale silicon (Si)-based spin-valve devices with a 20 nm Si channel and a Fe/Mg/MgO/Ge stack as the spin injector/detector was conducted. By inserting an ultrathin (1 nm) Mg layer in between the tunnel barrier MgO and the Fe electrode to prevent the formation of a magnetically-dead layer, the spin-valve ratio has been increased up to –3.6% at 15 K. This is the highest values reported in Si lateral spin-valve devices. The results in this chapter have been submitted and under review.

8.1. Spin-valve device structures

The highly doped n-type Si (100) substrates with electron density $n = 1\times10^{18}$ cm^{-3} were used for device fabrication. The Si substrates were first cleaned by H_2SO_4/H_2O_2 solution, then etched by diluted hydrofluoric acid solution to remove the native oxide layer, and rinsed in de-ionized water. For evaporation of the tunneling barrier and ferromagnetic electrodes, Molecular-Beam-Epitaxy (MBE) was employed.

After the cleaning process, the substrates were introduced into a MBE chamber with a base pressure of 1×10^{-8} Pa for growing the stack of Fe (electrode) / Mg (spacer) / MgO (tunnel barrier) / Ge (buffer layer) (from the top to the bottom). Knudsen cells were used for thermal evaporation of Ge, Mg and Fe, while a low-power electron-beam evaporator was used to deposit MgO with a slow rate of 0.03 Å/s. In-situ reflection high energy electron diffraction confirmed that MgO grown on the Ge buffer layer became crystalline when the MgO thickness exceeded 1 nm. After thin film deposition, the electron-beam lithography (EBL) and ion-milling techniques were used to fabricate the 20 nm Si channel. Finally, the Au (40 nm) / Cr (5 nm) pad electrodes for wire bonding were deposited by EB evaporation. Figure 8.1 shows the schematic structure of a device.

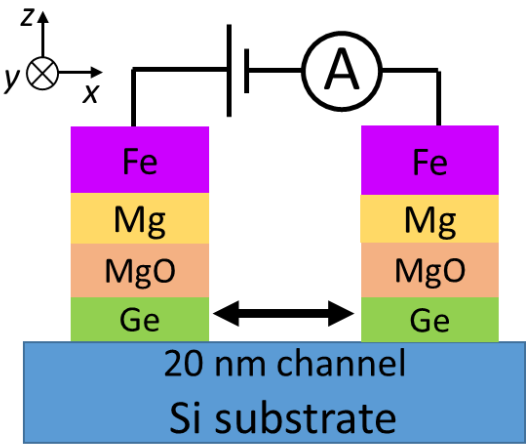

Figure 8.1: The schematic structure of a device with the Mg buffer layer to prevent the formation of a magnetically-dead layer at the interface of Fe and MgO.

8.2. Optimization of the Mg buffer layer thickness

In this section, I have varied the Mg buffer layer thickness and investigated the local spin-valve effect of the Si-based nanoscale spin-valve devices in order to optimize the Mg thickness in this device structure. Figure 8.2(a) shows the device structure in this experiment.

The devices were fabricated with the fixed structure of 10 nm Fe / Mg / 1.5 nm MgO / 1nm Ge but varying the Mg thickness t_{Mg} from 0.5 to 2 nm. Figure 8.2(b) shows the dependence of MR ratio on bias voltage in different Mg thicknesses. The device with a 0.5 nm Mg buffer layer shows the maximum MR ratio lower than those with thicker Mg. However, the device with 2 nm Mg also shows the worse performance than the others. It is

found that the window for high MR ratio is between 1 nm and 1.5 nm Mg buffer layer. Therefore, the optimized thickness of Mg at 1 nm was chosen.

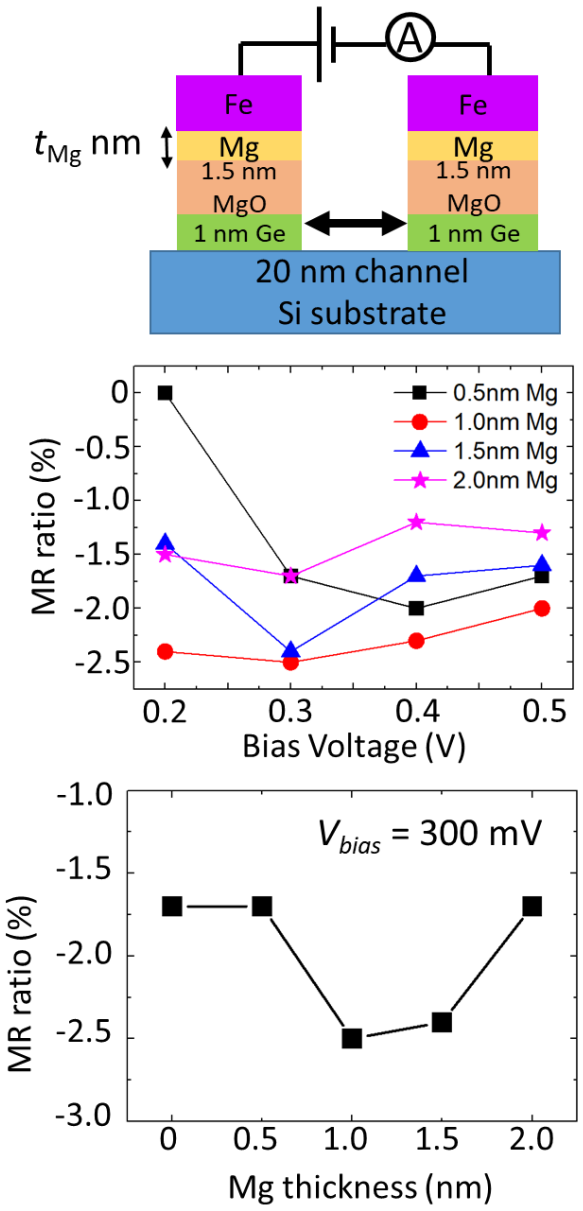

Figure 8.2: (a) The schematic structure of devices which are used for the optimization of Mg buffer layer thickness, (b) the dependence of local spin-valve signal MR on applied bias voltage for various devices with different Mg thickness, and (c) the dependence of local MR ratio on the Mg buffer layer thickness measured at 300 mV.

8.3. Optimization of the MgO tunnel barrier thickness in Mg-inserted device

In this section, a 1 nm Mg buffer layer has been inserted into the device and varied the MgO thickness in order to optimize the MgO thickness in this new structure. Figure 8.3 describes the device structure in this experiment.

Devices were fabricated with the fixed structure of 10 nm Fe / 1 nm Mg / MgO / 1nm Ge but varied the MgO thickness t_{MgO} from 1.5 to 3.5 nm.

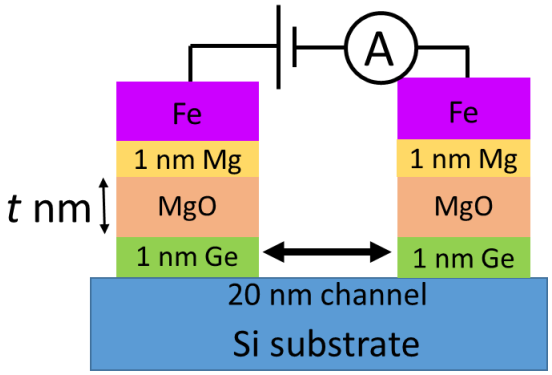

Figure 8.3: The schematic structure of devices which is used for the optimization of MgO tunnel barrier thickness. The MgO thickness is varied from 1.5 to 3.5 nm.

8.3.1. Conductance characteristics

This part shows the investigation of the conductance characteristics of the Si-based nanoscale 2 terminal spin-valve devices with the 1 nm Mg buffer layer.

Figure 8.4(a) shows the current – voltage characteristic (I – V curves) at 50 – 300 K of the device grown by MBE with a 3.5 nm-thick MgO tunnel barrier and a 1 nm-thick Mg insertion layer. The non-linear I – V curves were observed, suggesting that the resistances of

the devices are dominated by the electron transport through the spin-valve structure consisting of Fe/Mg/MgO/Ge – Si – Ge/MgO/Mg/Fe. The strong dependence of the $I - V$ curves on temperature was also found. Figure 8.4(b) shows the resistance of this device as a function of temperature, measured with a bias voltage of 300 mV. Here, a rapid increase of the resistance as temperature decreases, from the order of ~ 10^1 Ω at 300 K to ~ 10^6 Ω at 15 K, was observed. Such behavior indicates that the electron transport through the barrier occurs not by direct tunneling, but by thermally activated hopping through defect states in the MgO tunnel barrier [1]. From the temperature dependence of the resistance, it is possible to evaluate the contribution of the parasitic AMR of the Fe electrodes to the total spin-valve effect at various temperatures as follows. The total device resistance R can be decomposed into two components: $R = R_{Fe} + R_{sv}$, where R_{Fe} is the parasitic series resistance of the Fe electrodes and R_{sv} is the intrinsic tunneling resistance of the spin-valve structure. Since the parasitic $R_{Fe}(T)$ decreases as temperature decreases, $R_{Fe}(T) \leq R_{Fe}(300K) < R(300K) \approx 20\ \Omega$. The AMR effect $|\Delta R_{Fe}/R_{Fe}|$ of Fe is in the order of 0.1%, thus the magnetoresistance of Fe $|\Delta R_{Fe}|$ is in the order of 0.2 Ω. From this consideration, it could be estimated the contribution of the parasitic AMR effect of $|\Delta R_{Fe}/R(T)|$ at 15 K should be in the order of 10^{-7} which is extremely small compared with the observed MR signal of 2% – 3%, as shown later. Therefore, the contribution of the parasitic AMR effect of the Fe electrodes is negligible at low temperatures.

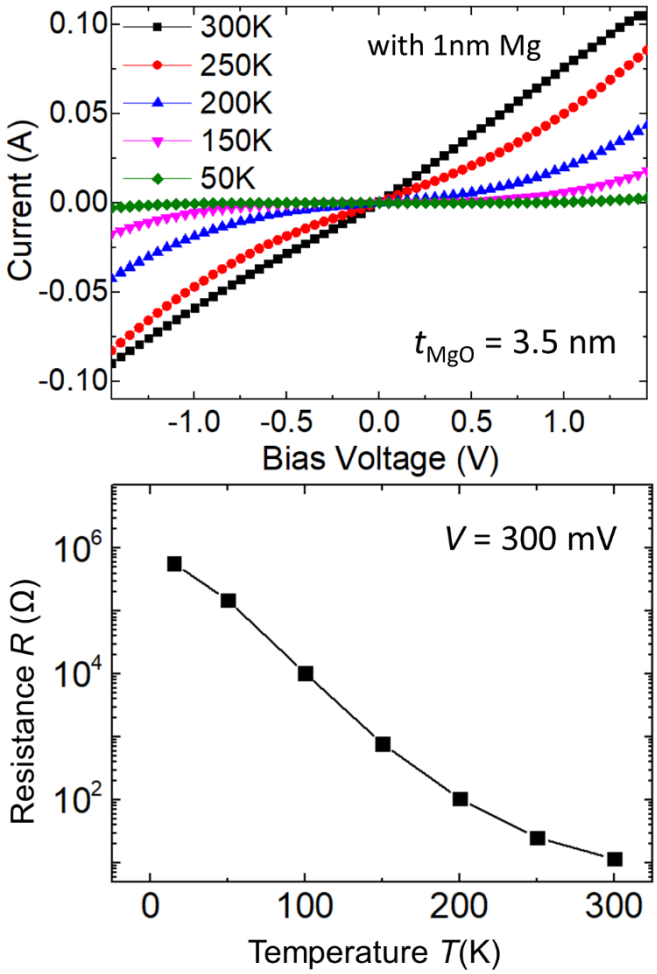

Figure 8.4: (a) Current – voltage characteristics (I – V curves) of a MBE-grown device with an MgO thickness t_{MgO} = 3.5 nm and Mg thickness of 1 nm. (b) The temperature (T) dependence of the resistance R measured at 300 mV.

8.3.2. Local spin-valve effect

In this part, the investigation of the spin-valve effect in devices with the 1 nm Mg layer inserted between the ferromagnetic Fe layer and the tunnel barrier MgO layer was presented. This Mg insertion layer is used to protect the Fe layer from intermixing with other atoms in the MgO barrier and from forming a magnetically-dead layer which reduces the spin

coherence of tunneling electrons [2,3]. Therefore, the Mg insertion layer is expected enhance the spin injection efficiency in my devices. Figure 8.5(a) shows the MR characteristics of a spin-valve device with t_{MgO} = 3.5 nm at 15 K, measured with a bias voltage of 200 mV and a magnetic field applied along the Si channel. In this device, by inserting the ultrathin (1 nm) Mg layer, I have succeeded in improving the local MR ratio up to $|\Delta R| \sim 75$ kΩ and |MR| = 3.6%. Figure 8.5(b) shows the MR ratio of the devices with various t_{MgO} as a function of the bias voltage *V*. At low *V*, the best MR ratio is obtained for the sample with t_{MgO} = 3.5 nm. However, the MR ratio is nearly the same for all the devices at $V \geq 400$ mV.

Finally, it is the discussion about the spin-dependent output voltage ΔV of the devices in this series. Figure 8.5(c) shows ΔV of the devices with various t_{MgO} as a function of *V* at 15 K. It is found that the maximum ΔV in this series is limited to ~ 10 mV, which is lower than in the highest value of 25 mV in the devices without an Mg insertion layer. The reason is the decrease of the MR ratio of the devices with the Mg insertion layer at high bias voltages as shown in Fig. 8.5(b). I conclude that, while inserting the Mg layer between the Fe and the MgO layer helps to increase the MR ratio at low bias voltages, it cannot generate a large spin-dependent output voltage at high bias voltages, which is important in the spin transistor applications.

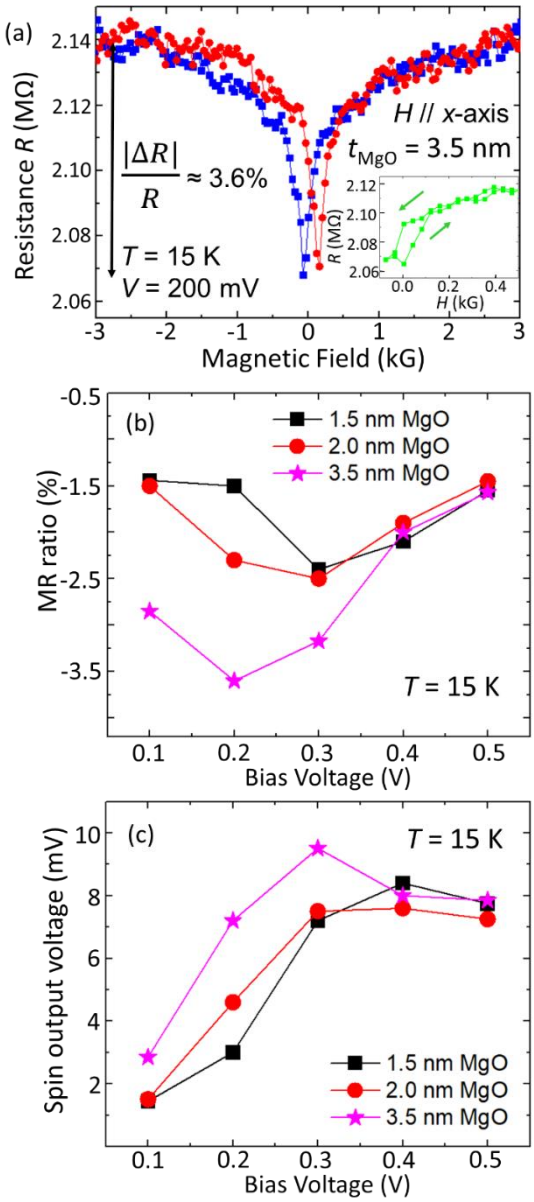

Figure 8.5: (a) Local magnetoresistance of the device grown by MBE with a 1 nm-thick Mg insertion layer and 3.5 nm-thick MgO barrier layer, measured at 15 K with a bias voltage of 200 mV. Inset shows the minor loop MR. (b) Bias voltage dependence of the MR ratio at 15 K for the devices with t_{MgO} = 1.5 nm, 2.0 nm, and 3.5 nm. (c) Bias voltage dependence of the spin-dependent output voltage at 15 K for the devices with t_{MgO} = 1.5 nm, 2.0 nm, and 3.5 nm.

8.4. Summary

This chapter describes the investigation of the spin transport in nanoscale Si spin-valve devices prepared by MBE with various spin injectors/detectors. An ultrathin (1 nm) Mg layer in between the tunnel barrier MgO and the Fe electrodes was utilized to prevent the formation of a magnetically-dead layer at this interface, in order to enhance the spin injection in this Si-based spin-valve structure. By optimizing the Mg buffer layer thickness and MgO tunnel barrier thickness, I have succeeded in improving the MR ratio up to –3.6% in this Si-based spin-valve structure. This value is the highest reported so far in Si lateral spin-valve devices. These results give better understanding and control of the spin transport through the tunnel barrier into Si and will be helpful for improving performance of Si-based spin-valve devices. The results in this chapter have been submitted and under review.

References

1. Hiep, D. D., Tanaka, M. & Hai, P. N. Inverse spin-valve effect in nanoscale Si-based spin-valve devices. *J. Appl. Phys.* **122,** 223904 (2017).
2. Sato, S., Nakane, R., Hada, T. & Tanaka, M. Spin injection into silicon in three-terminal vertical and four-terminal lateral devices with Fe/Mg/MgO/Si tunnel junctions having an ultrathin Mg insertion layer. *Phys. Rev. B* **96,** 235204 (2017).
3. Linn, T. & Mauri, D. Method of forming a barrier layer of a tunneling magnetoresistive sensor. **US Patent,** (2005).

CHAPTER 9

CONCLUSIONS and FUTURE PERSPECTIVES

Conclusions

The purpose of this study is to investigate the spin transport in the nanoscale Si-based spin-valve device with Fe electrodes, (Mg)/MgO/Ge tunnel barriers, and a 20 nm-long Si channel. Key results and conclusions are highlighted below.

In Chapter 1, I gave a brief review of spintronics, the technology which aims to utilize the spin degree freedom of electrons for many applications in nowadays and future technology such as new forms of information storage, foundation for new paradigm for information processing to low-power nonvolatile green electronics. In spintronics, the spin-MOSFET is considered to be the building block of low-power-consumption electronics devices. And Si with its advantages is the promising channel material for Spin-MOSFET. This chapter also figures out the current issues of Si spintronics in the diffusive regime, and the motivation to solve them by ballistic transport.

In Chapter 2, overviews of the spin transport mechanisms in diffusive regime and ballistic regime were presented. Additionally, electrical spin measurements techniques were

discussed. An understanding of the physical mechanisms that govern spin transport inside semiconductors is essential for proper design and characterization of these devices, as well as for overcoming the current issues.

In Chapter 3, the fabrication process and device characterization in this study were described. At the beginning, I gave an introduction about the techniques mainly used in this research, such as EB evaporation, MBE, EBL, ion milling, and photolithography. Then, I discussed about the process flow which is used for device fabrication, from the substrate preparation, FM electrodes and tunnel barriers deposition, fabrication of nanoscale Si channel, fabrication of microscale contacts, to the last step of wire bonding to chip carriers. In the end of this chapter, the setups and techniques used to measure my devices are briefly discussed.

In Chapter 4, investigation of spin-valve devices fabricated by electron beam evaporation was presented. I have investigated the spin transport in nanoscale Si spin-valve devices with the FM and tunnel barrier prepared by the EB evaporation method. Systematic investigations of the bias voltage dependence, temperature dependence, and magnetic-field direction dependence of the magnetoresistance indicate that the observed spin valve effect is governed by the spin transport through the nanoscale Si channel. A high magnetoresistance of 12 Ω corresponding to MR ratio of 0.8 % and a large spin-dependent output voltage of 13 mV were achieved for a device with the MgO/Ge tunnel layer at a bias voltage of 1.7 V at 50 K, which are among the highest values reported at that time. The spin-valve effect decreases with

increasing temperature but remains observable up to 200 K. The results in this chapter have been published on APL **109**, 232402 (2016).

In Chapter 5, investigation of spin transport in spin-valve devices fabricated by molecular beam epitaxy was presented. An enormous spin-valve effect with $|\Delta R|$ up to 57 kΩ, corresponding to $|\Delta R/R| = 3\%$, has been clearly observed. The sign of the spin-valve effect is reversed at low temperatures, suggesting the possibility of the spin-blockade effect of defect states in the MgO tunnel barrier. A high spin-dependent output voltage is 20 mV at the bias voltage of 0.9 V at 15 K, which is among the highest values reported in lateral Si-based spin-valve devices at that time. The results in this chapter have been published in JAP **122**, 223904 (2017), which is selected as the AIP Science Highlight paper and JAP Featured paper.

In Chapter 6, I demonstrated two important roles of (quasi) ballistic transport in the nanoscale Si channel: (i) generation of spin-valve effect even when there is no barrier at room temperature, and (ii) suppress spin-flip scattering to achieve a higher spin-valve ratio at low temperature. Indeed, I have obtained a large spin-valve ratio of 3%, which is much larger than that observed in μm-long Si channel devices reported before. Nevertheless, the electron transport in my nanoscale devices may be quasi ballistic rather than fully ballistic, because the channel length (20 nm) is not much shorter than that of the mean free path of 20 ~ 40 nm for n-type Si with $n = 10^{18}$ cm^{-3} [1]. By further downsizing the Si channel length to sub-10 nm, it is possible to achieve fully ballistic transport and higher spin-valve signals. The results in this chapter have been published in AAPPS Bulletin 28, 7-15 (2018) – Featured paper.

Chapter 9

In Chapter 7, optimization of the MgO tunnel barrier thickness of spin-valve devices was described. I have investigated the spin transport in nanoscale Si spin-valve devices prepared by MBE with different MgO layer thickness. In the device with MgO (1.5 nm) / Ge (1 nm) double layers grown by MBE, I obtained the highest spin-dependent output voltage of 25 mV. The results in this chapter have been submitted and under review.

In Chapter 8, I presented improvement of the spin-valve ratio by using an Mg buffer layer between Fe and MgO layers. In this chapter, an ultrathin Mg layer inserted between the tunnel barrier MgO and the Fe electrodes was utilized to prevent the formation of a magnetically-dead layer at this interface, in order to enhance the spin injection in this Si-based spin-valve structure. By optimizing the Mg buffer layer thickness (1 nm Mg) and MgO tunnel barrier thickness (3.5 nm MgO), I have succeeded in improving the MR ratio up to -3.6 % in this Si-based spin-valve structure. This value is the highest reported so far in lateral spin-valve devices. These results give better understanding and control of the spin transport through the tunnel barrier into Si and will be helpful for improving performance of Si-based spin-valve devices. The results in this chapter have been submitted and under review.

Chapter 9

Future Perspectives

For practical applications of Si-based spin-MOSFET, it is necessary to obtain the high spin-dependent output voltages (~ 100 mV) and high MR ratio (~ 20 %) in devices using spin-valve effect. However, previous works on spin-valve devices with μm-long Si channels showed poor spin output voltage (ΔV ~ 1 mV) and low MR ratio (~ 0.1 %). In this study, I have demonstrated the advantages of ballistic transport by using the nanoscale Si-based spin valve device. In the ballistic regime, significant improvements of the MR ratio (MR = 3.6 %) and the spin output voltage change (ΔV = 25 mV) have been shown.

However, the ballistic transport itself would be not enough to realize the large spin output voltage and MR ratio for practical applications of spin-MOSFET. Another element which plays a crucial role in spin injection process is the MgO spin filter layer. In this study, I found that the quality of MgO layer is not as good as expected. It is known that the task of growing a good quality but thin MgO layer directly on Si is challenging. Therefore, I used Ge as a buffer layer for growing MgO on Si. Indeed, the MgO/Ge double layer tunnel barrier has shown good results in improvement of the ΔV and MR ratio, comparing to a MgO single layer, as shown in Chapter 4. However, this MgO/Ge double layer has been not perfected yet. I found that the device resistance strongly depends on the temperature (~ 10^1 Ω at room temperature, but ~ 10^7 Ω at 15K), indicates that electron transport through the tunnel barrier is governed not by the direct tunneling, but by thermally activated hopping via defect states in barrier. This thermally hopping tunneling causes the inverse spin-valve effect reported in this study, which could reduce the coherent tunneling of electron through the tunnel barrier,

thus decrease the spin injection and transport in the spin-valve device. Another evidence for the high defect-state density is the decrease of device resistance with increasing the MgO thickness which has been explained in Chapter 7. All of those evidences manifest the unsatisfactory quality of the MgO layers with high defect density. Therefore, in the future, improvement of the crystal quality of the MgO spin filter barrier is the key to improve the spin-valve signal in nanoscale Si spin-valve devices.

Here, several possible methods to improve the quality of the MgO layer are outlined. The 1st method could be growth of MgO at higher growing temperature. In this study, the MgO layer has been only grown at low temperature (below 100°C). By optimizing the growing temperature (e.g. growing MgO at higher temperature), we could improve the quality of this MgO layer. The 2nd method could be using another buffer layer instead of Ge. In this study, while Ge shows its role in improving the spin injection efficiency, it is still not enough for growing a good MgO barrier with low defect density. Other materials, such as SiO_2, Al_2O_3 or HfO_2, as the buffer layer or spin filter layer, may help improve the ΔV and MR ratio. The 3rd method could be the complement of oxygen in the MgO growing process. Because MgO layer is grown at very low rate (0.03 Å/s), there is the possibility of desorption of oxygen atom from MgO during the growth process, which can create oxygen vacancy defects in MgO. By introducing O_2 into the growth chamber during the MgO growth process, we can reduce the defect density in the MgO layer.

In this study, I used the bulk Si substrates, in which it is difficult to control the depth d of the Si channel. If the ratio of $L/d \ll 1$, here L is the Si channel length, it is difficult to force

the polarized electrons move directly from injector to detector, instead of moving around in the Si substrate. Decreasing the Si channel depth by using silicon-on-insulator (SOI) substrate would be possible way to improve the signal in the Si-based nanoscale spin-valve device.

Finally, realizing the Si-based spin MOSFET will be the ultimate goal.

References

1. Qiu, B. *et al.* First-principles simulation of electron mean-free-path spectra and thermoelectric properties in silicon. *EPL (Europhysics Lett.* **109,** 57006 (2015).

Acknowledgements

At the end of 2014, a turn in life came to me to start researches on spin transport in silicon, which is a promising research topic for future electronic technology. And in the spring of 2015, by great support from Prof. Pham Nam Hai, I had opportunity to start PhD research in Tokyo Institute of Technology. 4-year is not a long time, but it is enough for me to receive wonderful things, from academic knowledge to fun in life. I also received a lot of help from people, and I would like to name some of them.

First of all, I wish to express my gratitude and appreciation to my supervisor, professor Pham Nam Hai. He is a physicist with a great understanding about the nature, especially in spintronics. In research, when unidentified problems block my path, the discussions with him clarify the problems and brighten my way. He taught me not only science, but also the attitude toward science. I have learned from him how to keep an open mind to absorb new things, but still employ the fundamental logic to evaluate the problems. I will not forget the atmosphere in parties at his home, with the great food made from his wife.

I would like to express my sincere thankfulness to professor Masaaki Tanaka for his collaboration and support in experimental facilities as well as valuable comments in my papers.

I would like to thank my Japanese friends in Pham Lab such as Yoshida, Ueda, Yao, Yamane. They helped me to do the Japanese procedures which are tough to me. From the first days I came to Pham Lab, together we have made our lab better day by day. I will not forget the “nomikai” in our lab with funny discussions, and the wonderful ski tour organized by Ueda. I learned a lot of things about seriousness and responsibility from them.

I express my sincere thanks also to Dr. Bui Cong Tinh, the JSPS fellow in Pham Lab for the valuable discussion with him. He is one of my close friend in Tokyo Tech with lot of memories.

I would like to thank Mr. Nguyen Huynh Duy Khanh, the PhD student in Pham Lab, for his help in work and for being an honest friend of mine.

I would like to appreciate all the members of Pham Lab for creating a friendly atmosphere in laboratory and supporting my research.

I also would like to appreciate members of Tanaka Lab in Tokyo University who support me in doing experiment.

I would like to express my gratitude to Rotary Yoneyama Scholarship and Iwatani Scholarship for the supports for my PhD study. Without their supports, it is tough for me to study in Japan. Especially, I wish to express the thankfulness to my Rotary sponsor, Mr. Egawa for his help. He taught me many things about Japan and life. And the food of his restaurant is so delicious. Japan gave me a chance to grow up, to complete myself, and those scholarships gave me the opportunities to be proud of being their scholarship students.

I would like to extend my sincerest thanks and appreciation to all of my friends, who gave me love and trust. You raise me up. Especially I wish to express the gratitude to my lovely girlfriend. Without her love, the weather is too cold.

Finally, I would like to say thank you to my beloved family. For all of your help and support, I cannot thank you enough. Without you, I am nothing.

List of publications

This thesis is based on the following publications:

- *Spin transport in nanoscale Si-based spin-valve devices*

  Duong Dinh Hiep, Masaaki Tanaka and Pham Nam Hai

  Applied Physics Letters **109**, 232402 (2016)

- *Inverse spin-valve effect in nanoscale Si-based spin-valve devices*

  Duong Dinh Hiep, Masaaki Tanaka and Pham Nam Hai

  Journal of Applied Physics **122**, 223904 (2017) – **Featured Paper** of **Journal of Applied Physics** and **Science Highlight Paper** of **American Institute of Physics** (AIP)

- *Spin-valve effect in nanoscale Si-based devices*

  Duong Dinh Hiep, Masaaki Tanaka and Pham Nam Hai

  Association of Asia Pacific Physical Societies Bulletin **28**, 7-15 (2018) (Featured Paper)

- *Large spin-valve effect and spin-dependent output voltage in nanoscale Silicon spin-valve devices*

  Duong Dinh Hiep, Masaaki Tanaka and Pham Nam Hai

  Submitted and under review

List of conferences

➢ International Conference

- 9th International Conference on Physics and Applications of Spin-Related Phenomena in Solids (2016) – *Spin transport in nanoscale silicon channels* – **Duong Dinh Hiep**, Masaaki Tanaka and Pham Nam Hai
- SSDM International Conference (2016) – *Spin-valve effect in nanoscale Si-based devices with ferromagnetic electrodes* – **Duong Dinh Hiep**, Masaaki Tanaka and Pham Nam Hai
- SSDM International Conference (2017) – *Inverse spin-valve effect in MBE-grown nanoscale Si spin-valve devices* – **Duong Dinh Hiep**, Masaaki Tanaka and Pham Nam Hai
- Kanamori Memorial International Symposium (2017) – *Inverse spin-valve effect in spin-valve devices with nanoscale Si channels* – **Duong Dinh Hiep**, Masaaki Tanaka and Pham Nam Hai
- IEEE International Magnetic Conference INTERMAG 2018 – *Large spin-valve effect in Si nano spin-valve devices* – **Duong Dinh Hiep**, Masaaki Tanaka and Pham Nam Hai

➢ Domestic Conference

- 第 64 回応用物理学会春季学術講演会 (2017) – *Spin valve effect in Si-based spin valve devices with a nano-scale Si channel* – **Duong Dinh Hiep**, Masaaki Tanaka and Pham Nam Hai
- 第 65 回応用物理学会春季学術講演会 (2018) – *Inverse spin valve effect in nano-scale Si-based spin-valve devices* – **Duong Dinh Hiep**, Masaaki Tanaka and Pham Nam Hai
- 第 66 回応用物理学会春季学術講演会 (2019) – *Large spin-dependent magnetoresistance and output voltage in the nanoscale Si spin-valve devices* – **Duong Dinh Hiep**, Masaaki Tanaka and Pham Nam Hai